Volume 2 · Issue 1
March 2023
ISSN: 2810-9635 (Online)

Materials Science in Additive Manufacturing

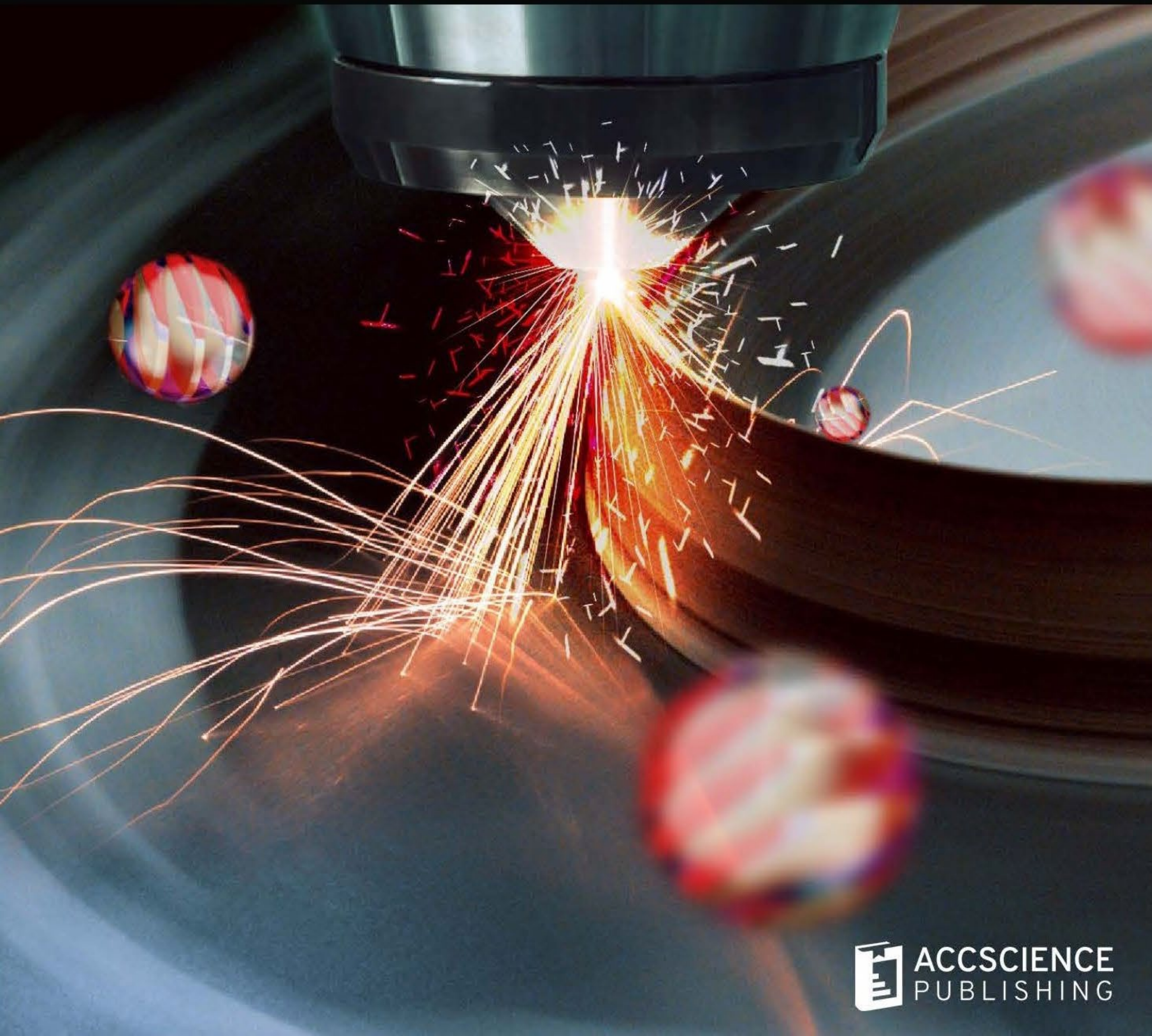

ACCSCIENCE PUBLISHING

ACCSCIENCE PUBLISHING

Materials Science in Additive Manufacturing

Online ISSN: 2810-9635

Materials Science in Additive Manufacturing aims to bridge the cutting-edge research between additive manufacturing and the entire spectrum of materials science. The journal covers all applied and fundamentals of processing, synthesis, structure, composition, properties and performance of materials designed or manipulated for additive manufacturing. The journal covers a wide scope of innovative techniques, processes, methods, and applications.

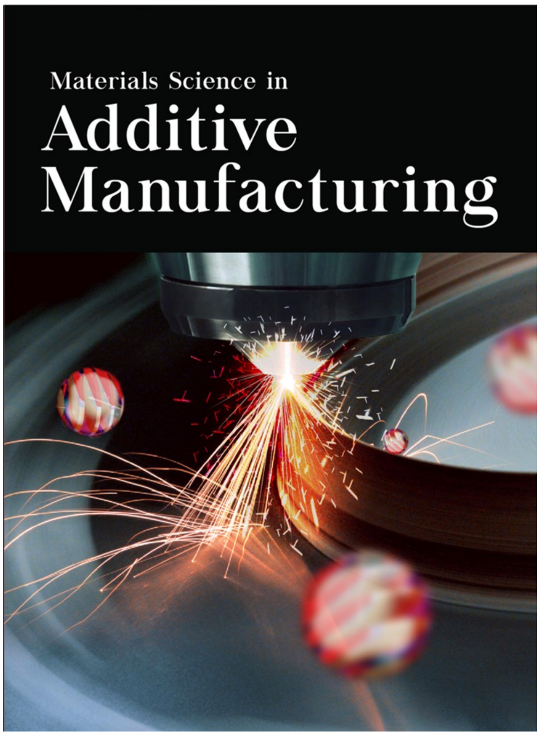

About the Publisher

AccScience Publishing is a publishing company based in Singapore. We publish a range of high-quality, open-access, peer-reviewed journals and books from a broad spectrum of disciplines.

Contact Us

Managing Editor
msam.office@accscience.sg

AccScience Publishing
8 Burn Road, #15-03 Trivex, Singapore 369977.

Volume 2 • Issue 1 • March 2023
ISSN 2810-9635 (online)

MATERIALS SCIENCE IN ADDITIVE MANUFACTURING

Editor-in-Chief

Chee Kai Chua

Singapore University of Technology and Design,
Singapore

ACCSCIENCE
PUBLISHING

Full issue copyright © 2023 AccScience Publishing
All rights reserved. Without permission in writing from the publisher, this full issue publication in its entirety may not be reproduced or transmitted for commercial purposes in any form or by any means, electronic or mechanical, including photocopying, recording, or any information storage and retrieval system. Permissions may be sought from msam.office@accscience.sg.

Article copyright © Respective Author(s)
See articles for copyright year. All articles in this full issue publication are open-access. There are no restrictions in the distribution and reproduction of individual articles, provided the original work is properly cited. However, permission to reuse copyrighted materials of an article for commercial purposes is applicable if the article is licensed under Creative Commons Attribution-NonCommercial License. Check the specific license before reusing.

MATERIALS SCIENCE IN ADDITIVE MANUFACTURING

ISSN: 2810-9635 (online)

Editorial and Production Credits

Publisher: AccScience Publishing
Editorial Assistant: Flora Kang
Production Editors: Ian Wong, Chi Tat Poon
Article Layout and Typeset: Sinjore Technologies (India)
Cover Design: BUTTON GRAPHIC DESIGN STUDIO (Malaysia)

For all advertising queries, contact msam.office@accscience.sg.

Supplementary file

Supplementary files of articles can be obtained at https://accscience.com/journal/MSAM/2/1.

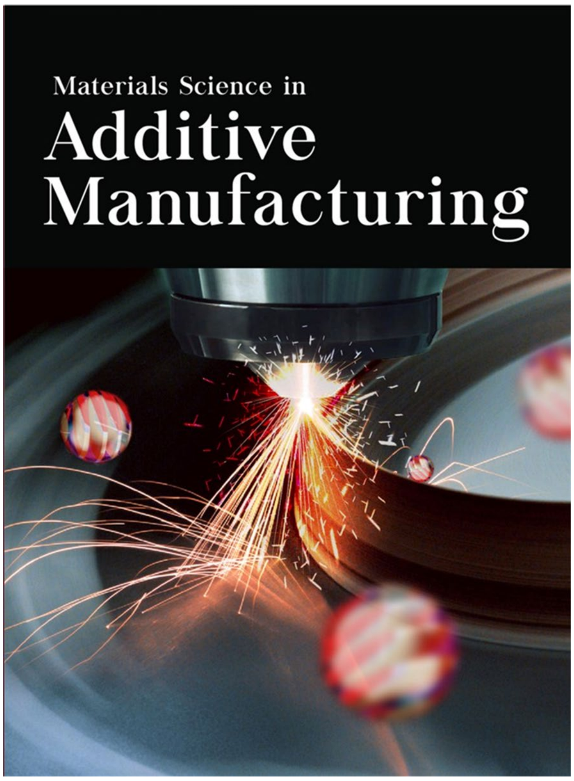

About the Cover

Directed energy deposition in progress

Disclaimer

AccScience Publishing is not liable to the statements, perspectives, and opinions contained in the publications. The appearance of advertisements in the journal shall not be construed as a warranty, endorsement, or approval of the products or services advertised and/or the safety thereof. AccScience Publishing disclaims responsibility for any injury to persons or property resulting from any ideas or products referred to in the publications or advertisements. AccScience Publishing remains neutral with regard to jurisdictional claims in published maps and institutional affiliations.

Materials Science in Additive Manufacturing

Editorial Board

Editor-in-Chief

Chee Kai Chua
Singapore University of Technology and Design, Singapore

Associate Editor

Swee Leong Sing
National University of Singapore, Singapore

Editorial Board Members*

Jingchao Jiang, *Hong Kong (China)*
Shweta Agarwala, *Denmark*
Mohsen Akbari, *Canada*
Thomas Boland, USA
Maling Gou, *China*
Paulo Jorge da Silva Bártolo, *Singapore*
Guha Manogharan, *USA*
Eujin Pei, *UK*
Cijun Shuai, *China*
Jonathan Phuong Tran, *Australia*
Chunze Yan, *China*
Ali Zamanian, *Iran*
Yicha Zhang, *France*
Clodualdo Aranas Jr, *Canada*
Mahdi Bodaghi, *UK*
Dongdong Gu, *China*
Charlotte Hauser, *Saudi Arabia*
Ming C Leu, *USA*
Tuğrul Özel, *USA*
Mui Ling Sharon Nai, *Singapore*
Jing Shi, *USA*
Dimitrios Tzetzis, *Greece*
Yiwei Weng, *China*
Jack G. Zhou, *USA*
Dong-Woo Cho, South Korea
Flávio Bartolomeu, *Portugal*
Filippo Berto, *Italy*
Shanmugam Kumar, *UK*
Pasquale Daniele Cavalière, *Italy*
Xiaopeng Li, *Australia*
Jose M. San Juan, *Spain*
Craig Banks, *UK*
Lifeng Kang, *Australia*
Ming-Wei Chang, *UK*
Leong Kah Fai, *Singapore*
Luciano Feo, *Italy*
Jikai Liu, *China*
Xiaochun Li, *USA*
Jie Zhou, *Netherlands*
Dong-Wook Han, South *Korea*
Mika Salmi, *Finland*
Wai Yee Yeong, *Singapore*
David K. Mills, *USA*
Zhangwei Chen, *China*
Antonio Gloria, *Italy*
Guoxing Lu, *Australia*

ACCSCIENCE
PUBLISHING

Volume 2 | Issue 1 | March 2023 |
Materials Science in Additive Manufacturing

https://accscience.com/journal/MSAM

CONTENTS

ACCSCIENCE PUBLISHING

Materials Science in Additive Manufacturing

ORIGINAL RESEARCH ARTICLE

Microstructure, mechanical properties, and corrosion performance of additively manufactured CoCrFeMnNi high-entropy alloy before and after heat treatment

Roman Savinov, Jing Shi*

Department of Mechanical and Materials Engineering, College of Engineering and Applied Science, University of Cincinnati, Cincinnati, OH 45221, USA

Abstract

Equiatomic CoCrFeMnNi, one of the well-known high-entropy alloys, possesses attractive mechanical properties for many potential applications. In this research, the effects of heat treatment on additively manufactured CoCrFeMnNi materials were studied. A pilot experiment was conducted to select two selective laser melting (SLM) conditions of different laser scanning speeds based on the density and porosity of obtained materials. Thereafter, microstructure, tensile properties, impact fracture, microhardness, and corrosion resistance were investigated for the materials obtained under the two selected SLM conditions, with and without heat treatment. It was discovered that while the texture with a strong <100> alignment was observed in both as-built and heat treated materials, the texture of heat treated materials was stronger. Also, heat treatment drastically improved the ductility of as-built CoCrFeMnNi by 23 – 59% for the selected SLM conditions, while the ultimate tensile strength showed only negligible change. The increase of ductility was believed to result from the release of residual strain and the increase of average grain size after heat treatment. Moreover, heat treatment was able to bring noticeable improvement in energy absorption for the as-built CoCrFeMnNi, reflected by 11 – 16% more energy absorption. Besides, all studied materials showed signs of ductile fracture, but more signs of brittle fracture, such as cleavage facets, were found in the as-built materials as compared with the heat-treated materials. In addition, higher laser scan speed was found to cause moderate reduction in corrosion resistance. Effect of heat treatment was also negative and mild for lower scanning speed case. However, the highest reduction in corrosion resistance was observed after heat treatment of the high laser scanning speed case.

Keywords: CoCrFeMnNi; High-entropy alloy; Additive manufacturing; Selective laser melting; Properties; Microstructure

***Corresponding author:**
Jing Shi
(jing.shi@uc.edu)

Citation: Savinov R, Shi J, 2023, Microstructure, mechanical properties, and corrosion performance of additively manufactured CoCrFeMnNi high-entropy alloy before and after heat treatment. *Mater Sci Add Manuf*, 2(1): 42.
https://doi.org/10.36922/msam.42

Received: November 9, 2022

Accepted: December 28, 2022

Published Online: February 9, 2023

Copyright: © 2023 Author(s). This is an Open Access article distributed under the terms of the Creative Commons Attribution License, permitting distribution, and reproduction in any medium, provided the original work is properly cited.

Publisher's Note: AccScience Publishing remains neutral with regard to jurisdictional claims in published maps and institutional affiliations.

1. Introduction

Until recently, the main strategy used in material engineering to produce alloys was choosing a principal element and adding several secondary elements to it. Such principal element approach considerably limits the scope of alloy development[1]. Common metallurgy knowledge suggests certain correlation between the number elements in a multicomponent system and the number of phases and intermetallic compounds formed in such system. In 2004, Yeh *et al.*[2] showed that single or double solid solutions can become stabilized when multiple elements are mixed in an appropriate ratio. This can happen because configurational entropy of mixing such elements is high enough to overcome the enthalpy of compound formation[1]. This new class of materials was named as high-entropy alloys (HEAs). HEAs can be defined with respect to composition or entropy. For composition-based definition, HEAs are usually the alloys containing at least four dominant elements with atomic percentage between 5% and 35%, in which additional minor elements are allowed if their atomic percentage is <5%. For entropy-based definition, entropy of mixing is calculated for alloys[1]: $S_{mix} = -R\sum_{i=1}^{n} x_i ln x_i$, where R is the gas constant and x_i is the molar fraction of the i-th element in the mixture, and the alloys with entropy higher than $1.5R$ are considered HEAs[4].

A major type of HEAs has been developed based on the parent alloy of CoCrFeNi, which consist of a single face-centered cubic unit cell (FCC) solid solution without segregation[5]. The addition of more elements to this HEA can reduce the diffusion, which enhances microstructure and mechanical properties such as creep resistance. For instance, CoCrFeMnNi, which also consists of a single-phase FCC, was first studied by Cantor *et al.*[6], and now it is known as "Cantor alloy." This alloy is one of the most thoroughly investigated HEAs, and it exhibits some attractive mechanical properties, such as unusual combination of high yield strength, high ultimate tensile strength, high ductility and fracture toughness at cryogenic temperatures[7]. The damage-tolerance can be attributed to the low stacking fault energies (SFEs) ranging from 18.3 to 27.3 $mJ/m^2 \cdot m^{-2}$ at room temperature[8]. The Cantor alloy was also shown to exhibit good radiation resistance. Damage-tolerance also rises from high lattice friction stress which results from the apparently random distribution of the solutes. This forms a true solid solution down to atomic scale which leads to high resistance to dislocation motion.

Unfortunately, the applications of HEAs are often plagued by the availability of manufacturing methods. Traditional manufacturing approaches are either expensive or inefficient in dealing with complex shapes, while additive manufacturing (AM) technology is well positioned to overcome such challenge thanks to its nature of layer-wise fabrication and significantly simplified process steps[8-10]. Compared with other AM techniques, selective laser melting (SLM), featured with high geometrical accuracy and product surface finish, has become a major AM technique for making complex metal components. Note that SLM belongs to the general powder bed fusion (PBF) group of AM processes according to the ISO/ASTM classification. In SLM, localized laser heating and high laser scanning speed result in extreme short duration of laser-material interaction[11]. The resultant rapid cyclic heating and cooling process is the root cause for the unique microstructure and mechanical properties of SLMed materials. SLM process may also produce favorable properties for HEAs. For instance, it was discovered that CoCrFeNi HEA obtained from SLM possess much higher yield strength compared with that produced by arc melting[12]. Li *et al.*[13] investigated SLM-produced CoCrFeMnNi and observed that elongated columnar grains grew epitaxially with a <001> orientation parallel to the build direction. The elemental distribution was homogeneous except Mn, which was present in higher concentration in the boundary of melting pool. Chen *et al.*[14] studied the feasibility of in situ alloying of elemental Mn with pre-alloyed CoCrFeNi in SLM. Only a single FCC phase was found in the resultant materials. The microstructure was characterized to be coarse columnar growing through more than 10 layers in the build direction, and a strong <001> texture was detected. Guo *et al.*[15] investigated machinability of SLM-produced CoCrFeMnNi. It was found that some machining operations led to compressive stress in machined surface in the cases of milling and grinding, or an increase in tensile stress in the case of wire electrical discharge machining (EDM). Savinov *et al.*[16] evaluated CoCrFeMnNi HEAs obtained from two major metal AM methods, that is, SLM and laser directed energy deposition (DED) processes. It was shown that both AM methods led to a single-phase FCC material, but the average grain size of DED-produced materials was twice that of SLMed materials.

Tensile properties of CoCrFeMnNi alloy were investigated by Li *et al.*[13], which showed the increase of ultimate tensile strength with the increase of volumetric energy density until 123 J/mm^3, followed by a flattened pattern beyond that. Zhang *et al.*[17] observed little effect of layer rotation strategy on yield and ultimate tensile strength, which were about 550 and 650 MPa, respectively. Chew *et al.*[18] studied CoCrFeMnNi manufactured by laser DED. Its tensile strength was found to be higher than the counterpart fabricated by SLM (660 MPa). Besides tensile properties, fracture toughness is also an important material property, which measures how good a given material hinders crack propagation at high-rate loading and is related to the service life and safety of many load-bearing components[19]. Together with high ductility, toughness is especially important when the SLM-produced HEAs are used as structural materials[20]. Low toughness materials generally fail in a brittle manner, which occurs rapidly almost with no plastic deformation[21], which should be avoided to prevent catastrophic failures. Kim *et al.*[22] used vacuum induction method (VIM) to fabricate CoCrFeMnNi HEA and showed that its absorbed energy was significantly higher than that of many other alloys. A similar study was performed by Xia *et al.*[23] who used vacuum levitation melting to produce CoCrFeNi HEA with varying amount of Al addition. It was observed that addition of Al lowered the impact energies at room temperature, and at Al concentrations close to that of Mn in CoCrFeMnNi, toughness dropped from 287.44 J to 1.28 J compared to pure CoCrFeNi. Bi *et al.*[24] investigated impact toughness of CoCrFeMnNi produced by laser DED. The impact toughness at 0°C was found to be four time smaller compared to the same alloy made by VIM. Kim *et al.*[25] obtained excellent impact toughness performance at cryogenic temperatures for CoCrFeMnNi produced by SLM, and they attributed the high performance to the formation of many deformation twins.

In general, the as-built alloy components from SLM processes need to receive some form of heat treatment for stress relieving and other purposes. Little information is available regarding heat treatment of additively manufactured CoCrFeMnNi HEA in the literature, and thus, the limited existing research on heat treating CoCrFeMnNi fabricated from other manufacturing processes is summarized in the following. Vaidiya *et al.*[26] showed that single FCC phases in arc melted CoCrFeNi and CoCrFEMnNi could be retained after thermal exposure at least up to 1373 K for an extended period of time, and the thermal exposure caused no disturbance to elemental distribution. In another study of the same group[27], a Cr_7C_3 contamination was found whose phase fraction did not change significantly with temperature, suggesting little dissolution of this phase during the thermal exposure up to 1373 K. Laplanche *et al.*[28] studied inductively melted and casted CoCrFeMnNi that was annealed at 870 – 1270 K for 1 h. Slight increase in hardness was found in materials annealed at lower temperature, which dropped rapidly due to the onset of recrystallization and grain growth. Sathiaraj *et al.*[29] investigated how heating rate affects microstructure evolution of heavily cold-rolled CoCrFeMnNi HEA. The studied temperature range was between 700°C and 1000°C using high (10°C/s) and low (~0.13°C/s) heating rates. It was found that heating rate significantly affected grain size and grain distribution; low rates led to larger grains with wider size distribution, which is a consequence of early activation of potential nucleation sites.

How a given HEA reacts in a corrosion environment depends on its microstructure, alloying elements, and processing methods. In recent years, corrosion resistance of CoCrFeMnNi HEA was investigated for samples produced by conventional methods[30-33], DED[34] and SLM[35-38]. Xu *et al.*[38] compared the corrosion properties of SLMed and as-cast CoCrFeMnNi and found that the former exhibit better corrosion resistance due to homogeneity of components and grain refinements. It was found that the corrosion resistance of HEA thin film in sea water benefits form heat treatment[33]. However, studies on bulk SLMed HEAs of Al_xCoCrFeMnNi showed that corrosion resistance declines after heat treatment[35]. Xiang *et al.*[39] showed that corrosion resistance of SLMed Ti-6Al-4V is dependent upon the laser power and laser scanning speed. However, the trend in relationship between a process parameter and corrosion resistance was not linear, for example, it increased with scan speed up to certain value after which higher scan speeds caused lower corrosion performance while the linear increase of laser power led to oscillating behavior of the resistance.

The critical literature analysis indicates that although CoCrFeMnNi is one of the most studied HEAs, the majority of published works focus on such materials obtained by the conventional processes, such as casting and thin film deposition. For the existing works on CoCrFeMnNi obtained by AM processes, most investigated the as-built materials, but the effects of heat treatment on properties, such as impact fracture and corrosion resistance, remain uncharted. In reality, heat treatment is critical for metal AM in that it provides the stress relief and homogenization for metal alloys after the highly non-equilibrium melting and solidification in the laser AM processes. To bridge the gap, the current work investigates CoCrFeMnNi obtained from the dominant metal AM process, SLM, with a focus on the comparison of microstructure and properties between the as-built and heat-treated materials. It is expected that the findings can shed light on the understanding of CoCrFeMnNi HEA obtained from the complete SLM process, followed by heat treatment.

2. Materials and methods

2.1. SLM experiments

Spherically shaped pre-alloyed particles of equiatomic CoCrFeMnNi, made by gas atomization, were acquired for this study. The particle size distribution ranged from 15 to 53 μm, with an average diameter of 30 μm. A Concept Laser Mlab machine was adopted for SLM fabrication of HEA samples. In the SLM operation, argon was filled in the build chamber to avoid oxidation, and the substrate material is a stainless steel plate. There are two stages of SLM experiments. In the first stage, the appropriate SLM process condition for CoCrFeMnNi on the particular

SLM system was to be obtained. For this purpose, laser power (P), hatch spacing (H), and layer thickness (T) were fixed at 100W, 60 µm, and 20 µm, respectively, while the laser scanning speed (V) was varied from 200 to 800 mm/s. While this study intends to obtain various energy density input by adjusting the scanning speed alone, it is well recognized that other parameters may have significant effect on the obtained properties[40,41]. Note that the coding of sample conditions combines the numerical value of SLM laser scanning speed and the status of heat treatment. For instance, 450 AB indicates the condition of 450 mm/s. The resultant volume energy density, defined as P/(V•H•T), ranged 104.2 – 416.7 J/mm^3. As a result, seven small cubes of 5 × 5.6 × 5 mm were obtained, as shown in Figure 1. Based on the porosity observation and relative density measurement, the appropriate laser scanning speeds were determined for the next stage. In the second stage, with the same settings on laser power, hatch spacing, and layer thickness, two laser scanning speeds were selected for building larger specimens for mechanical property evaluation. Tensile test pieces were produced as a scale-down version of the subsize rectangular tensile test specimen according to ASTM E8/E8M. Their length is 56.4 mm. The length of the specimens was oriented along scan direction (SD), width along the deposit direction (DD), and thickness along transverse direction (TD), as shown in Figure 2. Charpy specimens were prepared in accordance with the ASTM E23 standard, as shown in Figure 3. Each block for Charpy test is 55 mm in length, 10 mm in width, and 10 mm in height.

To investigate the effects of heat treatment (annealing) on the microstructures and mechanical properties, half of the fabricated Charpy samples and half of the tensile samples were heat treated in a vacuum tube furnace (Model: KJ-T1700-60IC). This heat treatment strategy, adopted from other studies[26,29], consisted of ramping at the rate of 10°C/min up to 1000°C/min, dwell time of 2 h, and then quenching in water.

Electrochemical corrosion experiments were conducted in 3 M NaCl solution at room temperature. Corrosion samples were ground to 1200 grit sandpaper and then polished with 1 µm diamond slurry. Electrochemical studies were performed with a potentiostat (WaveDriver 100) equipped with a 3-electrode system, which consists of HEA sample working electrode, a Ti wire as a counter electrode, and Ag/AgCl reference electrode. Area of 10 × 10 mm was exposed to the electrolyte. To ensure a steady-state potential, an open circuit potential (OCP) was measured for 1 h. Potentiodynamic polarization curves were performed at a scan rate of 5 mV/s. Five measurements were performed for each condition to ensure the accuracy of the results, which was evaluated by calculating the standard error of these measurements.

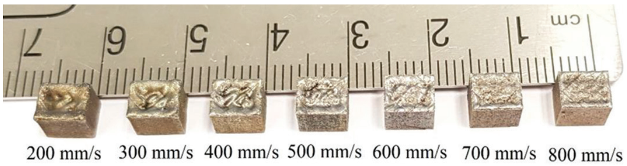

Figure 1. Selective laser melting-produced CoCrFeMnNi test cubes for scanning speed selection.

2.2. Material characterization

Cubic specimens obtained in the first stage of SLM experiment were analyzed by measuring their density and by visually analyzing their polished side whose normal is perpendicular to DD. Density of these cubes were measured with Archimedes method according to ASTM B962[42] and compared to the bulk density of 8.05 g/cm^3 for CoCrFeMnNi[36]. Furthermore, the optical micrographs of polished cubic specimens were processed by the software ImageJ, and thus the porosity of obtained materials was obtained. For the specimens obtained in the second stage of SLM experiments, they were cutoff the build plate after SLM using wire EDM. For the Charpy test, V-notch was cut by wire EDM on the surface parallel to DD for the Charpy block specimens. The impact tests were performed using a JBS-300B Charpy Impact Testing Machine. Since the absorbed impact energy of CoCrFeMnNi does not significantly change within a broad temperature range[22], Charpy test in the current study was performed only at room temperature. Besides the measurement of absorbed impact energy, the lateral expansion on the compression side of the specimens was also evaluated[43]. For the tensile specimens, tensile tests were performed on a Shimadzu Autograph AGS-X 50 kN machine at a crosshead speed of 1 mm/min at room temperature. Furthermore, Vickers microhardness was obtained on the cross-section (as defined in Figure 2A) of as-built (AB) and heat-treated (HT) samples. The applied load was 0.1 kg with dwell time of 15 s. Nine indentations were made in the matrix array with indentations being 0.5 mm apart from each other.

Metallographic samples were cut, ground, polished and then etched with a solution consisting of C_2H_5OH (25 mL) + HCl (25 mL) + $CuSO_{4.5}H_2O$ (5 g). A scanning electron microscope (model: FEI SCIOS) with electron backscatter diffraction (EBSD) capability was adopted for microstructure and texture analysis. For obtaining reliable results, three EDS area scans at different heights along DD were obtained and the averages were taken. Meanwhile, for phase identification, X-ray diffraction (XRD) profiles were obtained for the materials obtained in the second stage of SLM experiment, using a X'Pert Pro X-ray diffractometer

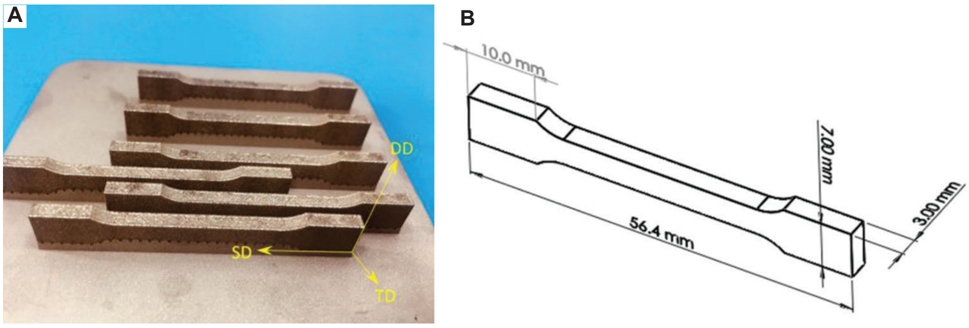

Figure 2. Selective laser melting (SLM)-produced CoCrFeMnNi tensile samples. (A) Selected tensile samples attached to the build plate after SLM; (B) dimensions of tensile samples.

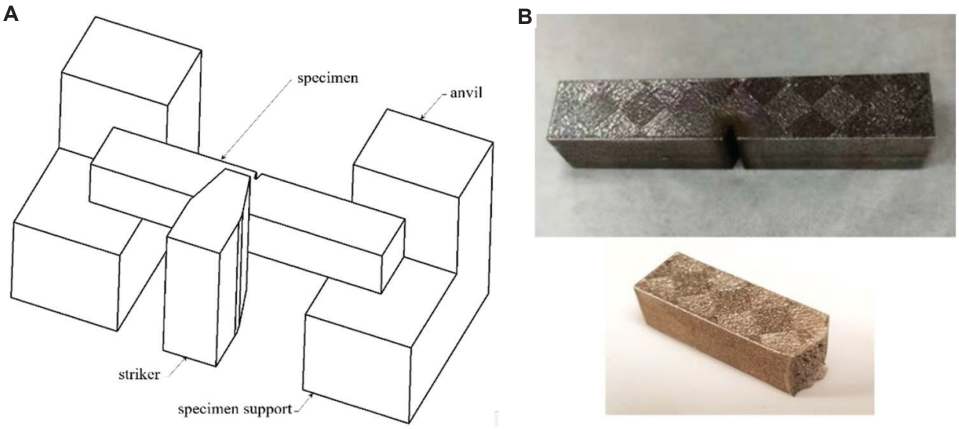

Figure 3. Charpy test of selective laser melting-produced CoCrFeMnNi. (A) Schematic orientation of Charpy specimen during the test (ASTM E23); (B) a Charpy specimen before and after test.

equipped with Cu target. The scan was performed in the 2θ range of 35° to 100° and with tube voltage and current of 40 kV and 44 mA, respectively. The fracture surfaces of Charpy V-notched samples were also characterized by surface appearance as seen in the scanning electron microscopy (SEM) images.

3. Results and discussion

3.1. Effect of scanning speed on relative density and porosity

The criterion for selecting the proper scanning speed was based on the porosity or the density of the SLM-produced materials. Figure 4A shows the optical micrographs of the cross sections of cubic samples obtained under the seven scanning speeds. It is clear that the density and size of pores increase as the scanning speed decreases. This phenomenon can be explained by the following. It is well known that incorrect choices of laser energy density in SLM often result in formation of defects. Depending on defect types, the energy density domain for SLM can be split into three regions. Low energy densities in the first region usually cause lack of fusion (LOF) defects as laser fails to provide sufficient energy to generate full melting of powder layers, which leads to the formation of pockets of unmelted powder particles or even delamination from the previously deposited layers[44]. The second region of energy density domain is the target for process parameter optimization and can be characterized by the reduced porosity fraction. In the third region, excessive overheating caused by high energy density generates surface temperatures that exceed the evaporation point of an alloy causing particles and molten material to eject from heat-affected zone, resulting in large spherical pores[45]. Strong vaporization and spatter lead to shortage of molten metal to fill the molten track. As a result, a printed part is left with many voids[46]. Moreover, high energy density may cause vaporization of low melting elements, which becomes entrapped and leads to the formation of pores. Inert gas dissolved in the molten metal and released during solidification as well as moisture present on the surface of powder particles may also be the source of gaseous porosity[45].

In the present study, energy density optimization was performed by varying the scanning speed, and the scope of chosen values revealed only the latter two regions of energy density domain as explained above. As shown in Figure 4A, laser scanning at slower than 400 mm/s resulted in severe porosity. Notice the top surfaces of the samples are not flat. This is a result of high energy density input used to produce samples in Figure 4. High energy input causes two phenomena that take place in a molten pool. First, the liquid viscosity is too low to keep up the integrity of the melt pool[47]. Melt pool agitates violently which results in a non-uniform top surface[48]. Second phenomenon is a steep thermal gradient that develops due to the high energy input and causes the higher cooling rate. As a result, the molten material does not have enough driving force and time to spread to become flattened. This leads to a big wavy surface at the top of samples[49]. Figure 4B summarizes the quantitative characterization by means of measured density of cubic samples and visual analysis of percent porosity as observed on their cross section. An overall trend can be observed, that is, higher scanning speeds (within the investigation range) are beneficial for

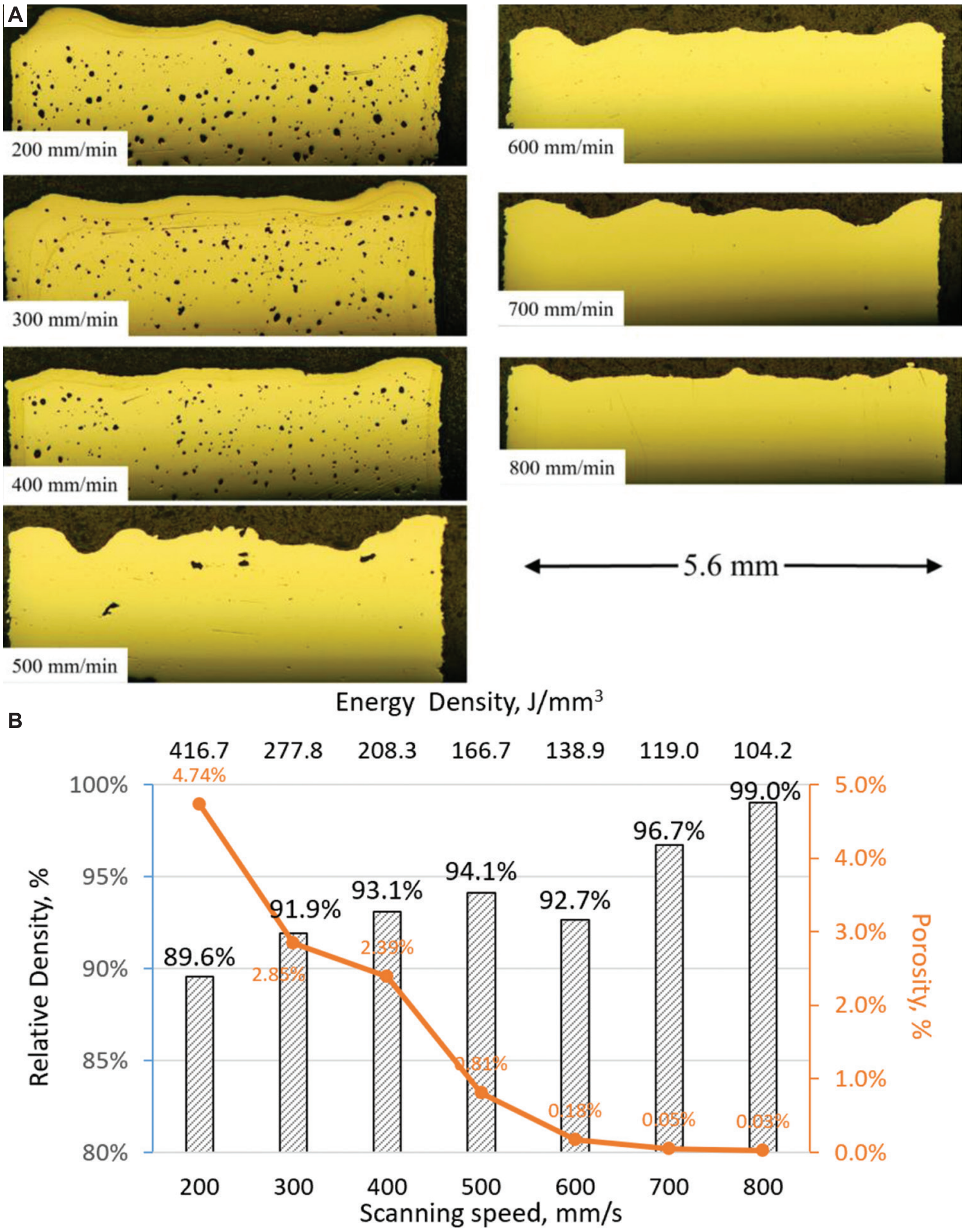

Figure 4. Effect of scanning speed on density and porosity of selective laser melting-produced CoCrFeMnNi. (A) Optical micrographs showing cross sections of printed cubes for process optimization, and (B) density of the cubes measured according to ASTM B962 and porosity measured through image processing.

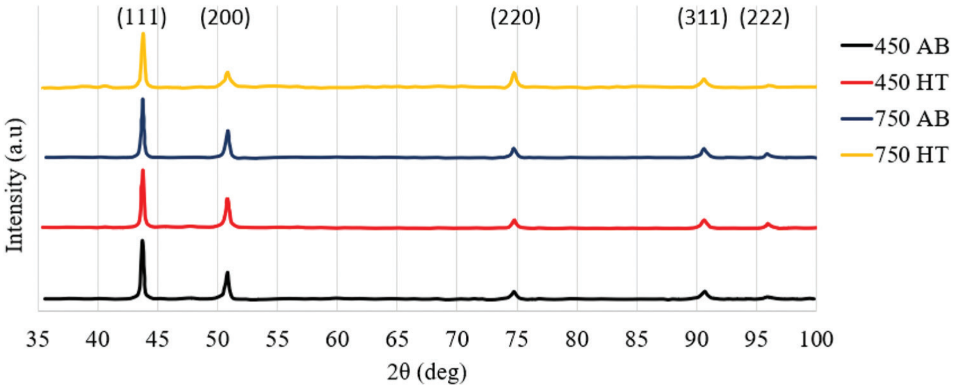

Figure 5. X-ray diffraction analysis results of selective laser melting-produced CoCrFeMnNi at 450 and 750 mm/s scanning speeds before and after heat treatment.

densification of SLM-produced CoCrFeMnNi. It is clear that a scanning speed between 700 and 800 mm/s can lead to very low porosity, and thus the scanning speed of 750 mm/s was chosen to produce samples for mechanical property evaluation. Meanwhile, a scanning speed between 400 and 500 mm/s exhibit acceptable porosity, and thus the scanning speed of 450 mm/s was chosen for comparison purpose. Additional relative density measurements show that the relative density values for 450 mm/s and 750 mm/s are 93.8% and 97.4%, respectively.

3.2. Microstructure analysis

Figure 5 shows the results of XRD analysis for the SLM-produced CoCrFeMnNi using the two scanning speeds of 450 and 750 mm/s before and after heat treatment. FCC single phase was detected in all the four conditions. The XRD results obtained in this study are typical for CoCrFeMnNi produced by laser AM processes, such as SLM[13,14] and laser DED[50,51]. No significant shift in peak locations was observed among the studied materials, indicating that the chosen range of scan speed as well as heat treatment had negligible effect on crystal structure and phase composition of the studied materials.

Figure 6 shows SEM images of the DD-TD section of CoCrFeMnNi samples before and after heat treatment. The 450 AB sample consists of layer-wise microstructure, but the melt pool marks are not regularly stacked due to the frequent change of SD. The microstructures of samples before and after heat treatment are very similar, while there is a small difference in average size of melt pools. The average melt pool length of 450 AB condition is about 140 µm, while that 750 AB condition is approximately 120 µm. The smaller size of melt pools of 750 AB sample can be explained by the lower energy density applied in the SLM process. Consequently, less material is melted at the faster scanning speed sample. Heat treatment provides the homogenization effect, and thus the melt pool boundaries are no longer clearly revealed. However, a similar pattern can be observed in terms of elongated grains. The average grain width of 450 HT sample is approximately 85 µm, while that of 750 HT sample is between 50 and 80 µm. Although SEM observations found no such particles, some powder did not fully melt in the SLM process. This is evident from the fact that unmelted particles are present on the fracture surface of Charpy samples (Figure 16E). However, they are not randomly scattered across the fracture surface but only found inside few isolated colonies and therefore should not be present in abundant amount in the obtained materials.

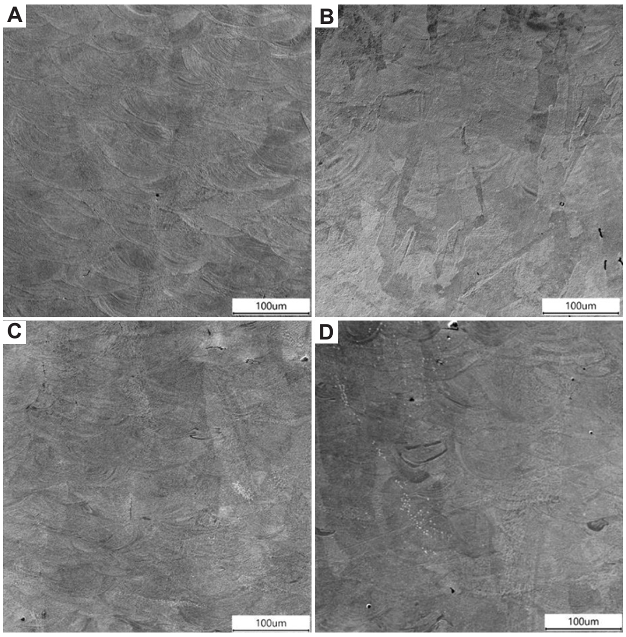

Figure 6. SEM micrographs of selective laser melting-produced CoCrFeMnNi (450 and 750 mm/s scanning speeds, before and after heat treatment) in the DD-TD cross section. (A) 450 AB; (B) 450 HT; (C) 750 AB; and (D) 750 HT.

To understand the effect of scan speed and heat treatment on crystallographic texture, EBSD analysis was performed on the DD-TD section. Figure 7 shows the inverse pole figure (PF) maps as well as PFs for the studied materials. Thanks to the XRD analysis results, only FCC phase was needed to index the pattern for obtaining inverse PFs (IPFs). The confidence index (CI) of all samples is high (0.62 – 0.65). The microstructure of all four conditions primarily consists of coarse columnar grains of 75 – 200 μm wide, and these grains cross several layers along the deposition direction. Such phenomenon is typical for the morphology for AM-produced materials[11,20,52,53], which is driven by epitaxial growth due to re-melting in the layer wise process[54]. The PFs (PFs) show presence of

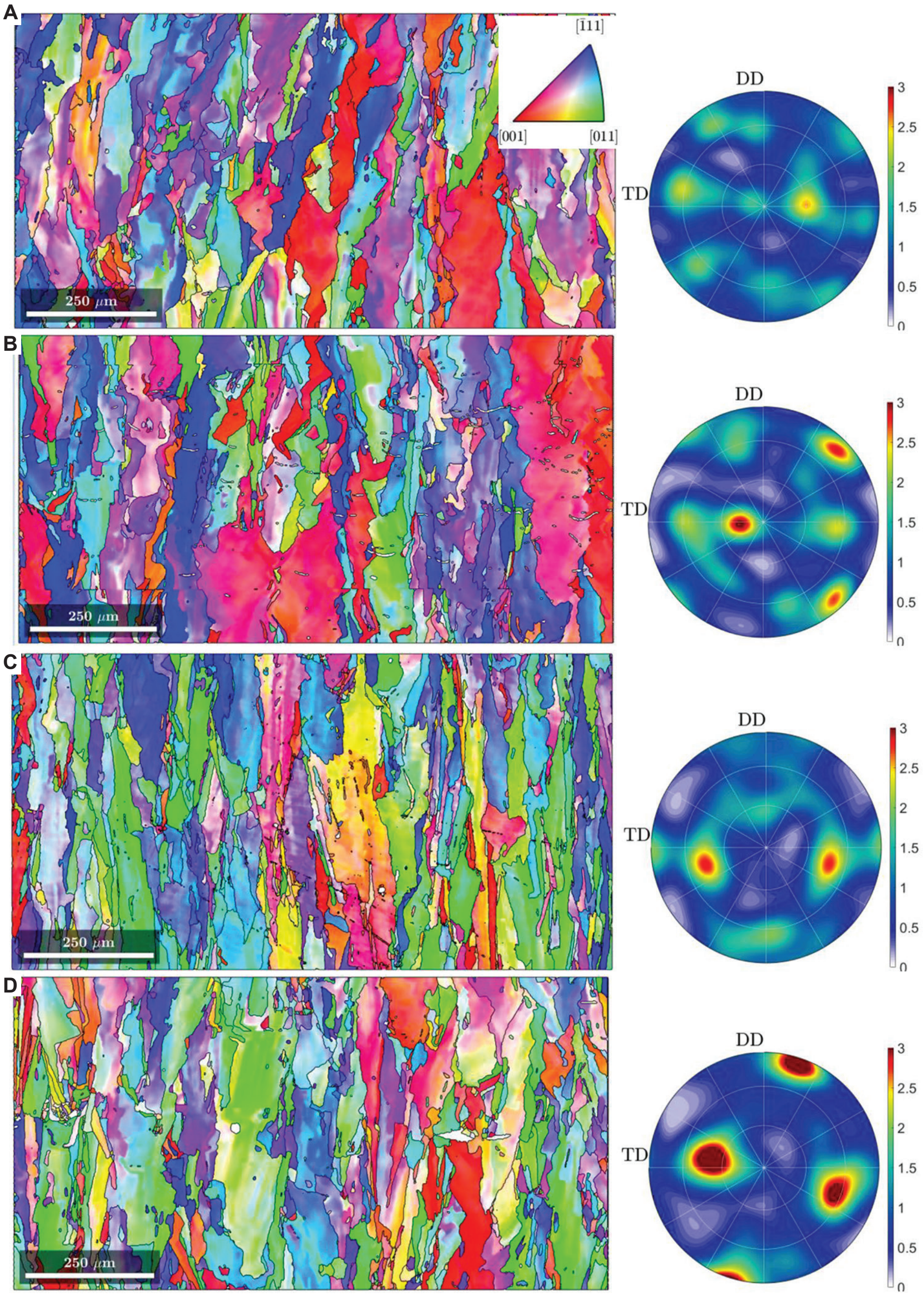

Figure 7. Inverse PFs (IPFs) along the normal direction and their corresponding PFs for SLM-produced CoCrFeMnNi using 450 and 750 mm/s scanning speeds before and after heat treatment. (A) 450 AB; (B) 450 HT; (C) 750 AB; and (D) 750 HT.

texture with a strong <100> alignment in all four samples. However, HT samples appear to have a stronger texture since the intensities of their PFs are higher compared to AB samples, which indicates that heat treatment causes more grains to align with similar orientation. Scanning speed affects the texture as well. The PF intensity of the 750 AB is noticeably higher compared to that of 450 AB. The same is true for heat-treated samples produced with different scanning speeds.

Figure 8 shows grain boundary misorientation distributions for all four conditions. The distribution of all samples is not random and with exception of 450 HT, and all samples feature a single peak with an average misorientation around 45°. Grain boundaries with 45° misorientation mainly correspond to rotation around [100] direction[55]. Meanwhile, the small angle misorientation (<15°) was reduced after heat treatment for both 450 and 750 mm/s samples. The grain size was calculated using one-dimensional parameter, which refers to the longest distance (diameter) between any two boundary points[56]. A weighted averaging approach was used to calculate the average grain size using the following equation[57]:

$$\overline{d_i} = \frac{1}{\sum_{i=0}^{n} A_i} \sum_{k=0}^{n} A_i d_i \, , \qquad \text{(I)}$$

Where n is the number of grains, A_i is the area of grain I, and d_i is the diameter. As seen from Figure 8, heat treatment led to increase in average grain size. However, such increase is more pronounced in the 450 mm/s cases for which average grain size increased from 276.5 to 309 μm after heat treatment, while in the 750 mm/s cases, grain size increase was more moderate (from 242.1 to 254.4 μm) after heat treatment. Grains of the 450 AB condition are noticeably larger as compared to that of the 750 AB condition for the reasons explained earlier, and similar relationship holds for the HT samples.

As shown in Figure 9, the compositions of both AB and HT samples are overall uniform and close to the equiatomic composition of the original powder. There is a slight misbalance in Cr and Mn with the latter being in a small depletion especially for the 450 mm/s samples. This might be because during the SLM process, the surface temperature of melt pools can exceed the boiling point of the alloy. The difference in vapor pressures on the melt pool surface creates a driving force for vapor to leave the surface[58]. Mn has the highest vapor pressure and lower melting temperature among other constituencies of the HEA and thus can easily leave the melt pool[59]. Such high volatility of Mn agrees with the current results. Samples of 450 mm/s condition receive higher energy during SLM process leading to higher melt pool temperatures, which hold for longer time. Consequently, higher amount of Mn has a chance to escape resulting in Mn depletion of 450 samples. Heat treatment obviously has no significant effect on Mn content since 1000°C chosen for treatment

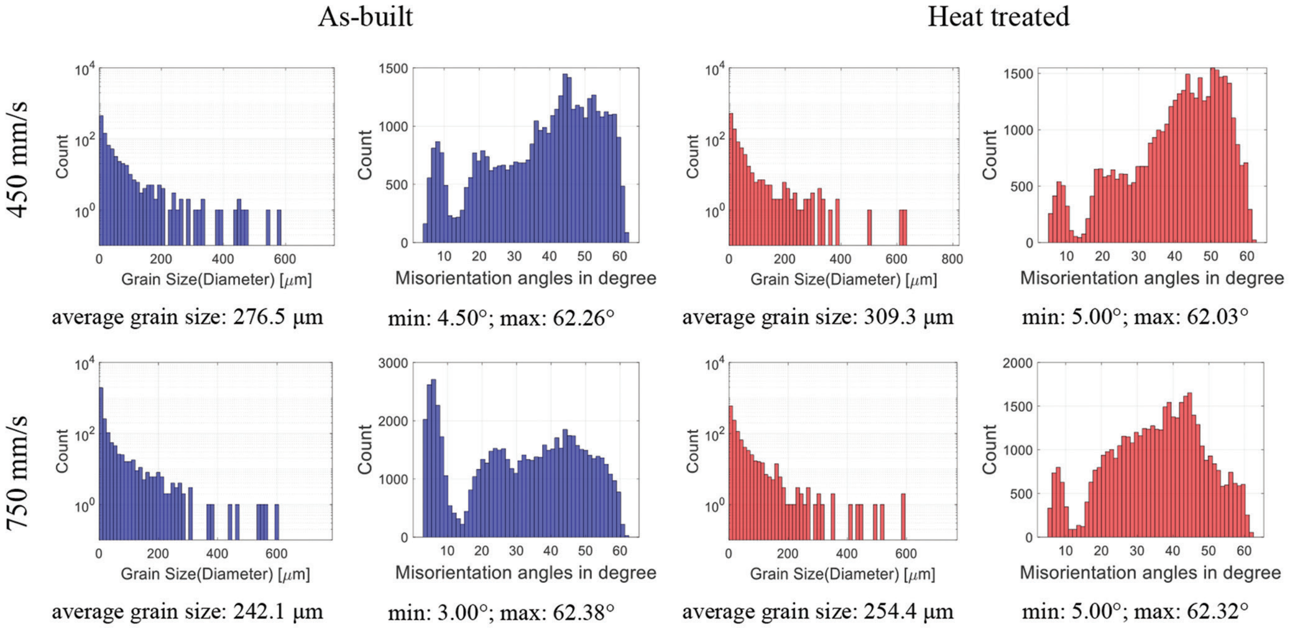

average grain size: 276.5 μm

min: 4.50°; max: 62.26°

average grain size: 309.3 μm

min: 5.00°; max: 62.03°

average grain size: 242.1 μm

min: 3.00°; max: 62.38°

average grain size: 254.4 μm

min: 5.00°; max: 62.32°

Figure 8. Grain boundaries misorientation distribution and grain area distribution for selective laser melting-produced CoCrFeMnNi using 450 and 750 mm/s scanning speeds before and after heat treatment.

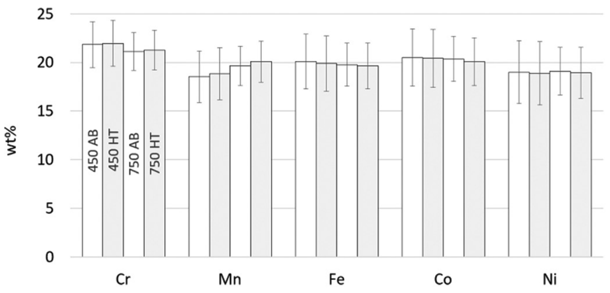

Figure 9. Average composition of selective laser melting-produced CoCrFeMnNi at 450 and 750 mm/s scanning speeds before and after heat treatment.

is far less than the melting temperature of Mn (1246°C). Mn evaporation is believed to contribute to the formation of voids in SLM-produced samples with the higher energy density as discussed above. In the literature, similar phenomenon was observed in SLM-produced CoCrFeMnNi[36]. Together with the presence of the aforementioned micro-cracks, this slight depletion in Mn might be another indication of the need for further process parameter optimization. On the other hand, the heat treatment hardly affects the composition of SLM-produced CoCrFeMnNi.

3.3. Electrochemical corrosion behavior

Open circuit potential (OCP) is a straightforward method to study the corrosion behavior. Figure 10 shows OCP results for four conditions. Potentials of both AB conditions gradually shift toward the anodic direction or in positive (more noble) potential values. This is an indication that a passive film was formed on the surface of AB samples[36,60]. The OCP of 750 AB sample has dipped toward the end of the experiment, which is an indication of a breakdown and re-passivation. The opposite phenomenon was observed with OCP of HT samples. OCPs of both 450 HT and 750 HT samples shift towards the cathodic direction or in the negative (less noble) potential values and after 1 h, and the potential stabilizes at about −0.1 V versus normal hydrogen electrode (NHE). In this case, the implication is that passive layers did not form.

Tafel potentiodynamic polarization curves of 450 and 750 samples at AB and HT conditions are shown in Figure 11. Potential at the dip of such curves represents corrosion potential (E_{corr}). This parameter reflects the stability of the system: the higher the E_{corr} and the smaller the corrosion tendency[37,39]. Figure 12 summarizes the corrosion potentials for all four cases obtained in this experiment. As can be seen from the two figures, higher scanning speed results in slight decrease in corrosion resistance in the AB case. After heat treatment, such decrease is more pronounced as E_{corr} of 750 HT case is almost 100 mV <450 HT case. Gradual decrease in corrosion resistance with increase of scan speed was also reported for SLMed Ti-6Al-4V[39], 316L steel[61] and CoRrW[62].

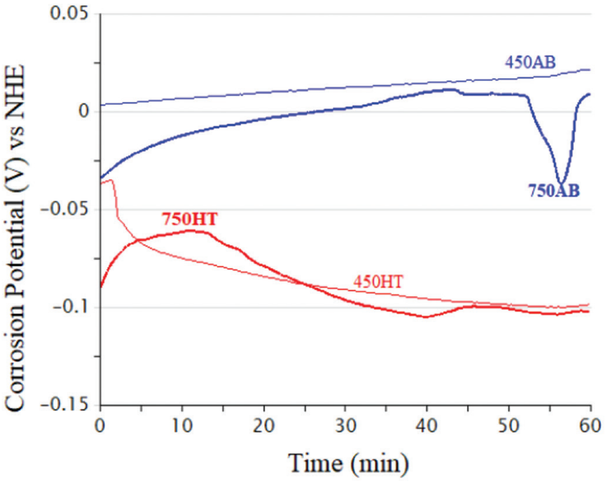

Figure 10. Open circuit potential with respect to normal hydrogen electrode for selective laser melting-produced CoCrFeMnNi at 450 and 750 mm/s scanning speeds, with and without heat treatment.

It appears that heat treatment also reduces corrosion resistance of the SLMed CoCrFeMnNi. In some cases, its effect is stronger compared to scan speed. As shown in Figure 12, corrosion potential decreased from −0.200 to −0.216 V versus NHE after heat treatment of 450 sample while it decreases from −0.225 to −0.291 V versus NHE after heat treatment of 750 sample. Corrosion resistance decline was also reported for SLMed AlCoCrMnNi HEA and was attributed to phases formed after heat treatment, which result in less protective passive film[35]. Zhu *et al.*[63] reported decrease in corrosion resistance of CoCrFeMnNi with annealing time longer than 6 h. Decrease in the anti-corrosion property was attributed to σ precipitates and Mn-rich inclusions, which increase the susceptibility to pitting corrosion.

3.4. Mechanical properties

3.4.1 Tensile properties

The engineering stress-strain curves, ultimate tensile strength, and elongation of the tensile samples are presented in Figure 13. It can be seen that heat treatment causes only insignificant changes in ultimate tensile strength (<0.5% for the 450 mm/s cases, and up to 4% for the 750 mm/s cases), while it considerably improves the ductility (59.3% and 23.2% increases for the 450 and 750 mm/s cases, respectively). Similar results were observed in spark plasma-sintered CoCrFeMnNi[3]. Decrease in tensile

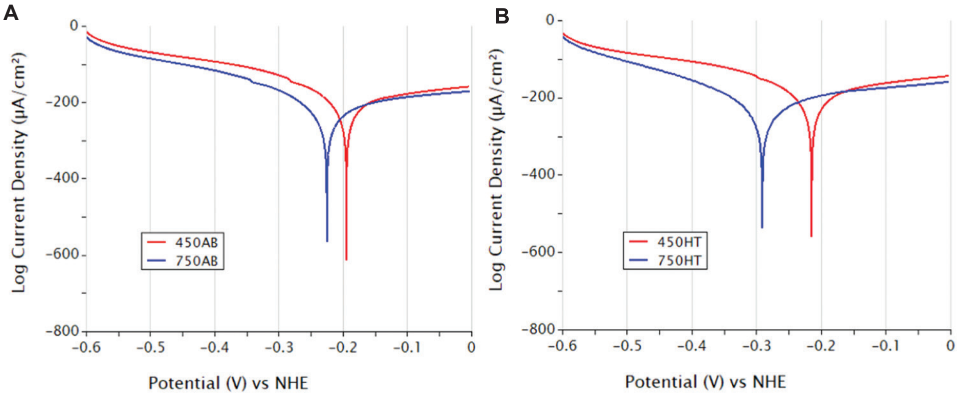

Figure 11. Tafel potentiodynamic polarization curves of selective laser melting-produced CoCrFeMnNi at 450 and 750 mm/s scanning speeds at AB conditions (A) and HT conditions (B).

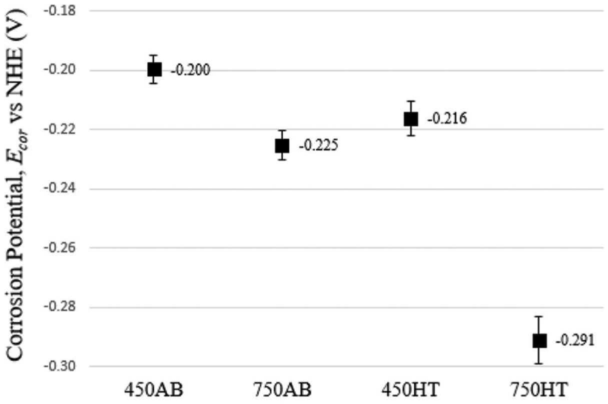

Figure 12. Summary of corrosion potentials for selective laser melting-produced CoCrFeMnNi at 450 and 750 mm/s scanning speeds before and after heat treatment.

strength after heat treatment is usually associated with either the Hall-Petch effect[13], which establishes the inverse relationship between grain size and tensile strength, or with the formation of precipitates such as carbides along the grain boundaries and plate-like martensitic phases which contribute to stress concentration[64], or with residual stress caused by lattice distortion[13]. The more obvious increase in ductility after heat treatment can be attributed to the increase of grain size and reduction of small-angle misorientation (shown in Figure 8), which is a clear indication of release of residual strain induced by SLM process, and restoration of ductility. Note that the obtained tensile properties are in general on par with the reported values from SLM and laser DED processes under the as-built condition. For instance, an ultimate tensile strength value of 601 MPa was achieved for SLM produced CoCrFeMnNi without heat treatment[65], and an ultimate tensile strength value of 660 MPa was reported for laser DED-produced CoCrFeMnNi without heat treatment[18]. However, the tensile properties are lower compared with the highest ultimate tensile strength and elongation achieved by the traditional casting process, which were reported to be 763 MPa and 57%, respectively.

3.4.2. Microhardness

Microhardness results for all four conditions, along with the reported values in literature are shown in Figure 14. It appears that the scanning speed does not affect the microhardness of as-built samples. Both 450 AB and 750 AB conditions have practically the same hardness at about 237 HV. In contrast, the microhardness after heat treatment is significantly smaller for both 450 HT and 750 HT conditions. However, the effect of heat treatment on the 750 mm/s sample in terms of microhardness was more pronounced. The hardness of the 750 AB sample decreased by 15% while that of 450 AB sample decreased by only 8.6% after heat treatment. Note that the microhardness values for as-built materials are modestly higher than the hardness of 212 HV1 reported for SLM produced CoCrFeMnNi[66], and even higher compared to the DED produced CoCrFeMnNi (195 HV5)[67] and the cast and homogenized (C&H) CoCrFeMnNi (160 HV1)[68]. In addition, the obtained microhardness values are close to that reported for the same HEA produced by arc melting and drop casting with cold rolling (AMDC&CR) of 21% reduction (222 HV0.3)[69].

3.4.3. Impact fracture

The Charpy test results are depicted in Figure 15. Similar to the microhardness results, the laser scanning speed has little effect on how much energy has been absorbed by 450 AB and 750 AB conditions. Both have almost the same value of 140 J. However, heat treatment generates noticeable influence on the impact fracture results - the energy absorption for the 450 mm/s samples increased

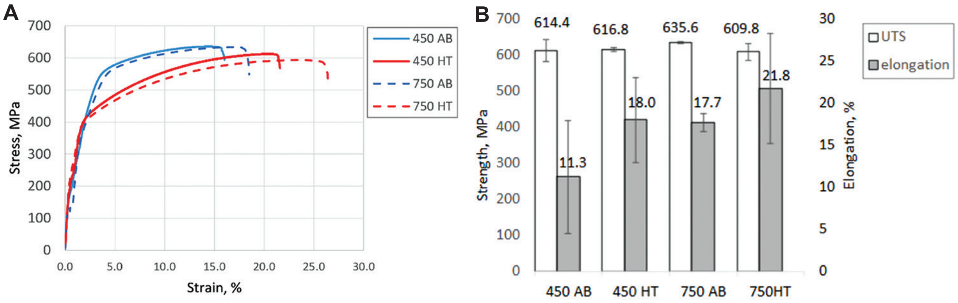

Figure 13. Tensile properties of selective laser melting produced CoCrFeMnNi at 450 and 750 mm/s scanning speeds before and after heat treatment. (A) Room temperature stress-strain curves; (B) ultimate tensile strength and elongation.

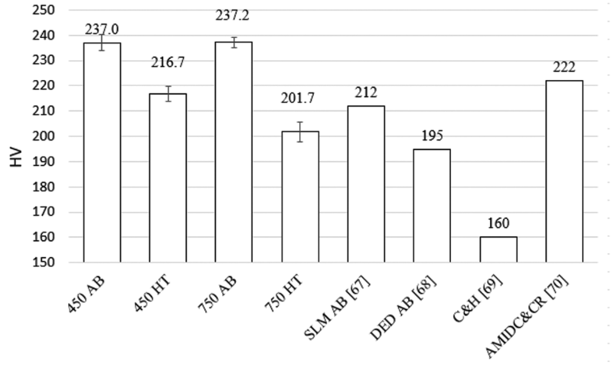

Figure 14. Microhardness results for selective laser melting-produced CoCrFeMnNi at 450 and 750 mm/s scanning speeds before and after heat treatment, along with the microhardness values reported in literature.[66-69]

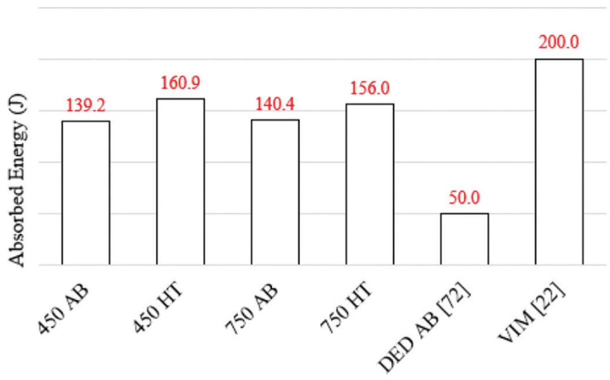

Figure 15. Energy absorption during Charpy test for selective laser melting-produced CoCrFeMnNi at 450 and 750 mm/s scanning speeds before and after heat treatment, along with the reported absorption energies in literature[22,71]. Note that the DED result[71] was obtained at 0°C.

by 15.6%, while that for the 750 mm/s samples increased by 11.1%. The absorbed impact energy of both HT and untreated samples are noticeably smaller than the energy absorbed by VIM-produced CoCrFeMnNi (approximately 200 J)[22] which, in turn, is half that of the forged Al_xCoCrFeNi[70]. On the other hand, Charpy results of the current study are significantly higher compared to CoCrFeMnNi sample made by DED whose impact energy was measured to be only 50 J at 0°C[24]. This toughness reduction of SLM-produced samples compared to the cast samples can be attributed to the presence of defects, such as pores, impurities, and brittle, non-equilibrium phases. The latter two were not observed in the present work but the existence of defects, such as LOF and micro-cracks, described above may explain such toughness reduction.

To better understand the impact behavior, fracture surface images of 450 and 750 mm/s samples, both before and after heat treatment, were studied. Higher magnification SEM images reveal features that are characteristic for both ductile and brittle fracture. For instance, Figure 16A shows that vast area of fracture surface is dominant by large dark islands with average size of 50 – 150 µm surrounded by a texture that appears brighter. The observed flat dark islands are cleavage facets whose presence indicates brittle type fracture[43,71]. Cleavage facets are surrounded by region that consists of dimples and microvoid coalescence of a submicron size. Abundance of dimple pattern is a typical characteristic of ductile fracture, which is related to the coalescence of microvoids. The microvoids can form due to decohesion between second-phase particle and matrix[43]. High magnification image in Figure 16B of dimple pattern shows that they were formed by both normal and shear ruptures. When the SEM electron probe hits inclined edge of a dimple, more of secondary electrons escape from it than from the flat surface of cleavage facets. This leads to so-called edge effect leading to brighter appearance of the region that surrounds cleavage facets[72]. Figure 16C and D shows two cleavage facets whose size differs roughly by an order of magnitude. The smaller one demonstrates clearly defined cleavage steps, river pattern and dimples surrounding the cleavage area, which are similar to the features observed on the fracture surface of AlCoCrCuFeNi HEA[71]. Besides, unmelted powder particles are observed on fracture surface of all studied samples. In most cases, they are found in a colony of conglomerated particles,

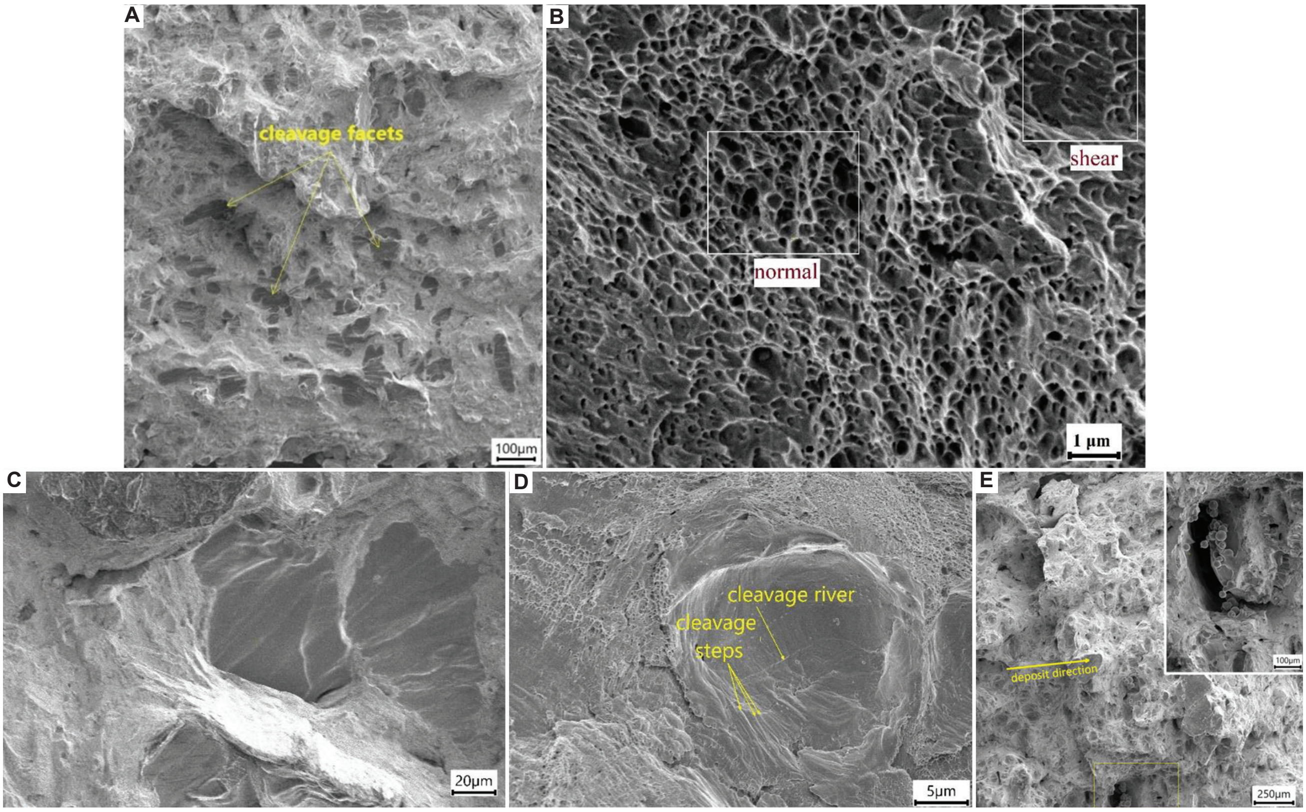

Figure 16. Fracture surface analysis of a 450 AB Charpy sample after testing. (A) Overall observation showing large amount of cleavage facets; (B) a region with dimples formed by normal and shear fractures; (C) a large cleavage facet; (D) a small cleavage facet; (E) colonies of unmelted particles inside a void.

inside either large voids or wide cracks, as shown in Figure 16E. These colonies of unmelted powder particles are surrounded by a smooth surface without cleavage steps or river pattern suggesting that the cause of fracture in the vicinity of unmelted powder particles is LOF.

Figure 17 shows low magnification image of surface of the 450 and 750 samples before and after heat treatment. There is a clear difference between the fracture surface morphology before and after heat treatment. The amount and size of cleavage facets of the HT sample are smaller compared to the AB sample while more ductile dimples can be observed on the surface of the HT sample. Both materials have lots of slightly curved deep cracks with their concave up direction pointing toward the deposit direction. Their positions are generally aligned with a straight line orthogonal to the deposition direction (marked as dashed line), which suggests that they are situated on the same deposited layer. In addition, almost all such cracks are free of unmelted powder particles. The fact that these cracks are found in HT samples as well suggests that the chosen heat treatment is not effective for the reduction of these defects, and perhaps hot isostatic pressing (HIP) treatment

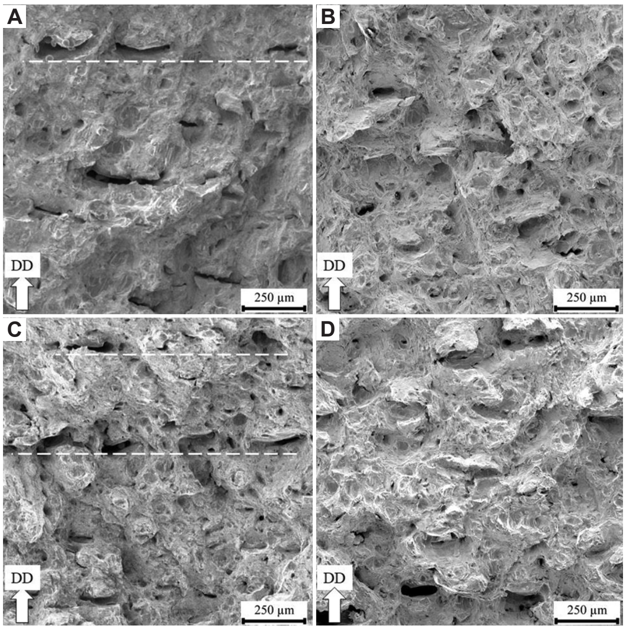

Figure 17. Fracture surface of (A) 450 AB, (B) 450 HT, (C) 750 AB, and (D) 750 HT Charpy samples showing wide cracks originated on lack of fusion defects.

can help to eliminate or reduce the amount of such defects and therefore significantly increase impact toughness of SLM-produced CoCrFeMnNi.

4. Conclusions

This research focuses on the effect of heat treatment on microstructure and properties of SLM-produced CoCrFeMnNi, in which the impact fracture and corrosion resistance were, for the first time, studied. First, SLM experiments were performed with various laser scanning speeds, and the proper ones were determined based on the evaluation on the density and porosity of obtained CoCrFeMnNi. In the next step, various samples such as Charpy impact and tensile test were prepared with the selected SLM process parameters, and heat treatment was conducted on the obtained materials. Thereafter, corrosion resistance properties, tensile properties, impact fracture, microhardness, elemental composition, and crystallographic texture were investigated for the as-built and heat treated samples. The following findings can be summarized.

- Under the fixed settings of the laser power (P), hatch spacing (H), and layer thickness (T) at 100W, 60 µm, and 20 µm, respectively, the laser scanning speed between 700 and 800 mm/s was found to generate the highest density and lowest porosity.
- SLM-produced CoCrFeMnNi materials solidified into a single-phase FCC structure. While the texture with a strong <100> alignment was observed in the materials obtained using 450 mm/s and 650 mm/s scanning speeds, for both before and after heat treatment, the texture of heat-treated materials was found to be stronger according to the PFs.
- Elemental composition of obtained samples is close to the nominal composition of equiatomic CoCrFeMnNi. However, small depletion of Mn was detected especially in 450 mm/s cases, which can be attributed to the high volatility of Mn in the SLM process.
- Ductility was drastically improved by the heat treatment (increased by 59.3% and 23.2% for 450 mm/s and 750 mm/s cases, respectively), while the ultimate tensile strength showed only negligible change. It could be attributed to the release of residual strain and the increase of average grain size as a result of heat treatment.
- Between the selected 450 mm/s and 750 mm/s scanning speeds, the difference in impact energy absorption was small. However, heat treatment caused noticeable increase in energy absorption (by 15.6% and 11.1% for 450 mm/s and 750 mm/s cases, respectively).
- Electrochemical corrosion study revealed formation of passive film on surface of both AB samples as evident from anodic drift of open circuit potential test while no such films were formed on heat-treated samples. Higher scanning speed resulted in slight decrease in corrosion resistance in the as-built materials. Heat treatment also lowered the corrosion resistance, which is more pronounced for the materials obtained at 750 mm/s.

Acknowledgments

None.

Funding

None.

Conflict of interest

The authors hereby declare that they have no known competing financial interests or personal relationships that could have appeared to influence the work reported in this paper.

Author contributions

Conceptualization: Jing Shi
Data curation: Roman Savinov
Formal analysis: Roman Savinov
Investigation: Roman Savinov
Methodology: Roman Savinov
Supervision: Jing Shi
Visualization: Roman Savinov, Jing Shi
Writing – original draft: Roman Savinov, Jing Shi
Writing – reviewing and editing: Roman Savinov, Jing Shi

Availability of data

The raw/processed data required to reproduce the findings can be made available on reasonable requests.

References

1. Moghaddam AO, Shaburova NA, Samodurova MN, *et al.*, 2021, Additive manufacturing of high entropy alloys: A practical review. *J Mater Sci Technol*, 77: 131–162.
2. Yeh JW, Chen SK, Lin SJ, *et al.*, 2004, Nanostructured high-entropy alloys with multiple principal elements: novel alloy design concepts and outcomes. *Adv Eng Mater*, 6: 299–303.
3. Eißmann N, Klöden B, Weißgärber T, *et al.*, 2017, High-entropy alloy CoCrFeMnNi produced by powder metallurgy. *Powder Metallurgy*, 60: 184–197.
4. Wang X, Guo W, Fu Y, 2021, High-entropy alloys: Emerging materials for advanced functional applications. *J Mater Chem A*, 9: 663–701.

5. Chen S, Tong Y, Liaw PK, 2018, Additive manufacturing of high-entropy alloys: A review. *Entropy*, 20: 937.

   https://doi.org/10.3390/e20120937

6. Cantor B, Chang ITH, Knight P, *et al.*, 2004, Microstructural development in equiatomic multicomponent alloys. *Mater Sci Eng A*, 375: 213–218.
7. Zaddach AJ, Niu C, Koch CC, *et al.*, 2013, Mechanical properties and stacking fault energies of NiFeCrCoMn high-entropy alloy. *JOM*, 65: 1780–1789.
8. Drissi-Daoudi R, Pandiyan V, Logé R, *et al.*, 2022, Differentiation of materials and laser powder bed fusion processing regimes from airborne acoustic emission combined with machine learning. *Virtual Phys Prototyp*, 17: 181–204.
9. Sing SL, 2022, Perspectives on additive manufacturing enabled Beta-titanium alloys for biomedical applications. *Int J Bioprint*, 8: 478.

   https://doi.org/10.18063/ijb.v8i1.478

10. Shi J, Wang Y, 2020, Development of metal matrix composites by laser-assisted additive manufacturing technologies: A review. *J Mater Sci*, 55: 9883–9917.
11. Wang Y, Shi J, Liu Y, 2019, Competitive grain growth and dendrite morphology evolution in selective laser melting of Inconel 718 superalloy. *J Cryst Growth*, 521: 15–29.
12. Brif Y, Thomas M, Todd I, 2015, The use of high-entropy alloys in additive manufacturing. *Scr Mater*, 99: 93–96.
13. Li R, Niu P, Yuan T, *et al.*, 2018, Selective laser melting of an equiatomic CoCrFeMnNi high-entropy alloy: Processability, non-equilibrium microstructure and mechanical property. *J Alloys Compounds*, 746: 125–134.
14. Chen P, Li S, Zhou Y, *et al.*, 2020, Fabricating CoCrFeMnNi high entropy alloy via selective laser melting *in-situ* alloying. *J Mater Sci Technol*, 43: 40–43.
15. Guo J, Goh M, Zhu Z, *et al.*, 2018, On the machining of selective laser melting CoCrFeMnNi high-entropy alloy. *Mater Des*, 153: 211–220.
16. Savinov R, Wang Y, Wang J, *et al.*, 2021, Comparison of microstructure and properties of CoCrFeMnNi high-entropy alloy from selective laser melting and directed energy deposition processes. *Procedia Manuf*, 53: 435–442.
17. Zhang C, Feng K, Kokawa H, *et al.*, 2020, Cracking mechanism and mechanical properties of selective laser melted CoCrFeMnNi high entropy alloy using different scanning strategies. *Mater Sci Eng A*, 789: 139672.
18. Chew Y, Bi GJ, Zhu ZG, *et al.*, 2019, Microstructure and enhanced strength of laser aided additive manufactured CoCrFeNiMn high entropy alloy. *Mater Sci Eng A*, 744: 137–144.
19. Keshavarz MK, Sikan F, Boutet CE, *et al.*, 2019, Impact properties of half stress-relieved and hot isostatic pressed Ti–6Al–4V components fabricated by laser powder bed fusion. *Mater Sci Eng A*, 760: 481–488.
20. Lee KA, Kim YK, Yu JH, *et al.*, 2017, Effect of heat treatment on microstructure and impact toughness of Ti-6Al-4V manufactured by selective laser melting process. *Arch Metallurgy Mater*, 62: 1341–1346.
21. Krishnadev M, Larouche M, Lakshmanan VI, *et al.*, 2010, Failure analysis of failed wire rope. *J Failure Anal Prev*, 10: 341–348.
22. Kim JH, Lim KR, Won JW, *et al.*, 2018, Mechanical properties and deformation twinning behavior of as-cast CoCrFeMnNi high-entropy alloy at low and high temperatures. *Mater Sci Eng A*, 712: 108–113.
23. Xia SQ, Gao MC, Zhang Y, 2018, Abnormal temperature dependence of impact toughness in AlxCoCrFeNi system high entropy alloys. *Mater Chem Phys*, 210: 213–221.
24. Bi G, Chew Y, Weng F, *et al.*, 2018, Process study and characterization of properties of FeCrNiMnCo high-entropy alloys fabricated by laser-aided additive manufacturing. In: *Advanced Laser Processing and Manufacturing II*. Vol. 10813. United States: SPIE. pp. 43–52.
25. Kim YK, Kim MC, Lee KA, 2022, 1.45 GPa ultrastrong cryogenic strength with superior impact toughness in the in-situ nano oxide reinforced CrMnFeCoNi high-entropy alloy matrix nanocomposite manufactured by laser powder bed fusion. *J Mater Sci Technol*, 97: 10–19.
26. Vaidya M, Guruvidyathri K, Murty BS, 2019, Phase formation and thermal stability of CoCrFeNi and CoCrFeMnNi equiatomic high entropy alloys. *J Alloys Compounds*, 774: 856–864.
27. Vaidya M, Anupam A, Bharadwaj JV, *et al.*, 2019, Grain growth kinetics in CoCrFeNi and CoCrFeMnNi high entropy alloys processed by spark plasma sintering. *J Alloys Compounds*, 791: 1114–1121.
28. Laplanche G, Horst O, Otto F, *et al.*, 2015, Microstructural evolution of a CoCrFeMnNi high-entropy alloy after swaging and annealing. *J Alloys Compounds*, 647: 548–557.
29. Sathiaraj GD, Tsai CW, Yeh JW, *et al.*, 2016, The effect of heating rate on microstructure and texture formation during annealing of heavily cold-rolled equiatomic CoCrFeMnNi high entropy alloy. *J Alloys Compounds*, 688: 752–761.
30. Aiso T, Nishimoto M, Muto I, *et al.*, 2021, Roles of alloying elements in the corrosion resistance of equiatomic CoCrFeMnNi high-entropy alloy and application to corrosion-resistant alloy design. *Mater Trans*, 62: 1677–1680.
31. Pathak S, Kumar N, Mishra RS, *et al.*, 2019, Aqueous corrosion behavior of cast CoCrFeMnNi alloy. *J Mater Eng Perform*, 28: 5970–5977.
32. Peng H, Lin Z, Li R, *et al.*, 2020, Corrosion behavior of an equiatomic CoCrFeMnNi high-entropy alloy-a comparison between selective laser melting and cast. *Front Mater*, 7: 244.
33. Popescu AMJ, Branzoi F, Burada M, *et al.*, 2022, Influence of

heat treatment on the corrosion behavior of electrodeposited CoCrFeMnNi high-entropy alloy thin films. *Coatings*, 12; 1108.

https://doi.org/10.3390/coatings12081108

34. Melia MA, Carroll JD, Whetten SR, *et al*., 2019, Mechanical and corrosion properties of additively manufactured CoCrFeMnNi high entropy alloy. *Addit Manuf*, 29: 100833.
35. Kong D, Wang L, Zhu G, *et al*., 2023, Heat treatment effects on the metastable microstructure, mechanical property and corrosion behavior of Al-added CoCrFeMnNi alloys fabricated by laser powder bed fusion. *J Mater Sci Technol*, 138: 171–182.
36. Ren J, Mahajan C, Liu L, *et al*., 2019, Corrosion behavior of selectively laser melted CoCrFeMnNi high entropy alloy. *Metals*, 9: 1029.
37. Wang B, Sun M, Li B, *et al*., 2020, Anisotropic response of CoCrFeMnNi high-entropy alloy fabricated by selective laser melting. *Materials*, 13: 5687.

    https://doi.org/10.3390/ma13245687

38. Xu Z, Zhang H, Du X, *et al*., 2020, Corrosion resistance enhancement of CoCrFeMnNi high-entropy alloy fabricated by additive manufacturing. *Corrosion Sci*, 177: 108954.
39. Xiang S, Yuan Y, Zhang C, *et al*., 2022, Effects of process parameters on the corrosion resistance and biocompatibility of Ti6Al4V parts fabricated by selective laser melting. *ACS Omega*, 7: 5954–5961.
40. Cacace S, Semeraro Q, 2022, Fast optimisation procedure for the selection of L-PBF parameters based on utility function. *Virtual Phys Prototyp*, 17: 125–137.
41. Gong X, Zeng D, Groeneveld-Meijer W, *et al*., 2022, Additive manufacturing: A machine learning model of process-structure-property linkages for machining behavior of Ti-6Al-4V. *Mater Sci Addit Manuf*, 1: 6.
42. Lu C, Shi J, 2022, Relative density and surface roughness prediction for Inconel 718 by selective laser melting: Central composite design and multi-objective optimization. *Int J Adv Manuf Technol*, 119: 3931–3949.
43. Davis JR, 1998, Metals Handbook. Handbook Committee. Netherlands: ASM International.
44. Maitra V, Shi J, Lu C, 2022, Robust prediction and validation of as-built density of Ti-6Al-4V parts manufactured via selective laser melting using a machine learning approach. *J Manuf Processes*, 78: 183–201.
45. Cherry JA, Davies HM, Mehmood S, *et al*., 2015, Investigation into the effect of process parameters on microstructural and physical properties of 316L stainless steel parts by selective laser melting. *Int J Adv Manuf Technol*, 76: 869–879.
46. Bai Y, Yang Y, Wang D, *et al*., 2017, Influence mechanism of parameters process and mechanical properties evolution mechanism of maraging steel 300 by selective laser melting. *Mater Sci Eng A*, 703: 116–123.
47. Ye D, Zhu K, Fuh JY, *et al*., 2019, The investigation of plume and spatter signatures on melted states in selective laser melting. *Optics Laser Technol*, 111: 395–406.
48. Dai S, Zhu H, Zeng X, 2020, Effect of line energy density and wall thickness on the top surface quality of AlSi10Mg sample fabricated via selective laser melting. In: *IOP Conf Ser Mater Sci Eng*, 774: 012088.
49. Pal S, Lojen G, Hudak R, *et al*., 2020, As-fabricated surface morphologies of Ti-6Al-4V samples fabricated by different laser processing parameters in selective laser melting. *Addit Manuf*, 33: 101147.
50. Xiang S, Luan H, Wu J, *et al*., 2019, Microstructures and mechanical properties of CrMnFeCoNi high entropy alloys fabricated using laser metal deposition technique. *J Alloys Compounds*, 773: 387–392.
51. Wang Q, Amar A, Jiang C, *et al*., 2020, CoCrFeNiMo0. 2 high entropy alloy by laser melting deposition: Prospective material for low temperature and corrosion resistant applications. *Intermetallics*, 119: 106727.
52. Bian P, Shi J, Liu Y, *et al*., 2020, Influence of laser power and scanning strategy on residual stress distribution in additively manufactured 316L steel. *Optics Laser Technol*, 132: 106477.
53. Joseph J, Stanford N, Hodgson P, *et al*., 2017, Tension/compression asymmetry in additive manufactured face centered cubic high entropy alloy. *Scripta Mater*, 129: 30–34.
54. Wang Y, Shi J, Lu S, *et al*., 2017, Selective laser melting of graphene-reinforced Inconel 718 superalloy: evaluation of microstructure and tensile performance. *J Manuf Sci Eng*, 139: 041005.
55. Ratanaphan S, Yoon Y, Rohrer GS, 2014, The five parameter grain boundary character distribution of polycrystalline silicon. *J Mater Sci*, 49: 4938–4945.
56. Bachmann F, Hielscher R, Schaeben H, 2010, Texture analysis with MTEX–free and open source software toolbox. In: *Solid State Phenomena*. Vol. 160. Switzerland: Trans Tech Publications Ltd. pp. 63–68.
57. Wright S, 2014, Time for a Change-New Perspectives in Grain Size Analysis. Available from: https://www.edaxblog.com/2014/06/23/time-for-a-change-new-perspectives-in-grain-size-analysis [Last accessed on 2023 Jan 10].
58. He X, DebRoy T, Fuerschbach PW, 2003, Alloying element vaporization during laser spot welding of stainless steel. *J Phys D Appl Phys*, 36: 3079.
59. Alcock CB, Itkin VP, Horrigan MK, 1984, Vapour pressure equations for the metallic elements: 298–2500K. *Can Metallurgical Q*, 23: 309–313.
60. Mouanga M, Berçot P, 2010, Comparison of corrosion behaviour of zinc in NaCl and in NaOH solutions; Part II: Electrochemical analyses. *Corrosion Sci*, 52: 3993–4000.
61. Collazo A, Figueroa R, Pérez C, *et al*., 2022, Effect of laser speed and hatch spacing on the corrosion behavior of 316L stainless steel produced by selective laser melting. *Materials*,

15: 1353.

62. Lu Y, Gan Y, Lin J, *et al.*, 2017, Effect of laser speeds on the mechanical property and corrosion resistance of CoCrW alloy fabricated by SLM. *Rapid Prototyp J*, 23: 28–33.

63. Zhu M, Zhao B, Yuan Y, *et al.*, 2021, Effect of annealing time on microstructure and corrosion behavior of CoCrFeMnNi high-entropy alloy in alkaline soil simulation solution. *Corrosion Commun*, 3: 45–61.

64. Sing SL, Huang S, Yeong WY, 2020, Effect of solution heat treatment on microstructure and mechanical properties of laser powder bed fusion produced cobalt-28chromium-6molybdenum. *Mater Sci Eng A*, 769: 138511.

65. Gludovatz B, Hohenwarter A, Catoor D, *et al.*, 2014, A fracture-resistant high-entropy alloy for cryogenic applications. *Science*, 345: 1153–1158.

66. Piglione A, Dovgyy B, Liu C, *et al.*, 2018, Printability and microstructure of the CoCrFeMnNi high-entropy alloy fabricated by laser powder bed fusion. *Mater Lett*, 224: 22–25.

67. Haase C, Tang F, Wilms MB, *et al.*, 2017, Combining thermodynamic modeling and 3D printing of elemental powder blends for high-throughput investigation of high-entropy alloys–Towards rapid alloy screening and design. *Mater Sci Eng A*, 688: 180–189.

68. Schuh B, Mendez-Martin F, Völker B, *et al.*, 2015, Mechanical properties, microstructure and thermal stability of a nanocrystalline CoCrFeMnNi high-entropy alloy after severe plastic deformation. *Acta Mater*, 96: 258–268.

69. Otto F, Hanold NL, George EP, 2014, Microstructural evolution after thermomechanical processing in an equiatomic, single-phase CoCrFeMnNi high-entropy alloy with special focus on twin boundaries. *Intermetallics*, 54: 39–48.

70. Li D, Zhang Y, 2016, The ultrahigh charpy impact toughness of forged AlxCoCrFeNi high entropy alloys at room and cryogenic temperatures. *Intermetallics*, 70: 24–28.

71. Zhang Y, Zuo TT, Tang Z, *et al.*, 2014, Microstructures and properties of high-entropy alloys. *Progress Mater Sci*, 61: 1–93.

72. Leng Y, 2009, *Materials characterization: Introduction to Microscopic and Spectroscopic Methods*. United States: John Wiley & Sons.

ACCSCIENCE PUBLISHING

Materials Science in Additive Manufacturing

ORIGINAL RESEARCH ARTICLE

Fast layer fiber orientation optimization method for continuous fiber-reinforced material extrusion process

Valentin Marchal, Yicha Zhang*, Nadia Labed, Rémy Lachat, and François Peyraut

Laboratoire Interdisciplinaire Carnot de Bourgogne, Unité Mixte de Recherche 6303, Centre National de la Recherche Scientifique, Université de Bourgogne Franche-Comté, Université de Technologie de Belfort-Montbéliard, F-90010 Belfort, France

Abstract

Material extrusion (MEX) is an additive manufacturing process that uses thermoplastic layer-by-layer building. The use of continuous fiber-reinforced filament enhances mechanical properties, making MEX suitable for use in aerospace, automotive, and robotics industries. This study proposes a laminate optimization method to improve the stiffness of printed parts with low computing time. The 2D stress-flow-based method optimizes fiber's orientation for each layer in the stacking direction, giving results for a 3D part optimization in a few minutes. Developed with Ansys Parametric Design Language, the computation tool was tested on printed wrenches, resulting in an 18% increase in stiffness. The proposed method is applicable to any printable shape.

Keywords: Additive manufacturing; Continuous fiber printing; Finite element method; Optimization

***Corresponding author:**
Yicha Zhang
(yicha.zhang@utbm.fr)

Citation: Marchal V, Zhang Y, Labed N, *et al.*, 2023, Fast layer fiber orientation optimization method for continuous fiber-reinforced material extrusion process. *Mater Sci Add Manuf,* 2(1): 49.
https://doi.org/10.36922/msam.49

Received: February 1, 2023

Accepted: February 15, 2023

Published Online: March 17, 2023

Copyright: © 2023 Author(s). This is an Open Access article distributed under the terms of the Creative Commons Attribution License, permitting distribution, and reproduction in any medium, provided the original work is properly cited.

Publisher's Note: AccScience Publishing remains neutral with regard to jurisdictional claims in published maps and institutional affiliations.

1. Introduction

Composite materials have seen significant growth since their creation in the 1930s, with applications ranging from experimental parts to mass production. Polymer-based composites, known for their lightweight, corrosion resistance, and high stiffness, are widely used in aerospace, military, wind turbines, and automotive industries[1]. There are two types of fiber-reinforced polymers, short fiber reinforcement or long fiber reinforcement, compatible with various fiber such as carbon, glass, and aramid. Long-fiber reinforcement is the most promising for creating light parts with metal alloy-like properties[2]. However, traditional manufacturing processes are difficult and require expensive equipment. In contrast, additive manufacturing has experienced significant growth in recent decades, with several processes available including material extrusion (MEX), powder bed fusion (PBF), sheet lamination (SHL), binder jetting, directed energy deposition, material jetting, and vat photopolymerization (VPP)[3]. Four of these processes have been adapted to fiber-reinforced polymers (PBF[4-6], VPP[7], SHL, and MEX[7-9]), but MEX is the only one widely developed with continuous fiber reinforcement[3,9-11]. The MEX process builds parts layer by layer by fusing a thermoplastic filament fed into a printing nozzle by an extruder. The nozzle, controlled by three stepper motors for precise movement in the printing volume, follows routes defined by a slicer software using a computer-aided design model of the part in.stl or.obj format. Optimal printing can be achieved by adjusting parameters, such as layer height, printing temperature, and bed temperature (if equipped). The optimal values of these printed parameters depend on the printed material, nozzle diameter, and ambient air temperature. MEX is attractive due to its ease of use, compatibility with various thermoplastics, low cost (for both printer and materials), and low energy consumption. When combined with continuous fiber-reinforced filaments, the MEX process leverages the benefits of both additive manufacturing and long fiber composites, resulting in complex freeform parts with stiffness comparable to aluminum alloys, low density, and corrosion resistance[12].

However, additive manufacturing of long fiber composites results in highly anisotropic materials. Hence, aligning the fibers with the mechanical strain is crucial to obtain the best stiffness and strength in a printed part[13-15]. Therefore, non-optimized fiber paths can lead to easy breakage. While previous works have explored fiber optimization, they have limitations. Zhou *et al.*[16] proposed a 2D model that divided the part into areas, each with a specific fiber orientation. Ding *et al.*[17] designed curved fiber routes using a 2D model. Li *et al.*[18] combined the two approaches with areas divided into concentric curved fiber routes. Safonov[19] and Nomura *et al.*[20] developed curved fiber routing in both 2D and 3D models, and Jung *et al.*[21] created a complex model that considers fiber orientation and diameter. All these methods are stress-based and consider fiber to be most effective when its direction aligns with the major principal direction. However, they are not easily applied to commercial printers like Markforged or Anisoprint, and while they can be done with the open-source slicing software Aura, they require manual coding of fiber routes in a gcode file. In addition, slicers like Eiger or Aura work layer-by-layer, a constraint of the MEX process that makes it impossible to use 3D optimization models and makes it challenging to find an easy and quick optimization model for commercial printers. To solve the problem above, the best fiber orientation is determined using a standard stress flow method based on principal stress analysis and corresponding direction. Keeping ease of use for commercial printers in mind, the concept of a stack is introduced: A set of layers with optimized orientation angles for each layer, weighted by the dominant principal stress. A cost-optimization approach using a multi-layered finite element model and the previously computed best orientation angles is also proposed. This allowed the identification of a reduced number of layers, where reinforcement is necessary, while using nylon in other layers. The methodology, implemented in Ansys Parametric Design Language, was efficient and demonstrated by a 18% increase in stiffness of wrenches manufactured on a Markforged X7 printer, without the need for time-consuming topology optimization algorithms or metamodels.

2. Principal stress-based method

Since printed composite parts are built layer-by-layer, resulting in a laminate composite, fibers are not oriented in a 3D space but in a stacking way. Intuitively, a 2D method applied to each layer of a part seems to be well adapted. However, this could result in a huge simulation cost, as MEX layers are thin (close to a tenth millimeter). For example, optimization of a ten-centimeter-high part would result in a thousand optimization processes. Furthermore, commercial machines only allow one angle per layer for oriented fibers. To solve these two issues, we will not consider a 2D layer-based method, but a 3D method based on a stack division of the part, as explained later.

2.1. 3D model based on a stack division of the part

To meet the time computation needs of designers, we introduce the concept of a stack, which is a group of several layers. By working with stacks instead of individual layers, we can decrease the mesh size and significantly reduce computation time. For example, a ratio of ten between a layer-based mesh and a stack-based mesh results in a 3D mesh that is 1000 times lighter (Figure 1). Working with stacks of ten layers provides a good balance between efficient computation and accurate results from the finite element analysis, as values greater than ten result in significant loss of precision. Hence, based on this simplification concept, an optimization method is proposed to optimize the fiber angles for each stack of layers as an optimal configuration to improve the structure's stiffness and strength.

Besides an important reduction of the simulation cost, using a stack-based 3D model also allows the user to allocate different angles on the layers of a stack while a layer-based model allows only one angle per layer. Thus, if a layer-based model is considered, each layer is reinforced with only the dominant stress orientation (Figure 2B left). However, some mechanical loads may result in a complex stress flow, with several strained directions (Figure 2A). As additively manufactured composites have low stiffness and strength when the load is not aligned with the fibers, it is important to consider all the possible strained orientations, as our model allows (Figure 2B right). With our approach, the computed percentages represented by each orientation (20%, 30%, and 50%) are distributed in ten different layers, so each area is reinforced on at least one layer.

2.2. Optimization process

This section presents our optimization process with the different substeps included in the workflow (Figure 3). It is

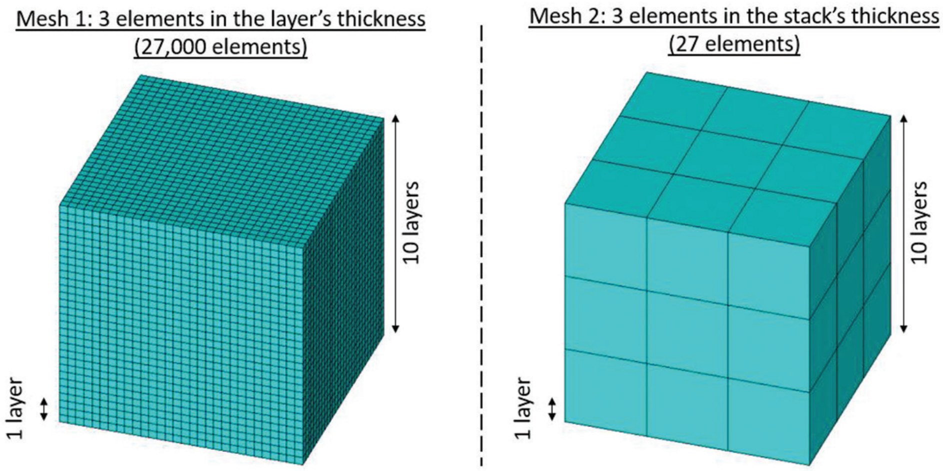

Figure 1. Comparison of number of layer-dimensioned mesh (left) and a stack-dimensioned mesh (right) on the same volume.

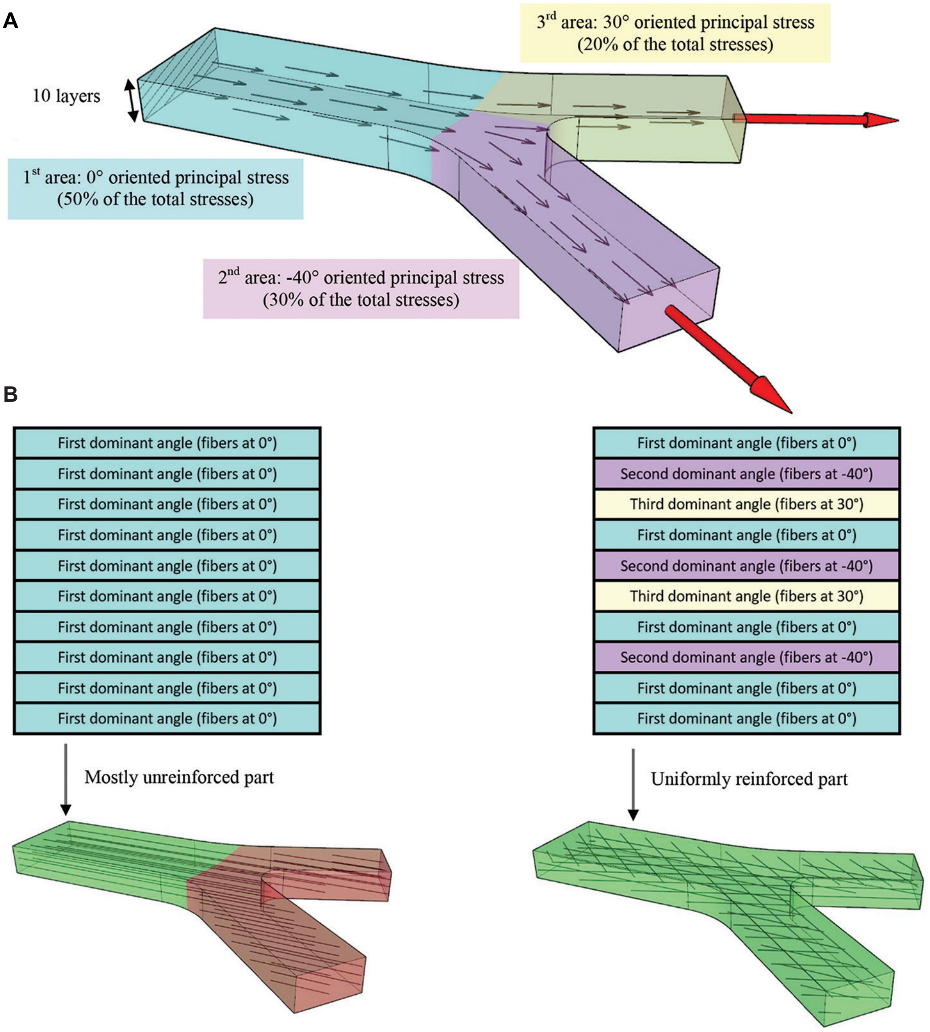

Figure 2. (A) Identification of the principal directions for a structure. (B) Fiber angle assignment for a layer-based optimized orientation (left) and a stack-based optimized orientation (right).

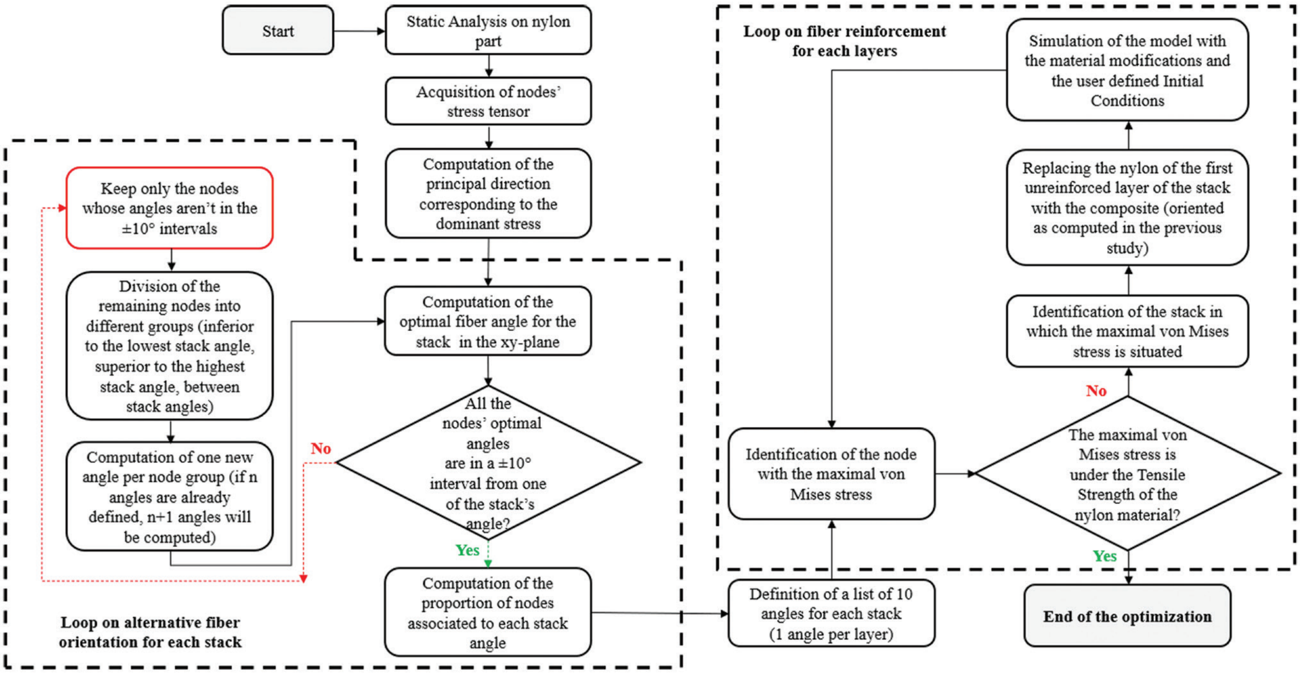

Figure 3. Flow chart of computation of the optimal stack's fiber angles and of the number of reinforced layers.

divided into two steps: The first one is to define an optimal fiber angle sequence for each stack of ten layers, and the second one is to optimize the number of reinforced layers.

2.2.1. Optimized stack fiber angles

The first step of our proposed method is to determine the optimal fiber angle based on the intuitive idea, considering that the optimal fiber orientation of the material should coincide with the absolute value of the dominant principal stress direction[16]. This method includes several substeps as shown in the workflow (Figure 3):

(i) A static analysis is first run on a whole part made of an isotropic material. This first calculation allows to determine the location where the deposit of fibers is needed to reinforce the stiffness of the part. After this static analysis is performed, the Cauchy stress tensor of each node is obtained.

(ii) The diagonalization of the Cauchy stress tensor gives the three principal stresses and the three principal directions. As the fibers in a composite are efficient for tensile or compressive loads, the first principal stress (tensile stress) is compared to the absolute value of the third principal stress (compressive if negative) to determine which of these two situations should be considered.

(iii) The principal direction corresponding to the dominant stress in absolute value between the first and third principal stress is used to compute the fiber orientation. The principal direction is projected on the xy-plane (perpendicular to the stacking direction z) because the current commercial manufacturing process does not allow printing continuous fibers in 3D orientations but only in 2D layers. The angle between this projected direction and the X-axis (considered parallel to a 0° fiber's orientation) is computed at each node of the mesh. The optimal fiber angle of the stack is the mean value of the node's fiber angles, weighted by the dominant principal stress value of each node.

(iv) To account for a possible deviation around the mean value calculated in step (iii), the algorithm determines which node has a fiber angle more than 10° degrees greater or lower than this mean value. Note that the value of 10° can be decreased at will by the user, but it should not be increased, as it has been found that the strength and the stiffness fall quickly when the angle between the fibers and the load exceed 10°. The remaining nodes are divided into two areas (upper and lower to the mean value), giving two new mean angles (Figure 4). While node's fiber angles are not in

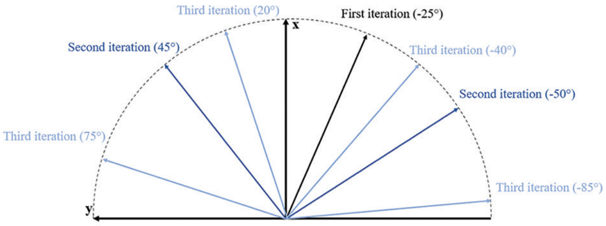

Figure 4. Computation of the stack's fiber angles iteration by iteration.

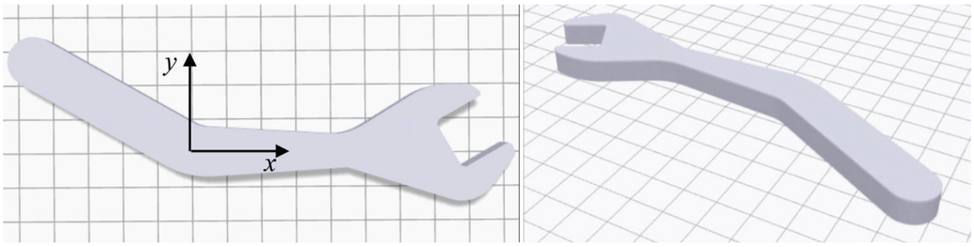

Figure 5. Top (left) and isometric (right) views of the wrench.

the interval of 10° width around the mean value, a new iteration is made.

Hence, a sequence of 10 fiber angles for each stack is obtained at the end of this first step. This result is used as an input for the second step.

2.2.2. Optimized number of reinforced layers

Once the optimal fiber's orientation has been computed inside each stack, it is necessary to reduce as much as possible the number of reinforced layers because continuous fiber-reinforced filament is a more expensive and heavier material compared to the nylon, which is also available with the Markforged X7 printer used in this work. To perform this cost reduction, a multi-layered finite element model only containing nylon at the beginning is used. A first computation provides the stacks where the maximal von Mises stress is located inside the nylon layers. While this maximal von Mises stress is higher than the tensile strength of the nylon, the material of the first unreinforced layer of the stack is replaced by the composite, oriented with the angle computed for this layer in the previous study. If there are locations where the von Mises stress is higher than the tensile strength of the nylon, the loop starts again.

3. Case study

The specific case of a wrench, which is an easy-to-print part (Figure 5), is considered. The crooked handle, with an angle of 30° between the two sections, makes the stress flow more complex and more interesting to study than a straight handle with unidirectional fiber reinforcement. Intuitively, the best way to enhance the stiffness of the wrench would be to reinforce equally the two sections, which would result in a 0°/−30° laminate. However, we will see in the next section that two additional angles calculated by our algorithm play a key role in the stiffness improvement.

3.1. Numerical results

The wrench is locked on the faces, which are supposed to be in contact with the screw, and a force is applied on the top of the handle (Figure 6). These boundary conditions correspond to the mechanical tests that we performed on the printed part.

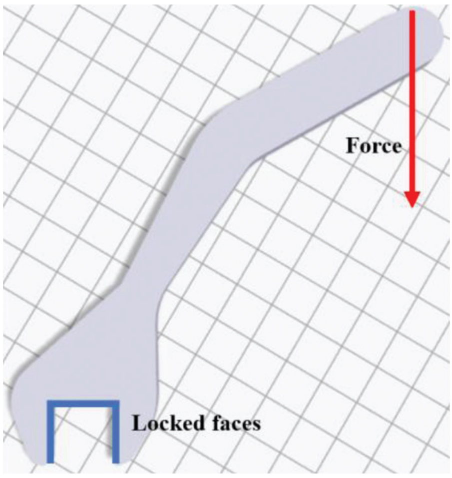

Figure 6. Mechanical model of the wrench.

The optimization model presented in section 2.2 gave the same fibers angle repartition for each stack with the following distribution: 2° (70%), −33° (10%), −17° (10%), and 13° (10%). The two angles of 0° and −30° that could be guessed intuitively were therefore found by the first step of the optimization algorithm depicted in Figure 3 with an angle of 2° close to 0° and an angle of −33° close to −30°. Since the stress' magnitudes were higher in the horizontal section of the handle (frame no. 2 in Figure 7) compared to the ones in the inclined section of the handle (frame no. 1 in Figure 7), the angle of 2° was logically more represented (seven times) than the angle of −33° corresponding to the inclined section. It is also important to note that the model gave two other angles (13° and −17°) corresponding to the stress fields inside of the wrench's head (frames no. 3 and no. 4, respectively, in Figure 7). The tests performed on the printed part demonstrated that these two additional angles that cannot be predicted without the help of an optimization algorithm play a key role to stiffen the wrench.

3.2. Tests on printed parts

To check whether the proposed method leads to an improvement of the performances of the wrench, two

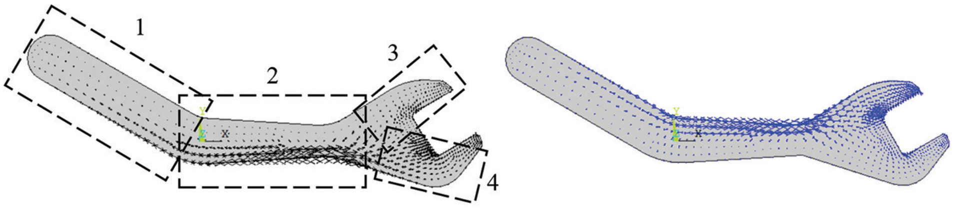

Figure 7. Distribution of the principal directions. Left: Tensile stress. Right: Compressive stress.

sets of printed parts were tested and then compared. The first set was built with an alternation of –30° oriented fibers (Figure 8A) and 0° oriented fibers (Figure 8B), corresponding to the intuitive fiber orientation. The second set has an alternation of the optimized angles computed in section 3.1 with the corresponding percentage: Seven layers with 2° oriented fiber, one layer at –33°, one layer at –17° and one layer at 13°. The parts were printed with a Markforged X7 printer using a continuous carbon fiber filament (blue routes on Figure 8). A nylon filament (white routes on Figure 8) was used for the roof and floor layers, which are mandatory with this printer.

Each wrench contains the same fiber content, only the orientation of the fiber changes. To be able to estimate the dispersion on the test results, three wrenches were printed for each fiber laminate. The six parts were tested with a compressive plate set on a Lloyds Instruments LR 50K. The wrench's head was locked inside a vice and leant on a steel plate to be locked vertically (Figure 9).

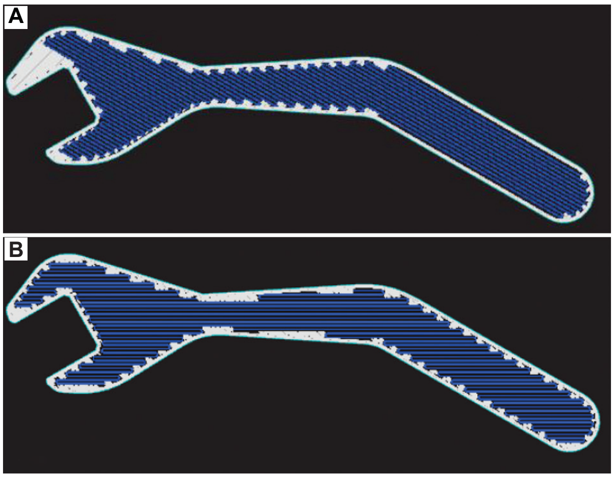

Figure 8. Printing routes with –30° oriented fibers (A) and 0° oriented fibers (B).

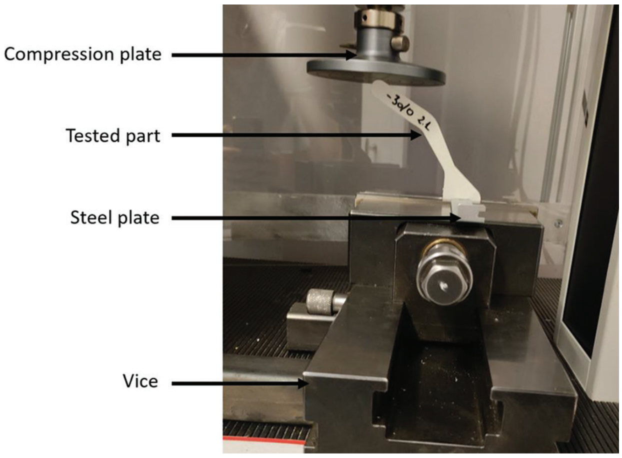

Figure 9. Testing setup.

Figure 10 shows the force-displacement curves of the six tested parts. There is a low dispersion in the results from one part to another of the same batch, which makes the results relevant. It appears that the optimized parts are stiffer than the non-optimized ones. In fact, the optimization of the layers' fiber angles has increased the stiffness of the printed parts by a significant improvement of 18%. This proves the usefulness of the optimization process compared to an intuitive reinforcement (0°/–30°).

3.3. Comparison with an optimization model

To check whether our quick method gives a result close to the optimal solution, we compared it to a solution obtained with an optimization model.

A direct optimization model with a Non-linear Programming Quadratic Line Search (NLPQL) algorithm was used with the Ansys Workbench software. The objective is to minimize the maximal displacement. Each layer's angle was set as a parameter initialized to 0° with a range of variation between –90° and 90°. The main issue, which led us to develop the quick method presented before in the first place, is that it is difficult to implement this model with many parameters. In our case, the wrench was built with 60 layers, which would require 60 parameters as well. However, the mechanical case was close to a 2D problem, as the load was set in the XY-plane. This was confirmed by the fact that our code gave the same angle sequence for each stack. Thus, the direct optimization method was applied on only ten layers of the wrench. Figure 11 shows the convergence of the model, which required 11 iterations to obtain the optimal (i.e., the lowest) maximal displacement within the part. Hence, a sequence of 10° was

Table 1. Comparison of the two optimization methods

Comparison criteria	Direct optimization (NLPQL)	Fast layering optimization
Computation time	> 5 h	16 s
Resulting layering	−30°/6°/0°/−9°/20°/ −2°/−3°/14°/−4°/−33°	−2°/−28°/−20°/−15°/−11°/ −6°/6°/12°/−2°/−2°
Resulting maximal displacement	4.9554×10^{-5} m	5.4166×10^{-5} m (+9%)

NLPQL: Non-linear Programming Quadratic Line Search

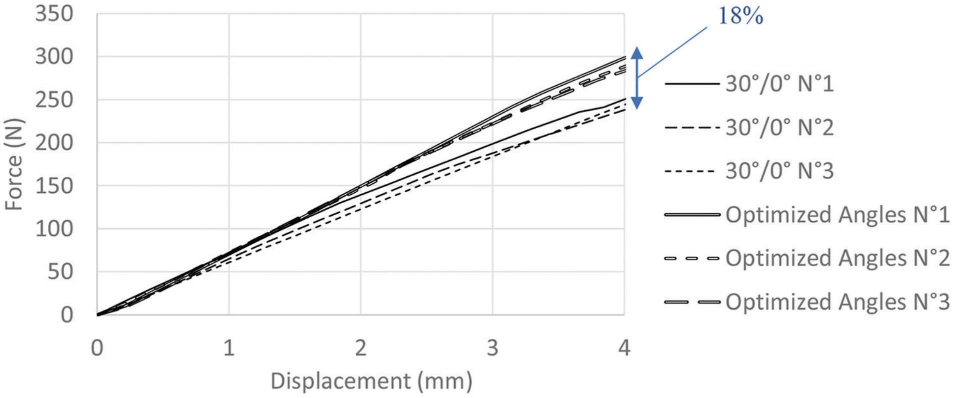

Figure 10. Force-displacement curves of the six tested parts.

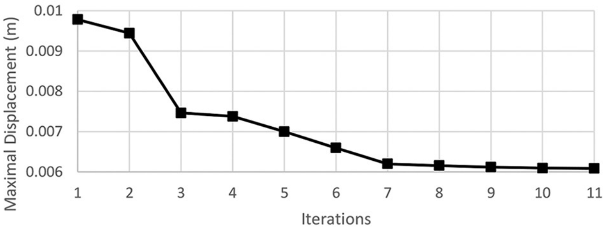

Figure 11. Convergence of the direct optimization model.

found. Then, this sequence was repeated 6 times to fill the geometry of the wrench.

A simulation on a part with the directly optimized angle sequence showed that the stiffness of the wrench is only 9% higher than the wrench obtained with our quick method, with a much higher computation time (Figure 12 and Table 1). If finding the best solution is requested, the NLPQL method is suitable but, if the goal is to quickly find an improved solution, the approach proposed in this paper is a good compromise between computation time and the search for the best solution. It is also important to note that this comparison was possible because the case was close to a 2D case. A more complex case would be harder to optimize with a gradient method due to the number of design parameters it would require. Ansys Workbench software, which was used for this study, limits, for example, the number of parameters to 20 for automatically computed Design of Experiments.

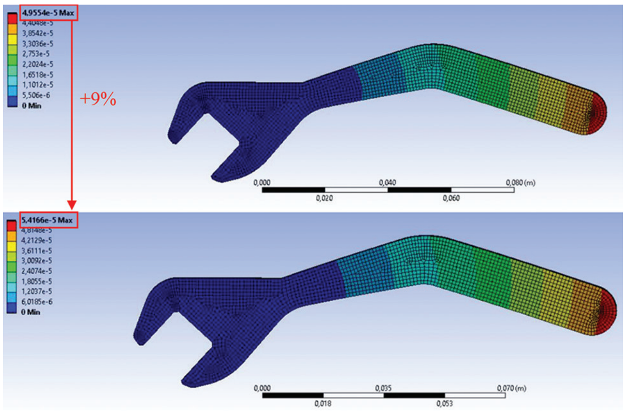

Figure 12. Displacement fields of the two compared wrenches: direct optimized (top) and quick optimized (bottom).

Hence, our quick method is a good compromise between performance and design time, as it led to a part that is only 9% less stiff than the optimal part within a minimal computation time.

4. Conclusions

A method to quickly optimize the fiber's orientations of a MEX-manufactured continuous fiber-reinforced composite was implemented with the finite element method in the Ansys Mechanical environment of programming. The use of stack-based model helped to reduce the numerical simulation time, which made the application of a 2D method inside a 3D part possible. Moreover, the proposed model is useful to consider not only one but several reinforcement directions.

The method relies on the fact that a continuous fiber is optimally used when oriented parallel to the stress flow. This is due to the high anisotropy of fibers and their exceptional tensile properties compared to polymers. Yet, continuous fiber-reinforced filaments are expensive, so this work also proposes a method to optimize the number of reinforced layers and therefore optimize the cost of the manufactured parts. The application of the stack-based layering optimization on printed parts gave satisfying results, with the stiffness of the parts being only 9% lower than the one found with a time-costly direct optimization method.

The next step would be to consider a more flexible approach based on curved fiber routes rather than unidirectional ones. The development of slicer software to customize the fiber routes is warranted since this flexibility has yet to be incorporated into the commercial printers.

Acknowledgments

None.

Funding

This research did not receive any specific grant from funding agencies in the public, commercial, or not-for-profit sectors.

Conflict of interest

The authors declare that they have no known competing financial interests or personal relationships that could have appeared to influence the work reported in this paper.

Author contributions

Conceptualization: Valentin Marchal, Yicha Zhang, Nadia Labed, and François Peyraut
Data curation: Valentin Marchal
Formal analysis: Valentin Marchal, Nadia Labed, and François Peyraut
Funding acquisition: Yicha Zhang
Investigation: Valentin Marchal and Rémy Lachat
Methodology: All authors
Software: Valentin Marchal
Supervision: Yicha Zhang, Nadia Labed, and François Peyraut
Validation: Rémy Lachat
Visualization: Valentin Marchal
Writing – original draft: Valentin Marchal, Yicha Zhang, and François Peyraut
Writing – review and editing: All authors

Ethics approval and consent to participate

Not applicable.

Consent for publication

Not applicable.

Availability of data

The data are not publicly available because the research work was carried out in a laboratory whose scientific developments are protected and cannot be transferred. However, the experimental data proving the relevance of the proposed numerical method are available from the corresponding author on reasonable request.

References

1. Zheng H, Zhang W, Li B, *et al.*, 2022, Recent advances of interphases in carbon fiber-reinforced polymer composites: A review. *Compos B Eng*, 233: 109639.

   https://doi.org/10.1016/j.compositesb.2022.109639

2. Li J, Durandet Y, Huang X, *et al.*, 2022, Additively manufactured fiber-reinforced composites: A review of mechanical behavior and opportunities. *J Mater Sci Technol*, 119: 219–244.

   https://doi.org/10.1016/j.jmst.2021.11.063

3. Liao G, Li Z, Cheng Y, *et al.*, 2018, Properties of oriented carbon fiber/polyamide 12 composite parts fabricated by fused deposition modeling. *Mater Des*, 139: 283–292.

   https://doi.org/10.1016/j.matdes.2017.11.027

4. Yan C, Hao L, Xu L, *et al.*, 2011, Preparation, characterisation and processing of carbon fibre/polyamide-12 composites for selective laser sintering. *Compos Sci Technol*, 71: 1834–1841.

   http://dx.doi.org/10.1016/j.compscitech.2011.08.013

5. Goodridge RD, Shofner ML, Hague RJM, *et al.*, 2011, Processing of a polyamide-12/carbon nanofiber composite by laser sintering. *Poly Test*, 30: 94–100.

   http://dx.doi.org/10.1016/j.polymertesting.2010.10.011

6. Jansson A, Pejryd L, 2016, Characterisation of carbon fibre-reinforced polyamide manufactured by selective laser sintering. *Addit Manuf*, 9: 7–13. http://dx.doi.org/10.1016/j.addma.2015.12.003

7. Hofstätter T, Pedersen DB, Tosello G, *et al.*, 2017, Applications of fiber-reinforced polymers in additive manufacturing. *Procedia CIRP*, 66: 312–316.

   https://doi-org.ezproxy.utbm.fr/10.1016/j.procir.2017.03.171

8. Tekinalp HL, Kunc V, Velez-Garcia GM, *et al.*, 2014, Highly oriented carbon fiber-polymer composites via additive manufacturing. *Compos Sci Technol*, 105: 144–150.

   http://dx.doi.org/10.1016/j.compscitech.2014.10.009

9. van de Werken N, Tekinalp H, Khanbolouki P, *et al.*, 2020, Additively manufactured carbon fiber-reinforced composites: State of the art and perspective. *Addit Manuf*, 31: 100962.

   https://doi.org/10.1016/j.addma.2019.100962

10. Tian X, Liu T, Yang C, *et al.*, 2016, Interface and performance of 3D printed continuous carbon fiber reinforced PLA composites. *Composites Part A*, 88: 198–205.

    http://dx.doi.org/10.1016/j.compositesa.2016.05.032

11. Aravind AU, Bhagat AR, Radhakrishnan R, *et al.*, 2020, A novel use of twisted continuous carbon fibers in additive manufacturing of composites. *Materials Today: Proceedings.*

    https://doi.org/10.1016/j.matpr.2020.07.665

12. Material Datasheet: Composites, Markforged. Available from: https://www-objects.markforged.com/craft/materials/compositesv5.2.pdf [Last accessed on 2022 Dec 13].

13. Mahajan C, Cormier D, 2015, 3D Printing of Carbon Fiber Composites with Preferentially Aligned Fibers. Proceedings of the 2015 Industrial and Systems Engineering Research Conference.

14. Goh GD, Toh W, Yap YL, *et al.*, 2021, Additively manufactured continuous carbon fiber-reinforced thermoplastic for topology optimized unmanned aerial vehicle structures. *Composites Part B*, 216: 108840.

    https://doi.org/10.1016/j.compositesb.2021.108840

15. Lewicki JP, Rodriguez JN, Zhu C, *et al.*, 2017, 3D-Printing of meso-structurally ordered carbon fiber/polymer composites with unprecedented orthotropic physical properties. *Sci Rep*, 7: 43401.

    https://doi.org/10.1038/srep43401

16. Zhou Y, Nomura T, Saitou K, 2018, Multi-component topology and material orientation design of composite structures (MTO-C). *Comput Methods Appl Mech Eng*, 342: 438–457.

    https://doi.org/10.1016/j.cma.2018.07.039

17. Ding H, Xu B, 2021, A novel discrete-continuous material orientation optimization model for stiffness-based concurrent design of fiber composite. *Compos Struct*, 273: 114288.

    https://doi.org/10.1016/j.compstruct.2021.114288

18. Li Y, Xu K, Liu X, *et al.*, 2021, Stress-oriented 3D printing path optimization based on image processing algorithms for reinforced load-bearing parts. *CIRP Ann Manuf Technol*, 70: 195–198.

    https://doi.org/10.1016/j.cirp.2021.04.037

19. Safonov AA, 2019, 3D topology optimization of continuous fiber-reinforced structures via natural evolution method. *Compos Struct*, 215: 289–297.

    https://doi.org/10.1016/j.compstruct.2019.02.063

20. Nomura T, Kawamoto A, Kondoh T, *et al.*, 2019, Inverse design of structure and fiber orientation by means of topology optimization with tensor field variables. *Composites Part B*, 176: 107187.

    https://doi.org/10.1016/j.compositesb.2019.107187

21. Jung T, Lee J, Nomura T, *et al.*, 2022, Inverse design of three-dimensional fiber-reinforced composites with spatially-varying fiber size and orientation usign multiscale topology optimization. *Compos Struct*, 279: 114768.

    https://doi.org/10.1016/j.compstruct.2021.114768

ACCSCIENCE PUBLISHING

Materials Science in Additive Manufacturing

ORIGINAL RESEARCH ARTICLE

3D-Printed disposable nozzles for cost-efficient extrusion-based 3D bioprinting

Hamed I. Albalawi[1,2,3], **Zainab N. Khan**[1], **Ranim H. Rawas**[1,2,3], **Alexander U. Valle-Pérez**[1,2,3], **Sherin Abdelrahman**[1,2,3], and **Charlotte A. E. Hauser**[1,2,3]*

[1]Laboratory for Nanomedicine, Division of Biological and Environmental Science and Engineering (BESE), King Abdullah University for Science and Technology, Thuwal 23955-6900, Saudi Arabia

[2]Computational Bioscience Research Center (CBRC), King Abdullah University of Science and Technology, Thuwal 23955, Saudi Arabia

[3]Red Sea Research Center, King Abdullah University of Science and Technology, Thuwal 23955, Saudi Arabia

Abstract

3D bioprinting has significantly impacted tissue engineering with its capability to create intricate structures with complex geometries that were difficult to replicate through traditional manufacturing techniques. Extrusion-based 3D bioprinting methods tend to be limited when creating complex structures using bioinks of low viscosity. However, the capacity for creating multi-material structures that have distinct properties could be unlocked through the mixture of two solutions before extrusion. This could be used to generate architectures with varying levels of stiffness and hydrophobicity, which could be utilized for regenerative medicine applications. Moreover, it allows for combining proteins and other biological materials in a single 3D-bioprinted structure. This paper presents a standardized fabrication method of disposable nozzle connectors (DNC) for 3D bioprinting with hydrogel-based materials. This method entails 3D printing connectors with dual inlets and a single outlet to mix the material internally. The connectors are compatible with conventional Luer lock needles, offering an efficient solution for nozzle replacement. IVZK (Ac-Ile-Val-Cha-Lys-NH2) peptide-based hydrogel materials were used as a bioink with the 3D-printed DNCs. Extrusion-based 3D bioprinting was employed to print shapes of varying complexities, demonstrating potential in achieving high print resolution, shape fidelity, and biocompatibility. Post-printing of human neonatal dermal fibroblasts, cell viability, proliferation, and metabolic activity were observed, which demonstrated the effectiveness of the proposed design and process for 3D bioprinting using low-viscosity bioinks.

Keywords: 3D bioprinting; Nozzle connecter; Extrusion-based 3D printing; 3D-printed nozzle; Disposable nozzles

***Corresponding author:**
Charlotte A. E. Hauser
(charlotte.hauser@kaust.edu.sa)

Citation: Albalawi HI, Khan ZN, Rawas RH, *et al.*, 2023, 3D-Printed disposable nozzles for cost-efficient extrusion-based 3D bioprinting. *Mater Sci Add Manuf,* 2(1): 52. https://doi.org/10.36922/msam.52

Received: February 15, 2023

Accepted: March 6, 2023

Published Online: March 21, 2023

Copyright: © 2023 Author(s). This is an Open Access article distributed under the terms of the Creative Commons Attribution License, permitting distribution, and reproduction in any medium, provided the original work is properly cited.

Publisher's Note: AccScience Publishing remains neutral with regard to jurisdictional claims in published maps and institutional affiliations.

1. Introduction

Three-dimensional (3D) printing is a manufacturing technique that can produce 3D objects in a layer-by-layer fashion using computer-aided design (CAD). It has been adopted by many industries, including education, aerospace, transportation, biomedicine, and healthcare[1-4]. More recently, 3D printing has been applied for sustainable and eco-friendly coral restoration[5-7]. One of the main branches of 3D printing technology is 3D bioprinting, which fabricates cell-based tissue constructs for tissue engineering and regenerative medicine[8]. 3D bioprinting is revolutionizing tissue engineering with its ability to create cell-integrated structures with complex geometries, which were previously unattainable with traditional manufacturing methods. Nevertheless, 3D bioprinting technology is still confined by certain constraints. One significant constraint is related to the 3D printing of structures similar to the complex hierarchical structure of natural tissues[9]. Various 3D printing technologies are used today in 3D bioprinting, such as extrusion-based and vat polymerization.

Vat polymerization is one of the 3D printing technologies used in fabricating tissue engineering scaffolds, relying on a light source, and polymerization reaction to cure a photocurable bio-based resin[10]. The materials utilized in vat polymerization for 3D bioprinting are usually photocurable resins and photocrosslinkable hydrogels. Using photocrosslinkable hydrogel in vat polymerization can enable cell encapsulation and replicate the extracellular matrix found in native tissue[11]. Elomaa *et al.*[12] developed a bioactive photocrosslinkable resin derived from a decellularized small intestine submucosa for vat polymerization-based 3D bioprinting. The developed bioactive resin offers a printable material that acts as a suitable medium for fabricating a complex 3D tissue model. However, vat polymerization application in fabricating cell-based scaffolds is limited due to the high ultraviolet (UV) exposure intensity and the cytotoxicity effect of polymerization reaction[13]. Consequently, this technique is limited to fabricating acellular scaffolds that can only be seeded with cells post-printing. Therefore, other 3D printing technologies can provide the necessary freedom in fabricating and mimicking 3D tissue models.

Extrusion-based 3D printing is a technique that is widely used in fabricating cell-based scaffolds in the 3D bioprinting process[14,15]. More recently, there has been an interest to integrate smart and intelligent biomaterials with 3D printing technology[16]. A pressure-based or mechanical feeder is used to extrude material through a nozzle[17]. While this layer-by-layer approach facilitates fabrication, it has limitations with low-viscosity materials when creating complex structures due to resolution constraints and instantaneous gelation properties of soft matter bioinks, such as peptide hydrogels. On the other hand, high-viscosity biomaterials produce a high shear force, resulting in a high degree of cell destruction during extrusion. Often, cross-linking methods are used to reduce the viscosity of biomaterials and improve cell viability[18]. However, alternative solutions could be developed by maximizing the instantaneous gelation property of low-viscosity bioinks to reduce shear force in the nozzle and eliminate post-printing crosslinking procedures. For instance, several low-viscosity bioinks for 3D bioprinting and cell culture have been developed[19,20]. Incorporating the mixing of multiple solutions before extrusion offers the potential for creating structures with various properties. Multi-material bioinks consisting of solutions such as proteins, hydrogels, and cells can create a more realistic 3D-bioprinted structure that could be advantageous for tissue engineering applications.

In multiple studies, extrusion-based 3D bioprinting and customized 3D-printed parts have been combined to create tissue scaffolds with desired characteristics. For instance, Khan *et al.*[21] combined vat polymerization and extrusion-based 3D bioprinting to create a complex human-like ear structure. Likewise, Abdelrahman *et al.* implemented a hybrid 3D bioprinting and vat polymerization approach for the modeling of Parkinson's disease using dopaminergic neurons[22]. Furthermore, Scott *et al.*[23] have 3D-printed a nozzle to enable multi-material 3D bioprinting using an extrusion-based system. This allows the nozzle to mix multiple solutions and create a multi-material structure. Through further research, researchers have looked into the advantages of merging various 3D printing techniques for utilization in different applications[6,24]. It has been demonstrated that the convergence of 3D printing techniques can upgrade 3D bioprinters and exploit material characteristics for enhanced printability and resolution.

Herein, we propose a design and fabrication process for disposable nozzle connectors (DNC) to accelerate the nozzle-making process for low-viscosity bioinks. It was curated to allow instantaneous mixing of three solutions for the formulation of a continuous bioink thread embedded with cells. The connectors were designed to easily fit into standard Luer lock needle tips, making them versatile and compatible with a wide range of mixing requirements and bioink viscosities. Our design parameters were set for the material characteristics of peptide bioinks, and several tests were performed to assess workability and printability. With a thorough evaluation, the developed DNC proved to be cost-effective, reproducible, and highly practical for standardization.

2. Methods

With the assistance of vat polymerization technology, several DNCs were designed to suit peptide bioink requirements and 3D-printed with varied final diameters and mixing regions. An ideal design was selected based on ease of flow and effective gelation. The 3D-printed DNCs were assembled with Luer lock needle tips to create fully functional nozzles with multiple inlets and a single outlet, as shown in Figure 1. A range of constructs were then 3D-bioprinted through a microfluidic syringe pump-based extrusion system with peptide-based and live cells. To determine the feasibility of the proposed connectors, an evaluation of the 3D-bioprinted construct was conducted in terms of gelation continuity, printability, biocompatibility, and shape fidelity. The methods applied for designing, fabricating, assembling, and evaluating DNCs for cellular 3D bioprinting with peptide bioinks are detailed in the following.

2.1. Designing DNC

To ensure uniformity, the connectors were designed using the NX CAD software with millimeter precision. Considering the desired needle tip diameter and angle, the connector was designed to fit into a Luer lock needle tip. By design, the two inlets of the connector merge into one channel considering the volume of the two solutions flowing inside the connector. This was done to reduce any material clogging before extrusion. The mixing region length was taken from a previous study to complement the characteristic requirements of our peptide hydrogels for 3D bioprinting[25-27]. This can be modified based on the characteristics of the desired printing materials. The DNC was designed with an additional holder for the cells inlet to enable extruding cells at the tip of the nozzle. An ideal design was narrowed down based on ease of flow through the mixing region while maintaining an inlet angle closest to 90° angle.

2.2. 3D printing connectors using vat polymerization

Connectors were 3D-printed using FormLabs 3B 3D printer in the recommended settings for the white polymer resin. Before 3D printing, the design files were converted to the STL format and then processed with PreForm software to prepare for slicing. The materials were chosen, and the model configuration took place during this process. Following the printing process, the 3D-printed model was washed with isopropanol for 30 min and then cured at a temperature of 40°C for 60 min using the Form Washer and Form Cure post-processing devices.

2.3. Parameter optimization for 3D bioprinting

For seamless material extrusion with the DNC, optimization experiments were run with an in-house developed robotic 3D bioprinter to evaluate gelation, printability, and shape fidelity. For all experiments, 13 mg/mL IVZK (Ac-Ile-Val-Cha-Lys-NH2) peptide and ×7 phosphate-buffered saline (PBS) were used. The cells inlet was pumped with ×1 PBS for acellular simulation tests. A gelation continuity test was conducted by running the microfluidic pumps connected to the DNC at a range of flow rates for peptide and PBS, to determine optimal gelation parameters. A g-code file for a continuous 5-segment line was used to trace any clumps or clogs and gelation time was recorded.

To assess printability, a six-layer semi-filled cube was 3D-printed with the DNC. Based on the gelation continuity test, the optimized flow rates were set to 55 μL/min, 20 μL/min, and 20 μL/min for peptide, PBS, and the cells inlet, respectively. Constructs were evaluated for print shape, consistent formation of bioink thread, and continuous layer deposition.

2.4. Creating acellular 3D-printed scaffolds

Finally, to evaluate the shape fidelity of bioprinted constructs, acellular samples were printed and observed for print resolution and mechanical stiffness. The DNC was mounted on the robotic 3D bioprinter to print hollow cylinders of $10 \times 10 \times 13$ mm^3 and grid structures of 20 mm^2. To enhance flow for longer periods of time, automated time-dependent pumping was exploited by programming the microfluidic pumps with alternating square wave flow profiles. Based on the optimized parameters reported previously, the square wave flow profile for the peptide hydrogel solution was set to a range of 50 – 55 μL/min with a 75% duty cycle and a period of 115 s. For the PBS, the square wave flow profile was set to a range of 15 – 20 μL/min with a 25% duty cycle and a period of 115 s[28].

2.5. 3D cell culture

The biocompatibility of peptide hydrogel biomaterials of IVZK peptide was tested with human neonatal dermal fibroblasts (HDFn). HDFn was cultured in a 3D-bioprinted construct with self-assembling ultra-short IVZK peptide-based hydrogels. An optimal gelation concentration of the IVZK peptide (13 mg/mL) was used. Purified and lyophilized peptide powder was sterilized using a UV light for 30 min before each experiment.

HDFn was obtained from Thermo Fisher Scientific, and cell suspensions were used after seven passages for every experiment. First, 1 mL of Dulbecco's modified eagle medium (DMEM, ×1) was supplemented with 4.5 g/L glucose, 1-glucamine, sodium pyruvate, 10% fetal bovine serum (FBS), and 1% penicillin/streptavidin (10,000 units/mL). After adding cells to the growth medium, the mixture was centrifuged for 5 min (250 ×*g*), at room temperature, to remove the DMSO storage buffer from the stock solution. Then, cells were cultured in 75 mL of growth medium within cell-treated flasks and incubated for 2 days at 37°C. After incubation, the cells were viewed under a microscope to determine their confluency. Then, the growth medium was removed and approximately 5 mL

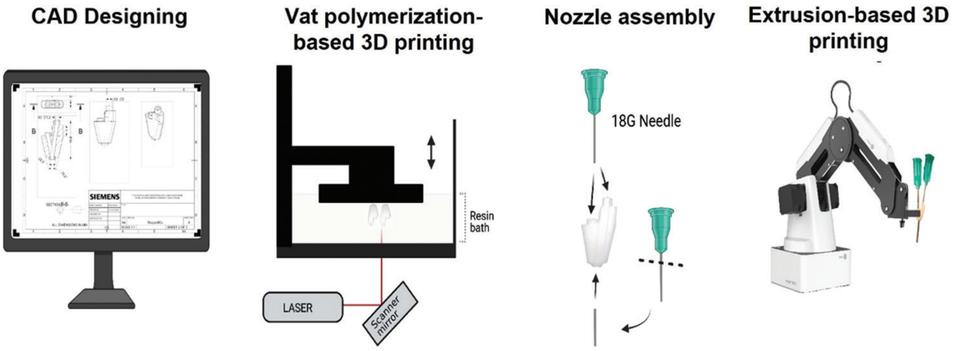

Figure 1. A schematic view of the fabrication process, including CAD designing, 3D printing of DNCs using vat polymerization, DNC nozzle assembly, and extrusion-based 3D bioprinting using the assembled nozzle.
CAD: Computer-aided design; 3D: Three-dimensional; DNC: Disposable nozzle connectors.

of 0.05% trypsin-ethylenediaminetetraacetic acid (×1) was added to the cells to detach them from the surface of the flask. The flask was then incubated at 37°C for 5 min. After the incubation period, the cells were examined under a microscope to confirm detachment. Finally, the solution was transferred into a clean 50-mL centrifuge tube with 10-mL of fresh DMEM (×1). The addition of DMEM (×1) inactivated the trypsin. Then, the cell suspension was centrifuged as described before, and the supernatant was removed. Following this, ×2 PBS was added to the cell pellet to achieve a final cell concentration of 3 million/mL with gentle mixing. The cell suspension with a volume of 0.5 mL was prepared and loaded into the cells inlet pump for bioprinting the 3D constructs.

2.6. 3D Bioprinting of cellular constructs

The robotic 3D bioprinter was mounted with a sterilized disposable nozzle and prepared for 3D bioprinting. Initially, IVZK peptide (13 mg/mL) and ×7 PBS were loaded in Pump 1 and Pump 2 and set to a flow rate range of 50 – 55 µL/min and 15 – 20 µL/min, respectively. Pump 3 was loaded with ×1 PBS and a volume of 0.5 mL HDFn suspension. A six-layer cube with dimensions of 10 × 10 × 2 mm was loaded as g-code and 3D-bioprinted.

2.7. Cell viability testing

The viability of the cellular 3D constructs was examined using the Live/Dead Viability/Cytotoxicity Kit (ThermoFisher, USA). Here, calcein acetoxymethyl ester (Calcein-AM) was used to detect viable cells and ethidium homodimer-I (EthD-I) was used to detect dead cells. DMEM (×1) media was removed from the 3D constructs before the contents of the kit were added. Then, a staining solution of 2 µM calcein-AM and 4 µM of EthD-1 were dissolved in ×1 PBS and the solution was added to the 3D constructs and incubated for 30 min at room temperature. After the incubation period, stained cells were imaged with an EVOS microscope. The viability of HDFn was assessed after 1 and 3 days.

2.8. Cell proliferation assessment

The CellTiter-Glo® luminescent 3D cell viability assay was used to determine the proliferation rate of cells in 3D peptide constructs. An ATP bioluminescence assay works by detecting the presence of living cells in the sample through a bioluminescent signal from metabolically active cells. Dead cells do not produce such a signal since they are not metabolically active. The intensity of the signal is directly proportional to the amount of ATP present in a cell. A volume of the CellTiter-Glo® 3D reagent equivalent to that of the cell culture medium was added to a Petri dish and thoroughly mixed for 5 min, followed by an incubation period of 25 min at room temperature. The bioluminescent signals were read using a plate reader (PHERAstar FS, Germany). The metabolic activity of HDFn was evaluated after 1 and 3 days.

The robotic 3D bioprinter was programmed to deposit bioink and cells into a 96-well plate. This was achieved by mapping the wells in a teach-and-playback approach and setting point-to-point (PTP) positions. The same parameters were used as those optimized for 3D bioprinting. Flow rates of peptide, PBS, and cells were set to 330 µL/min, 120 µL/min, and 120 µL/min, respectively, and they were deposited in each well for 10 s to achieve a volume of 90 µl/well.

2.9. Cytoskeleton staining

Rhodamine phalloidin (Invitrogen, ThermoFisher, USA) was used to stain F-Actin (ex/em ~540 nm/~565 nm) in HDFn. First, culture media was removed; then, the cells were fixed using 4% methanol-free formaldehyde (Thermofisher, USA) for 30 min. The cells were then washed with ×1 PBS after discarding the fixation solution. Subsequently, the cells were incubated for 5 min in a pre-chilled cytoskeleton buffer containing 3 mM $MgCl_2$, 300 mM sucrose, and 0.5%

Triton X-100 in PBS. The cells were then incubated for 30 min at room temperature, in a blocking buffer containing 5% FBS, 0.1% Tween-20, and 0.02% sodium azide in ×1 PBS. Rhodamine-phalloidin (1:40 in ×1 PBS) was added to each well after discarding the blocking buffer. The cells were incubated for 1 h at room temperature. The cells were then washed with ×1 PBS and incubated for 5 min with 4′,6-diamidino-2-phenylindole (DAPI) and sterile water (1:2000, volume/volume). Images were obtained using an EVOS microscope with ×4 and ×10 magnification using absorption and emission parameters. Assessment of the cells' morphology was performed after 1 and 3 days.

3. Results and discussion

This study highlights the apparent advantages of a DNC extrusion system in terms of cost-effectiveness and rapid fabrication time. The use of resins for fabrication makes it extremely simple to modify, fabricate, and replace nozzles as needed without disrupting experiments. In addition, using a vat polymerization-based fabrication method ensures precision and reproducibility, which ensures consistent 3D bioprinting results compared to the inevitable variations in handmade nozzles.

3.1. Design and fabrication of DNC

The connectors were designed to be compatible with standard Luer lock needle tips, where the 18G needle, equivalent to 1.2 mm outer diameter, was used for both inlets and the outlet of the DNC. Furthermore, the two inlets were designed with an angle so that they merge into one outlet, as illustrated in Figure 2A. The minimal angle of the inlet needle placement reduces the possibility of clogging. The design used in this study included an external cell inlet holder used to extrude cells at the nozzle tip (Figure 2B, top). This enabled the deposition of cells into the construct after the gelation process occurred within the DNC mixing region. The DNC illustrated in Figure 2B (bottom) is for printing an acellular peptide-based scaffold.

The DNC STL files were printed with FormLabs 3B using the suggested FormLabs White Resin settings. To eradicate any residual resin, the connectors were post-processed using isopropanol. Subsequently, two 18G needles were inserted into the two inlets, and another 18G needle was cut and sanded to be inserted into the outlet. The needle assembly into the connector was done before the curing process to ensure a sealed fit. Due to the slight shrinkage of the printed models during the curing process, a tight fit between the connectors and needles was created. To finalize the assembly of the nozzle, an 18G needle was inserted into the DNC side holder for the cell's inlet (Figure 2C). The cumulative time taken for printing and curing a batch of 5 DNCs was estimated to be around 3 h.

3.2. Parameter optimization for 3D bioprinting

After fabricating the DNC, several parameters needed to be optimized to establish compatibility with peptide bioinks and our robotic 3D bioprinter. These included flow rate profiles, peptide and PBS concentration, and printing speed. Performance was evaluated by observing gelation continuity, printability, shape fidelity, and biocompatibility.

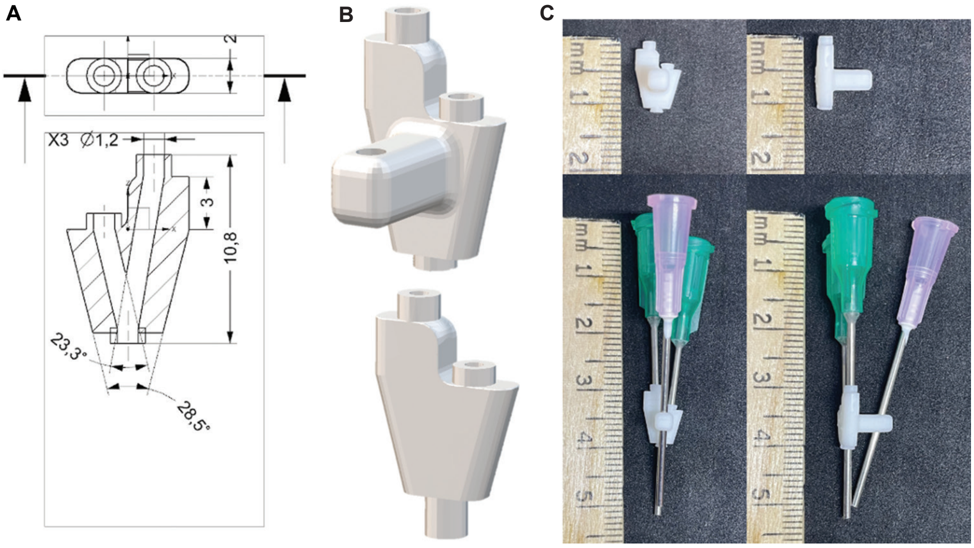

Figure 2. A visual representation of the DNC and the fabrication procedure of the nozzle. (A) A draft drawing showing the dimensions of the DNC and a cross-sectional view of the inlets and the outlet of the DNC, all in mm. (B) A CAD model of the two DNCs with and without the cell inlet holder. (C) The 3D-printed DNC with the needle assembly.
CAD: Computer-aided design; 3D: Three-dimensional; DNC: Disposable nozzle connectors.

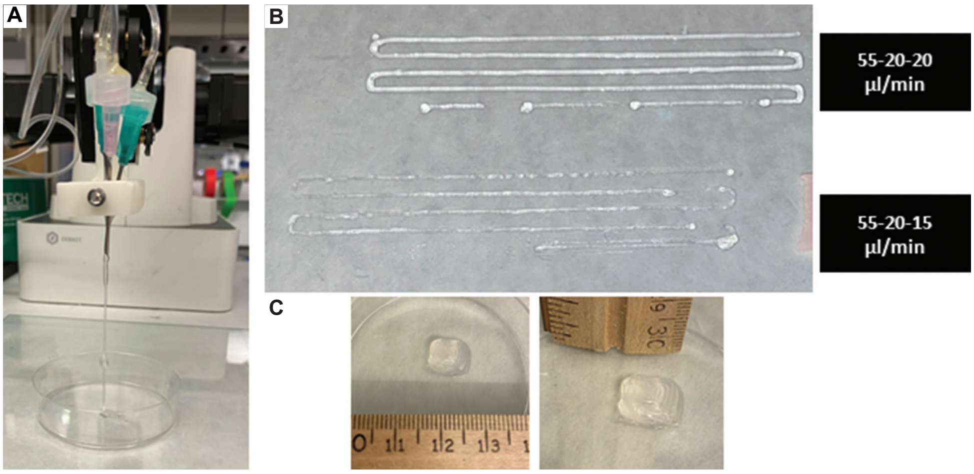

Figure 3. Gelation continuity tests of DNC. (A) Continuous extrusion of peptide bioink thread showing gelation and stiffness. (B) Extrusion of continuous five-segment line at different flow rates to optimize bioink formation. (C) Six-layer cubical constructs showing printability and layer deposition, top view, and side view.
DNC: Disposable nozzle connectors.

In terms of gelation continuity, the best flow rate profile was found to be 55 µL/min, 20 µL/min, and 20 µL/min for the peptide hydrogel, ×7 PBS, and ×1 PBS inlets, respectively. Different flow profiles were tested by printing a continuous 5-segment line, which visibly indicated the period of flow before clumps were formed from over-gelation. A visible thread of gel was also extruded and displayed gel continuity and stiffness, a prime indicator for printability (Figure 3A). Gelation time for the formation of a stable bioink thread was found to be approximately 81 s, which was relatively faster than homemade nozzles. Hence, the optimal flow rates were set according to these observations to be used for further printability assessments (Figure 3B). It was observed that lower flow rates resulted in insufficient flow, which was expected given the mixing region ratio. The gelation therein needed to be accelerated by increasing the overall flow to 95 µL/min.

A six-layer semi-filled cube of dimensions 10 × 10 × 2 mm was 3D-printed using the DNC. Based on the gelation continuity test, the optimized flow rates were set to 55 µL/min, 20 µL/min, and 20 µL/min for the three inlets of peptide, ×7 PBS, and ×1 PBS, respectively. The cubical shape was found to be well maintained with defined lines (Figure 3C, Cube). No clumps or clogs were observed during printing – A key marker of the nozzle performance through consistent formation of bioink thread. In addition, the construct layers piled up smoothly without any sagging, which also indicated continuous layer deposition. For further verification, the peptide flow rate was increased to 60 µL/min for another construct, but results showed lower printing resolution due to several clumps, most likely due to the slightly accelerated gelation.

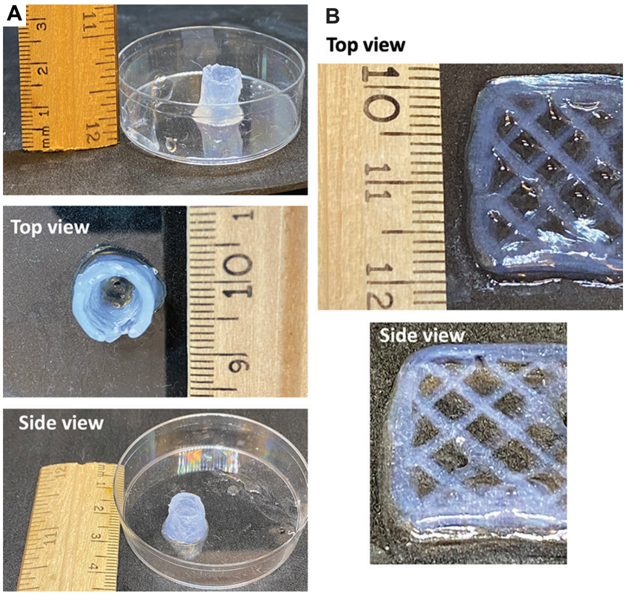

Figure 4. 3D printing of peptide-based acellular constructs with DNC. Different levels of shape complexity were selected: Hollow cylinder 10 × 10 × 13 mm^3 (A), and fine grid 20 mm^2 (B).
3D: Three-dimensional; DNC: Disposable nozzle connectors.

3.3. 3D printing shape fidelity and resolution

To test the DNC, several acellular constructs with different levels of complexity were printed. In addition, automated square wave flow profiles were programmed for the microfluidic pumps to enable smoother flow for longer periods. This was found to ease printing considerably, allowing for 20-min prints without flow interruptions or the need for user intervention to manually alter flow rates. First, a hollow cylinder of 10 × 10 × 13 mm^3 was printed (Figure 4A). This highlighted the layer-by-layer

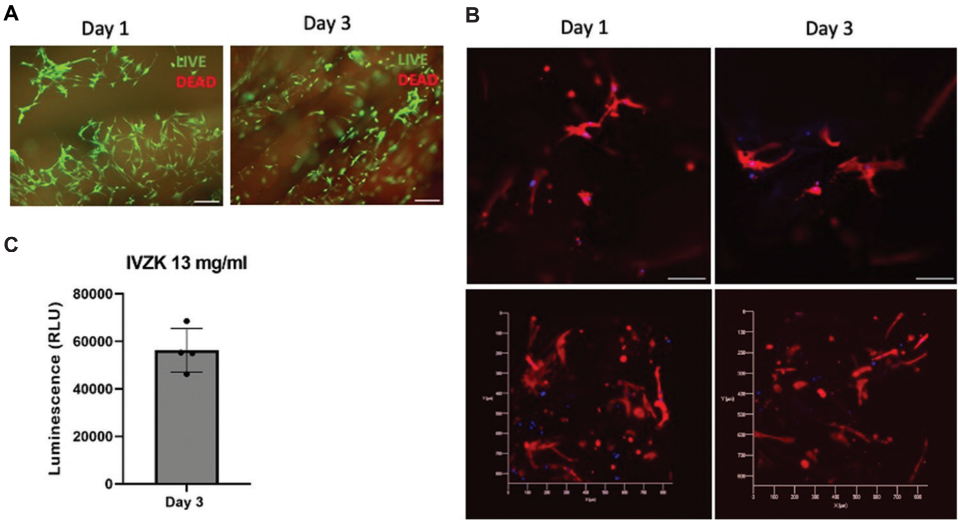

Figure 5. Biocompatibility assays of human neonatal dermal fibroblasts (HDFn) in three-dimensional (3D) IVZK peptide hydrogels constructs were tested for both days 1 and 3 to determine their growth rate and viability. (A) Cells stained with Calcein-AM (green: Live cells) and ethidium homodimer-1 (red: Dead cells). (B) Immunofluorescence staining of the cell nucleus and cytoskeleton protein F-actin. (red: F-actin; blue: nucleus). (C) Finally, the cell viability in 3D constructs of IVZK peptide hydrogel for up to 3 days was tested.

thread deposition for the biomanufacturing of taller constructs. In this case, a continuous thread was formed during printing, suggesting that the interaction design of the nozzle connector avoids clogging. Finally, fine grid squares of 20 mm^2 were 3D-printed to evaluate shape fidelity and print resolution. Figure 4B shows fine threads formed in different layers. According to these results, the DNC shows promising potential to be used as a nozzle connector for peptide-based 3D bioprinting since it enables continuous hydrogel thread extrusion and forms 3D structures with good resolution. Further, in this paper, the integration of cells for 3D bioprinting with DNC is presented.

3.4. 3D cell culture and biocompatibility studies

To assess the cytocompatibility of cells growing in 3D constructs, HDFn was cultured within IVZK peptide hydrogels in 3D constructs. Cell viability, metabolic activity, and morphology assays were performed after 1 and 3 days following bioprinting. HDFn proliferation was evaluated through quantitation of ATP production in metabolically active cells. More live cells growing at a faster rate indicated better biocompatibility of the peptide hydrogels. As shown in Figure 5C, the HDFn viability was good with a percentage of total cells and a growth rate of about >80%. The cell viability was higher after day 3 than, it was on day 1, indicating successful growth and cell division, as confirmed by the ATP assay and live/dead assay results (Figure 5A and C). Cytoskeleton staining was performed to further evaluate the biocompatibility of HDFns in 3D IVZK hydrogels in terms of morphology and interaction of the cells with the material. As illustrated in Figure 5B, the morphology of the HDFn indicated the presence of F-actin filaments, which provide HDFn with mechanical support. Based on these results, we can conclude that HDFn favors the IVZK hydrogel materials, as evidenced by results of the cytotoxicity assays.

4. Conclusions

Beginning from an established point in the field of 3D bioprinting, we provide here a standardized fabrication method of nozzles for 3D bioprinting with hydrogel-based materials to improve reliability of generated data, which will steer the field in a much more standard direction, eventually making it more advanced. This method involves printing connectors with two inlets and an outlet, enabling the material to be mixed within. In addition, these connectors are designed to suit the standard medical needles in the market, allowing the connectors to be used universally, and making them optimal candidates for various mixing requirements and bioink viscosities. Moreover, IVZK peptide-based hydrogel materials possess highly promising properties, making them excellent choices for tissue engineering. The effectiveness of these peptide building blocks has been employed to be compatible with different cell lines such as HDFn. By evaluating the DNC with peptide-based bioinks, 3D constructs were printed with good print resolution, shape fidelity, and mechanical stability, confirming the performance of the DNC in continuous gelation. By taking advantage of the DNC's ability to combine two solutions and incorporate cells during extrusion, we were able to form 3D-bioprinted structures. The results suggest that HDFn is well suited for the IVZK hydrogel materials post-printing, as demonstrated by cytotoxicity tests, which confirms the biocompatibility of the DNC in 3D bioprinting. We propose the DNC as a solid alternative to the fabrication of handmade nozzles for 3D bioprinting by taking full advantage of rapid prototyping and ensuring standardization and reproducibility.

Acknowledgments

The authors would like to acknowledge Kowther Kahin for her dedicated work in nozzle design, which inspired this work, Noofa Hammad for her technical support on the robotic 3D bioprinter, and Aris Konstantinidis for his support in conducting the experiments.

Funding

This work was financially supported by King Abdullah University of Science and Technology (KAUST).

Conflicts of interest

There are no conflicts of interest to declare.

Author contributions

Conceptualization: Hamed I. Albalawi, Charlotte A. E. Hauser
Investigation: Hamed I. Albalawi, Zainab N. Khan, Ranim H. Rawas, Alexander U. Valle-Pérez, Sherin Abdelrahman
Methodology: Hamed I. Albalawi, Zainab N. Khan, Sherin Abdelrahman
Writing – original draft: Hamed I. Albalawi, Zainab N. Khan, Ranim H. Rawas, Alexander U. Valle-Pérez
Writing – review & editing: Zainab N. Khan, Hamed I. Albalawi, Charlotte A. E. Hauser

Ethics approval and consent to participate

Not applicable.

Consent for publication

Not applicable.

Availability of data

Data related to this work can be acquired by contacting the corresponding author with a reasonable justification.

References

1. Ngo TD, Kashani A, Imbalzano G, *et al.*, 2018, Additive manufacturing (3D printing): A review of materials, methods, applications and challenges. *Compos Part B Eng*, 143: 172–196.

   https://doi.org/10.1016/j.compositesb.2018.02.012

2. Ford S, Minshall T, 2019, Invited review article: Where and how 3D printing is used in teaching and education. *Addit Manuf*, 25: 131–150.

   https://doi.org/10.1016/j.addma.2018.10.028

3. Shahrubudin N, Lee TC, Ramlan R, 2019, An overview on 3D printing technology: Technological, materials, and applications. *Procedia Manuf*, 35: 1286–1296.

   https://doi.org/10.1016/j.promfg.2019.06.089

4. Gao W, Zhang Y, Ramanujan D, *et al.*, 2015, The status, challenges, and future of additive manufacturing in engineering. *Comput Aided Des*, 69: 65–89.

   https://doi.org/10.1016/j.cad.2015.04.001

5. Avila-Ramírez A, Valle-Pérez AU, Susapto HH, *et al.*, 2021, Ecologically friendly biofunctional ink for reconstruction of rigid living systems under wet conditions. *Int J Bioprint*, 7: 398.

   https://doi.org/10.18063/ijb.v7i4.398

6. Albalawi HI, Khan ZN, Valle-Pérez AU, *et al.*, 2021, Sustainable and eco-friendly coral restoration through 3D printing and fabrication. *ACS Sustain. Chem Eng*, 9: 12634–12645.

   https://doi.org/10.1021/acssuschemeng.1c04148

7. Wangpraseurt D, You S, Azam F, *et al.*, 2020, *et al.* Bionic 3D printed corals. *Nat Commun*, 11: 1748.

   https://doi.org/10.1038/s41467-020-15486-4

8. Melchels FP, Domingos MA, Klein TJ, *et al.*, 2012, Additive manufacturing of tissues and organs. *Prog Polym Sci*, 37: 1079–1104.

   https://doi.org/10.1016/j.progpolymsci.2011.11.007

9. Murphy SV, De Coppi P, Atala A, 2019, Opportunities and challenges of translational 3D bioprinting. *Nat Biomed Eng*, 4: 370–380.

   https://doi.org/10.1038/s41551-019-0471-7

10. Ng WL, Lee JM, Zhou M, *et al.*, 2020, Vat polymerization-based bioprinting-process, materials, applications and regulatory challenges. *Biofabrication*, 12: 022001.

    https://doi.org/10.1088/1758-5090/ab6034

11. Li W, Mille LS, Robledo JA, *et al.*, 2020, Recent advances in formulating and processing biomaterial inks for vat polymerization-based 3D printing. *Adv Healthc Mater*, 9: 2000156.

    https://doi.org/10.1002/adhm.202000156

12. Elomaa L, Gerbeth L, Almalla A, *et al.*, 2023, Bioactive photocrosslinkable resin solely based on refined decellularized small intestine submucosa for vat photopolymerization of *in vitro* tissue mimics. *Addit Manuf*, 64: 103439.

    https://doi.org/10.26434/chemrxiv-2022-f2hpc

13. Wang Y, Wang J, Ji Z, *et al.*, 2022, Application of bioprinting in ophthalmology. *Int J Bioprint*, 8: 552.

    https://doi.org/10.18063/ijb.v8i2.552

14. Ozbolat IT, Hospodiuk M, 2016, Current advances and future perspectives in extrusion-based bioprinting. *Biomaterials*, 76: 321–343.

    https://doi.org/10.1016/j.biomaterials.2015.10.076

15. Xing J, Luo X, Bermudez J, *et al.*, 2017, 3D Bioprinting of Scaffold Structure using Micro-Extrusion Technology. In: The Annual International Solid Freeform Fabrication Symposium, Austin.

    https://doi.org/10.26153/16943

16. De León EH, Valle-Pérez AU, Khan ZN, *et al.*, 2023, Intelligent and smart biomaterials for sustainable 3D printing applications. *Curr Opin Biomed Eng*, 26: 100450.

    https://doi.org/10.1016/j.cobme.2023.100450

17. Pradeep PV, Paul L, 2022, Review on novel biomaterials and innovative 3D printing techniques in biomedical applications. *Mater Today Proc.*, 58: 96–103.

    https://doi.org/10.1016/j.matpr.2022.01.072

18. Xu H, Su Y, Liao Z, *et al.*, 2022, Coaxial bioprinting vascular constructs: A review. *Eur Polym J*, 179: 111549.

    https://doi.org/10.1016/j.eurpolymj.2022.111549

19. Morgan FL, Moroni L, Baker MB, 2020, Dynamic bioinks to advance bioprinting. *Adv Healthc Mater*, 9: 1901798.

    https://doi.org/10.1002/adhm.201901798

20. Colosi C, Shin SR, Manoharan V, *et al.*, 2016, Microfluidic bioprinting of heterogeneous 3D tissue constructs using low-viscosity bioink. *Adv Mater*, 28: 677–684.

    https://doi.org/10.1002/adma.201503310

21. Khan ZN, Albalawi HI, Valle-Pérez AU, *et al.*, 2022, From 3D printed molds to bioprinted scaffolds: A hybrid material extrusion and vat polymerization bioprinting approach for soft matter constructs. *Mater Sci Addit Manuf*, 1: 7.

    https://doi.org/10.18063/msam.v1i1.7

22. Abdelrahman S, Alsanie WF, Khan ZN, *et al.*, 2022, A Parkinson's disease model composed of 3D bioprinted dopaminergic neurons within a biomimetic peptide scaffold. *Biofabrication*, 14: 044103.

    https://doi.org/10.1088/1758-5090/ac7eec

23. Skylar-Scott MA, Mueller J, Visser CW, *et al.*, 2019, Voxelated soft matter via multimaterial multinozzle 3D printing. *Nature*, 575: 330–335.

    https://doi.org/10.1038/s41586-019-1736-8

24. Alrashoudi AA, Albalawi HI, Aldoukhi AH, *et al.*, 2021, Fabrication of a lateral flow assay for rapid in-field detection of COVID-19 antibodies using additive manufacturing printing technologies. *Int J Bioprint*, 7: 399.

    https://doi.org/10.18063/ijb.v7i4.399

25. Khan Z, Kahin K, Rauf S, *et al.*, 2018, Optimization of a 3D bioprinting process using ultrashort peptide bioinks. *Int J Bioprint*, 5: 173.

    https://doi.org/10.18063/ijb.v5i1.173

26. Susapto HH, Alhattab D, Abdelrahman S, *et al.*, 2021, Ultrashort peptide bioinks support automated printing of large-scale constructs assuring long-term survival of printed tissue constructs. *Nano Lett*, 21: 2719–2729.

    https://doi.org/10.1021/acs.nanolett.0c04426

27. Kahin K, Khan Z, Albagami M, *et al.*, 2019, Development of a robotic 3D bioprinting and microfluidic pumping system for tissue and organ engineering. In: Gray BL, Becker H, editors. Microfluidics, BioMEMS, and Medical Microsystems XVII. 25 (SPIE, 2019).

    https://doi.org/10.1117/12.2507237

28. Khan Z, Kahin K, Hauser C, 2021, Time-dependent pulsing of microfluidic pumps to enhance 3D bioprinting of peptide bioinks. In: Gray BL, Becker H, editors. Microfluidics, BioMEMS, and Medical Microsystems XIX, 5 (SPIE, 2021).

    https://doi.org/10.1117/12.2578830

ACCSCIENCE PUBLISHING

Materials Science in Additive Manufacturing

ORIGINAL RESEARCH ARTICLE

Data imputation strategies for process optimization of laser powder bed fusion of Ti6Al4V using machine learning

Guo Dong Goh[1], **Xi Huang**[2], **Sheng Huang**[3], **Jia Li Janessa Thong**[3], **Jia Jun Seah**[3], **Wai Yee Yeong**[1,2,3*]

[1]Singapore Centre for 3D Printing, School of Mechanical and Aerospace Engineering, Nanyang Technological University, 50 Nanyang Avenue, Singapore 639798, Singapore

[2]HP-NTU Digital Manufacturing Corporate Lab, Nanyang Technological University, Singapore

[3]School of Mechanical and Aerospace Engineering, Nanyang Technological University, 50 Nanyang Avenue, Singapore 639798, Singapore

Abstract

A database linking process parameters and material properties for additive manufacturing enables the performance of the material to be determined based on the process parameters, which are useful in the design and fabrication stage of a product. The data, however, are often incomplete as each individual research work focused on certain process parameters and material properties due to the wide range of variables available. Imputation of missing data is thus required to complete the material library. In this work, we attempt to collate the data of Ti6Al4V, a popular alloy used in aerospace and biomedical industries, fabricated using powder bed fusion, or commonly known as selective laser melting (SLM). Various imputation techniques of missing data of the SLM Ti6Al4V dataset, such as the k-nearest neighbor (kNN), multivariate imputation by chained equations, and graph imputation neural network (GINN) are investigated in this article. It was observed that kNN performed better in imputing variables related to process parameters, whereas GINN performed better in variables related to material properties. To further improve the quality of imputation, a strategy to use the median of the imputed values obtained from the three models has resulted in significant improvement in terms of the relative mean square error. Self-organizing map was used to visualize the relationship among the process parameters and the material properties.

Keywords: Additive manufacturing; 3D printing; Selective laser melting; Powder bed fusion; Machine learning; Data analytics; Imputation

***Corresponding author:**
Wai Yee Yeong
(wyyeong@ntu.edu.sg)

Citation: Goh GD, Huang X, Huang S, *et al.*, 2023, Data imputation strategies for process optimization of laser powder bed fusion of Ti6Al4V using machine learning. *Mater Sci Add Manuf,* 2(1): 50.
https://doi.org/10.36922/msam.50

Received: February 1, 2023

Accepted: March 7, 2023

Published Online: March 22, 2023

Copyright: © 2023 Author(s). This is an Open Access article distributed under the terms of the Creative Commons Attribution License, permitting distribution, and reproduction in any medium, provided the original work is properly cited.

Publisher's Note: AccScience Publishing remains neutral with regard to jurisdictional claims in published maps and institutional affiliations.

1. Introduction

Ti6Al4V is one of the most popular titanium alloys given its excellent material properties, including high strength, low density, and high corrosion resistance, and is used in a wide variety of industries, such as in aerospace for aircraft components and in biomedical for implants[1]. Instead of using traditional manufacturing methods, selective laser melting (SLM) of Ti6Al4V allows for more complex parts to be created. It is an additive manufacturing technique, categorized as powder bed fusion (PBF), which involves melting layers of powder to form functional parts using computer-aided design (CAD) software which allows for freedom of design[2]. The SLM process is influenced by a set of process parameters; however, the number of these parameters is not clearly defined. The most influential ones are shown in Figure 1.

Typically for a material to be established as processable by SLM, parametric studies are needed to optimize the parameters to obtain defect-free and fully dense parts. These parameters may differ from one machine to another and between materials. The common parameters studied are the laser power, laser scanning speed, hatch spacing, and powder layer thickness. In particular, the laser power controls the amount of energy that irradiates the material while hatch spacing which defines the distance between two laser scans and it should provide enough overlap between adjacent scan tracks to bonds. Controlling the bed density in SLM can be challenging as it depends on several factors, such as the powder size and shape, the recoating process, and the initial bed leveling. The bed density can affect the heat transfer during the melting process and the resulting microstructure and mechanical properties of the printed parts.

One of the attractive points of SLM Ti6Al4V is that the material properties can be tuned by optimizing the SLM process parameters. For instance, by adjusting the scanning speed and hatching distance, Roudnicka *et al.* investigated various energy density values ranging from 40 to 400 J/mm^3[3]. Their results showed that porosity and mechanical properties can be significantly altered by adjusting the parameters, and suggested a processing range for achieving the highest relative density. Furthermore, it was found that modifying the energy density may cause microstructural changes, which can affect the mechanical properties of the final product. Different processing conditions will result in different microstructures and mechanical properties. For instance, the microstructure of SLM-produced bulk samples consists of needle-shaped α'-martensite phase[4]. Heat treatment promotes the formation of free α- and β-phases at grain boundaries. The samples possess high strength but low ductility prior to heat treatment. Heat treatment enhances their mechanical properties at both ambient and elevated temperatures. The previous studies have researched the process-properties relationships for SLM Ti6Al4V but have focused only on a few properties in their studies: physical properties such as relative density[5-9], or mechanical properties such as tensile strength and Young's modulus[10-14].

Other studies that have carried out parameter optimization or modeling for Ti6Al4V do not investigate the full range of process parameters and only involve a few material properties. Sun *et al.*[15] and Kuo *et al.*[6] have investigated the relationship between process parameters and the density of the SLM Ti6Al4V. The former varied laser power, scanning speed, layer thickness, hatch spacing, and scanning strategy to obtain specimens with maximum density, while the latter varied laser power, exposure duration, and point distance and reported the porosity of the printed specimen. Bartolomeu *et al.*[16] studied and modeled the effects of laser power, scan speed, and hatch spacing on the density, hardness, and shear strength of SLM Ti6Al4V. More research have been conducted to understand the fatigue behavior of SLM-fabricated Ti-6Al-4V[17], which may differ from the behaviors under static loading.

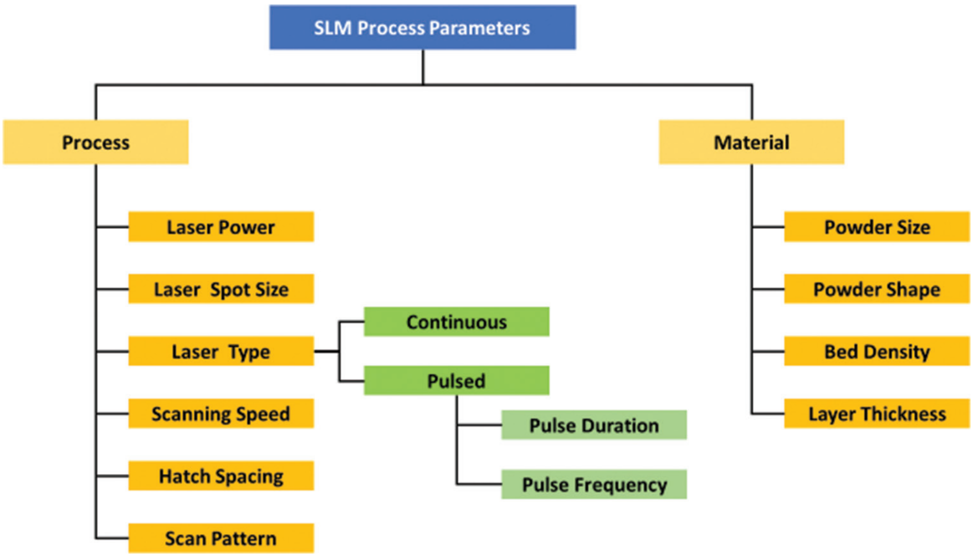

Figure 1. Influential parameters that affect the quality of the part fabricated by selective laser melting.

Machine learning in 3D printing is growing rapidly and has been used to perform process and design optimization, anomalies detection, etc.[18]. It relies heavily on the dataset to train a good machine learning model to have good prediction. Given the vast number of literature investigating the process parameters' effects on the different properties of SLM Ti6Al4V, there is potential in collating the data and using machine learning to perform data analytics on the dataset to determine the process-structure-properties relationship. There are missing values present in the collated SLM Ti6Al4V dataset as each property/parameter has been studied in isolation, but the quantity of data is insufficient for machine learning; therefore, imputation is required to bolster the data volume. Hence, the data from the literature are considered incomplete, and imputation of the missing data is required as a pre-processing step before subsequent analysis can be carried out.

Researchers have utilized various kinds of techniques to impute missing data in manufacturing processes. For instance, Steiner *et al.* aimed to develop real-time predictive models of two key strength properties of a wood composite manufacturing process using real-time process and destructive test data collected from a wood composite manufacturer[19]. However, sensor malfunction and data "send/retrieval" problems lead to null fields in the company's data warehouse, which resulted in information loss. To overcome this challenge, two missing data imputation methods, expectation-maximization (EM) algorithm and multiple imputation (MI) using Markov Chain Monte Carlo (MCMC) simulation, were used to impute the missing data. Predictive models based on the imputed datasets generated more precise prediction results than models of non-imputed datasets. In addition, Bayesian Additive Regression Tree (BART) produced the most precise prediction results among four predictive modeling methods. In another work, Wang *et al.* discuss the importance of data mining in intelligent manufacturing and introduce an energy monitoring platform for small- and medium-sized enterprises that records energy consumption data at various levels of granularity[20]. However, incomplete data can lead to an inaccurate portrayal of the system, so Wang *et al.* propose a novel orthogonal-least-square-based autoencoder to generate new samples for the imputation of missing values. The proposed approach outperforms alternative methods significantly for missing ratios >0.05 based on experimental results using real industrial datasets.

There are many data imputation strategies, from simple statistical methods such as mean imputation and regression imputation to more complex methods such as hot-deck imputation, which imputes the missing data by realistic scores that preserve the variable distribution[21]. Some widely-used imputation methods include: imputing using zero, mean, median, or mode; imputing using randomly selected value; and imputing using a model[22]. These techniques often impute a single and constant value for each variable without capturing or reflecting the relationship among the variables. This will likely result in an incorrect process-properties relationship.

Model-based imputation methods can be categorized into two types: those that make predictions for the missing values based on similar data points, and those that attempt to construct a global model to infer the missing data. The former includes algorithms such as k-nearest neighbors (kNN), while the latter encompasses deep learning neural networks.

The present study is focused on the investigation of the effect of different model-based imputation techniques on the process-structure relationship of the SLM Ti6Al4V dataset. The results of the imputation were evaluated to determine the best strategy for the dataset. This article will first present the methodology, followed by results and discussion about the different imputation methods, and finally the investigation of the imputed dataset.

2. Methodology

2.1. Imputation methods

2.1.1. k-Nearest neighbors (kNN) imputation

kNN imputation is one of the most common methods to impute missing values. It is used for both classification and regression problems[23]. The algorithm identifies k number of neighboring points using a distance metric and estimates the missing values using the values of these k neighboring observations[24].

The distance metric is generally Euclidean, and the function can be defined as

$$E\left(\vec{x},\vec{y}\right)=\sqrt{\sum_{i=1}^{m}(x_i-y_i)^2} \tag{I}$$

Where x_i and y_i are the point of interest and a case point from the dataset, and m is the number of input variables[25]. The process flow for the imputation is shown in Figure 2.

Since the kNN algorithm is non-parametric[23], there is no underlying assumption on the distribution of data, and hence, kNN is suitable for datasets with varied distributions.

Imputation was done using Scikit-learn's KNN Imputer class[26]. For calculation of the distance involving missing values, the coordinates of the missing value are ignored and the weights of the remaining coordinates

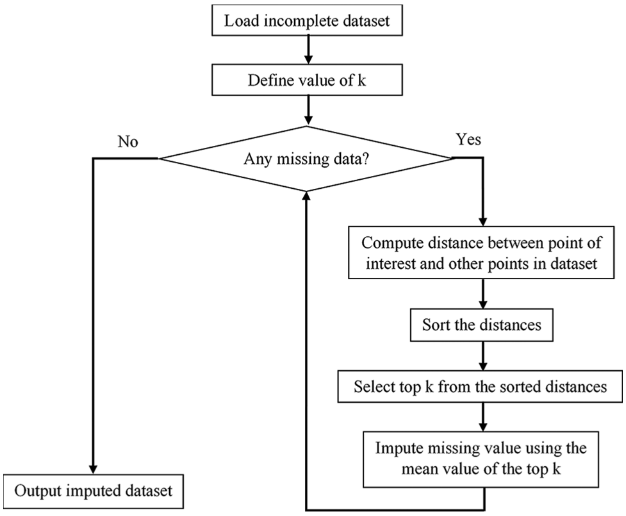

Figure 2. Process flow for k-nearest neighbor imputation.

are scaled-up[27]. The distance metric used to calculate the similarity between samples is the Euclidean distance. When calculating the distance involving missing values, the coordinates of the missing values are ignored. This means that when calculating the distance between two samples, only the coordinates where both samples have values are considered. The missing values are effectively treated as if they do not exist.

To account for the missing values, the weights of the remaining coordinates are scaled-up. This means that the distances between samples are adjusted to account for the missing values, so that samples that are similar in the remaining coordinates but have missing values in different locations are still considered similar. The scaling-up of weights is done by multiplying the weights of the remaining coordinates by a factor that is proportional to the number of non-missing coordinates in the samples being compared. Specifically, for each sample being compared, the weights of the remaining coordinates are divided by the proportion of non-missing coordinates in that sample. This means that the weights of the remaining coordinates are scaled-up by a factor equal to the reciprocal of the proportion of non-missing coordinates in the sample. This adjustment ensures that the distance metric takes into account the missing values in a meaningful way, without allowing the missing values to dominate the calculation. Each sample's missing values are imputed using the mean value from n_neighbors nearest neighbors, with n_neighbors = 5.

2.1.2. Multivariate imputation by chained equations

Multivariate imputation by chained equations (MICE)[28] is an imputation technique that iteratively imputes missing data for one variable modeled as a function of the other variables in a sequential fashion such that prior imputed values are used as part of the model in predicting subsequent variables. Hence, each variable can be modeled conforming to its distribution with continuous variables modeled using linear regression, while binary variables are modeled with logistic regression.

To carry out MICE, multiple copies of the dataset have to be created first. The following steps are then carried out on each copy of the dataset[29]:

(i) Missing values for each variable are imputed using non-missing values from the variable as a placeholder.
(ii) Set the imputed placeholders for one variable back to missing and model the selected variable as a function of the other variables. For each variable with missing values, the IterativeImputer class sets the imputed values for that variable to missing and models the selected variable as a function of the other variables using ExtraTreesRegressor. The model is trained on the complete cases, which are the cases where all variables are observed.
(iii) Using the fitted "ExtraTreesRegressor" model, predict, and impute missing values for the selected variable.
(iv) Repeat steps (ii) and (iii) for each variable in the dataset.
(v) The imputation cycle is repeated for 10 cycles, with the imputed values being updated at the end of each cycle.

The imputed copies of each dataset are then analyzed and the results combined using rules specific to the results[28], calculated using Rubin's Rules[30]. Rubin's Rule states that the estimated variance of the combined estimate is equal to the average of the within-imputation variance (the variability of the estimate within each imputed dataset) and the between-imputation variance (the variability of the estimates across the imputed datasets). To calculate the combined estimate, the point estimates from each imputed dataset are averaged, and the variance is calculated using Rubin's Rule. This approach accounts for the uncertainty due to missing data and provides estimates that are more accurate than those from the traditional complete case analysis.

Imputation was executed using Sckit-learn's IterativeImputer class, with the process flow as shown in Figure 3. Its implementation is similar to the R MICE package[28] but returns only one imputed dataset instead of multiple imputed datasets[31]. The estimator used for the sequential imputation was ExtraTreesRegressor, which builds an ensemble of regression trees, with default hyperparameters. Using ExtraTreesRegressor as the estimator for the IterativeImputer class, non-linear relationships between the variables in the dataset can be captured, which can result in improved imputations.

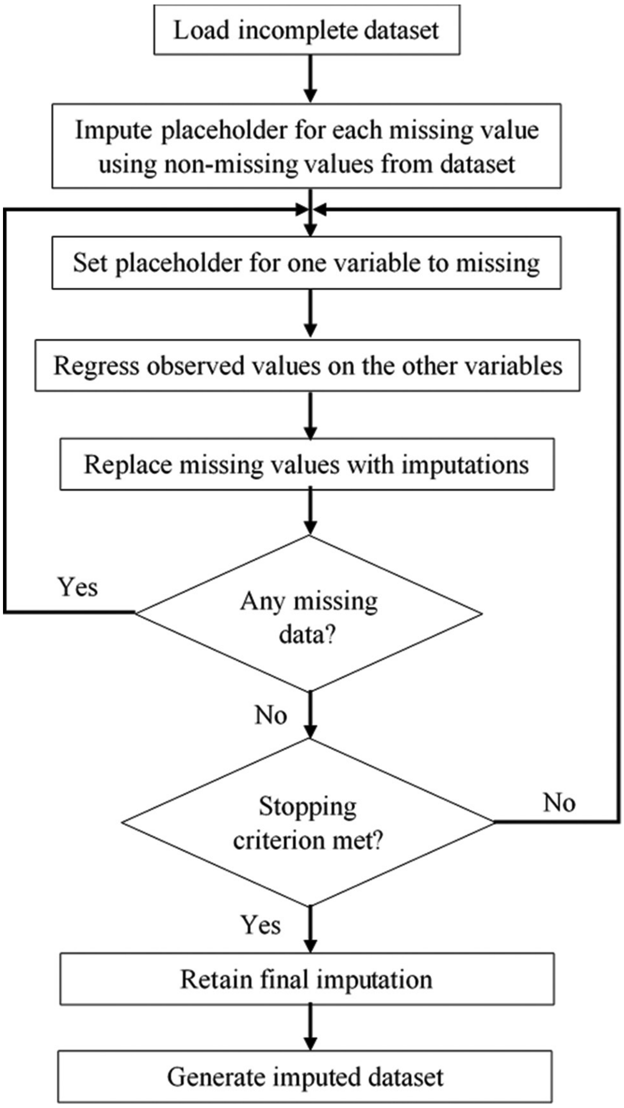

Figure 3. Process flow for graph imputation neural network imputation using IterativeImputer.

Since the Extra Trees algorithm is similar to Random Forest, which does not make any assumptions on the data[32], the distribution of the dataset to be imputed would not have a major impact on the imputation result.

2.1.3. Graph imputation neural network (GINN) imputation

GINN is a deep learning library that imputes missing data by first building a graph of similarities between complete values and then running an autoencoder with graph convolutions on top of that, with the schematics shown in Figure 4[33].

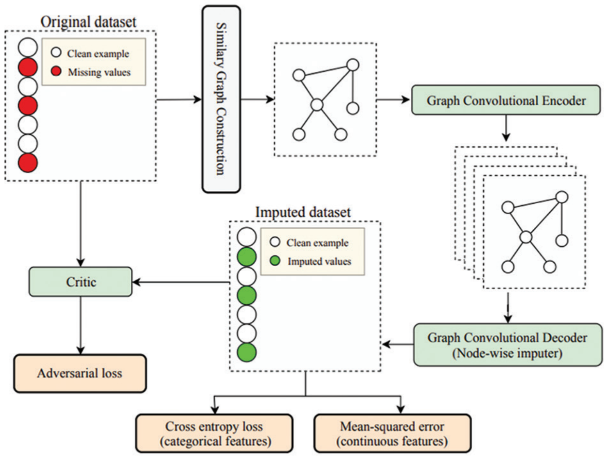

Figure 4. Schematics of graph imputation neural network imputation[27].

To develop the graph of similarities, each node of the graph is represented by a feature vector in the dataset, with Euclidean distance used to find the similarity between non-missing values[33]. Pruning is carried out twice by dropping all the connections below the 97.72th percentile, which was found to be a good value from experimental tests[33], for each row, leaving behind the most relevant nodes.

The graph convolution autoencoder used is defined as:

$$H=\mathrm{ReLU}\left(LX\Theta_1\right) \tag{II}$$

$$\hat{X}=\mathrm{Sigmoid}\left(LH\Theta_2\right) \tag{III}$$

Equation II is the encoder that takes the input X, with L as the Laplacian matrix related to the graph, and Θ_1 as a matrix of adjustable coefficients, and produces an encoded value H. Equation III is the decoder that provides a reconstructed imputed dataset $\hat{X}$ from the encoded H.

The graph convolution network is trained to minimize the loss function arising from errors in reconstruction as defined below:

$$L_A=\alpha \mathrm{MSE}\left(X,\hat{X}\right)+\left(1-\alpha\right)\mathrm{CE}(X,\hat{X}) \tag{IV}$$

Where MSE is the mean squared error for numerical variables, CE is the cross-entropy for categorical variables, and is an additional hyperparameter set as the ratio between numerical and categorical variables[33].

Adversarial training of the autoencoder is used in which a feedforward network is used as the critic to differentiate between imputed and non-imputed data, introducing an additional term to the loss function to include adversarial loss[33]. A more in-depth explanation of the GINN framework can be found in a previous work[33].

2.2. Cleaning of the dataset

Since there is a significant proportion of missing data in the dataset, initial data cleaning has to be carried out before imputation as the information is of limited use if there is insufficient data.

The proportion of missing data is first calculated for each variable, and variables with more than 92% missing data are dropped (Table 1).

In general, process parameter variables have fewer missing values as the print parameters are normally reported regardless of the type of mechanical tests being conducted, whereas material property variables have high number of missing values as not every study has reported the same material properties. The threshold number of 92% is determined having considered the importance of the variables and the pattern of missing data. It is understood that the accuracy and reliability of the imputations may be lower when a large proportion of the data is missing. In general, imputation methods tend to perform better when the amount of missing data is lower and may struggle to accurately impute large amounts of missing data. Therefore, in our case, we attempted alternative method such as multiple imputation followed by a median approach to improve the accuracy. Of the remaining variables, scanning strategy and microstructure are dropped as they are too varied and unable to be generalized. Duplicate rows in the remaining dataset are then dropped. 401 datapoints were retained.

There are 18 variables retained: energy density (J/mm^3), exposure duration (μs), hatch spacing (μm), laser focus (mm), laser power (W), laser spot (μm), laser type (0 for continuous wavelength [cw], 1 for pulsed wavelength [pw]), layer thickness (μm), point distance (μm), scan speed (mm/s), density (%), elongation (%), microhardness (HV), macrohardness (HV), ultimate tensile strength (MPa), yield strength (MPa), Young's modulus (GPa), and porosity (%). Only two variables, laser power and laser type, do not have any missing values.

Cells that have a range of data inputted as a string (e.g., "60 – 180") are replaced with the mean values. As the exact value was not given for the variable, the use of mean values for the range is the only option, although it will lead to some degree of uncertainty. Cells with standard deviations (e.g., "0.12 ± 0.03") are replaced to retain only the numeric values in front.

2.3. Visualizing relationships in imputed dataset

After obtaining the imputed dataset using the median values obtained from the 3 algorithms, the process-properties linkages for SLM Ti64 can be obtained using data-mining through a self-organizing map (SOM). A SOM is an unsupervised machine learning model developed by Kohonen that reduces the dimensionality of an input space while maintaining its underlying structure[34]. This is especially useful to visualize large quantities of high dimensional data and model the relationship between them in a low, two-dimensional map, helping to advance the understanding of process-property relationships for materials.

The implementation of the SOM is from a Python package Tfprop_sompy, developed by Kikugawa and Nishimura, based on an open-source package SOMPY[35]. The training data were normalized by $x_{ij} = \frac{x_{ij} - \mu_j}{\sigma_j}$ where x_{ij} is the i-th row of the j-th variable in the data, and μ_j and σ_j are the mean and standard deviations of the j-th variable, respectively. The size of the map was set to be 50 × 50 with the weights initialized using principal component analysis. Different sizes of the SOM were attempted and a map size of 100 × 100 was chosen such that each node of the map corresponds to at most one point of data in the dataset[36].

3. Results and discussion

3.1. Validation of the imputation models

Validation of the imputed values can be done through graphical plots that show the distribution of data, as well as numerical displays such as summary statistics of the imputed dataset[37].

Graphical evaluation of the imputed datasets is performed through data visualization using three plots: Boxplot, kernel density plot with histogram, and cumulative distribution plot. By comparing the statistical visualization plots, one can have an idea of the distribution of the imputed values and determine if they fall within expected boundaries.

Figure 5 shows the visualization plots for the energy density of the original dataset (observed) against the complete imputed dataset (imputed) for kNN imputations. The imputed values have close distributions to the original dataset and can be said to have reasonable values.

The three visualization plots for all the incomplete variables are plotted for each of the imputed datasets, and the imputed values for energy density, hatch spacing, laser spot, layer thickness, scan speed, elongation, microhardness, macrohardness, yield strength, and porosity for all three imputed datasets are found to be adequately close to the distribution of the original dataset (Figures S1–S3). However, the distributions for exposure duration, laser focus, point distance, and Young's modulus deviate from the original distribution to varying degrees for the different imputation techniques, with MICE (Figure 6) showing the greatest deviation followed by GINN (Figure 7) and then kNN (Figure 8).

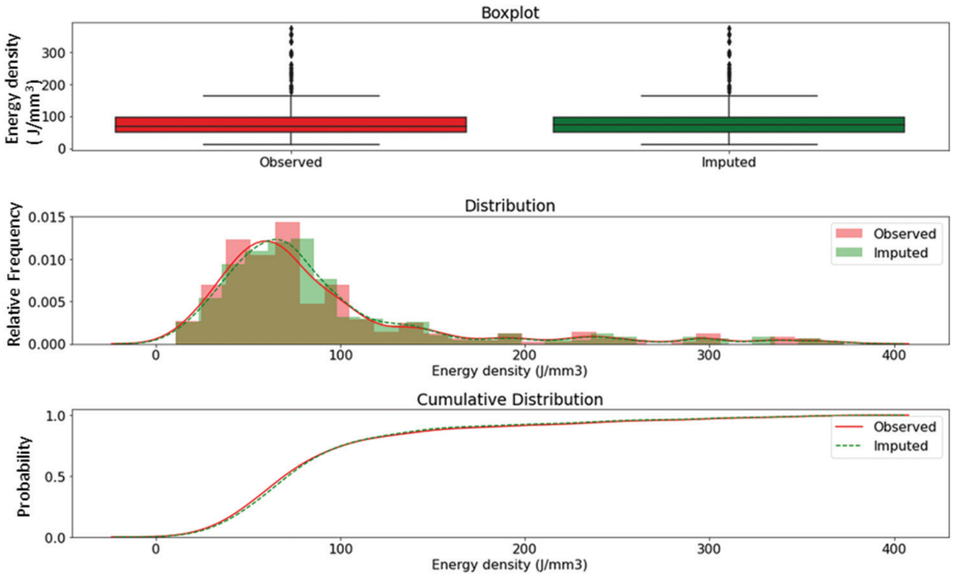

Figure 5. Graphs comparing the distributions of the observed (red) and imputed (green) energy density values. Top: Boxplot of the observed and imputed energy density values. Middle: Kernel density plot (line) with histogram (bars) of the observed and imputed energy density values. Bottom: Cumulative distribution plot of the observed and imputed energy density values.

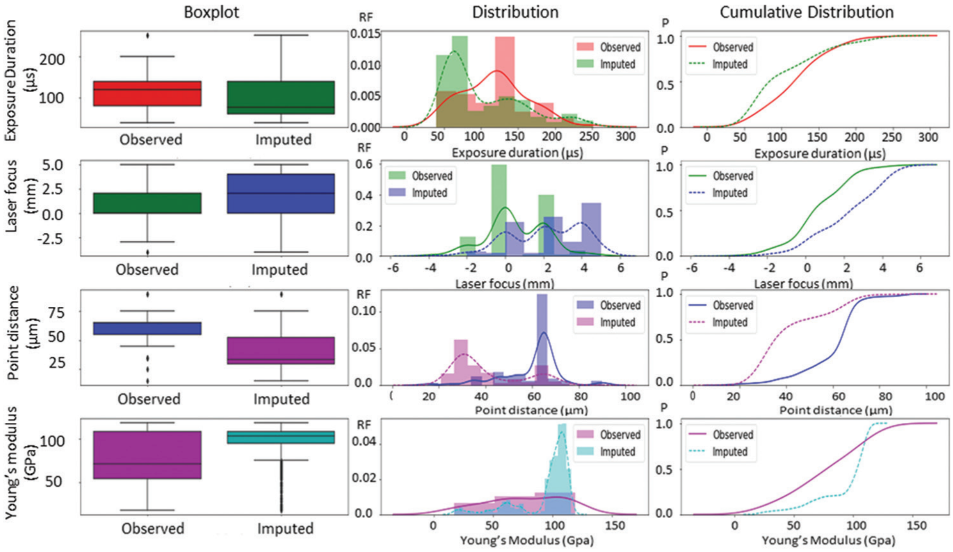

Figure 6. Graphs comparing the distributions of the observed and imputed values of exposure duration, laser focus, point distance, and Young's modulus for multivariate imputation by chained equations-imputed dataset, where RF is relative frequency and P is probability.

The variables exposure duration and point distance are only applicable to pulse wave laser for SLM. Since the dataset contains data from both pulse wave laser and continuous wave laser, the imputed values for these two variables would be for continuous wave laser parameter sets, which would not be relevant.

According to the literature[38], laser focus is a parameter that determines the laser spot size. However, the original literature that provided the values for laser focus did not state the laser spot size, and since there are several different ways to define the beam diameter[39], it is difficult to obtain the correct relationship between laser focus and laser spot for each observed value of laser focus. This could be a contributing factor, together with the limited data for laser focus, which led to the imputed values deviating from the original distribution.

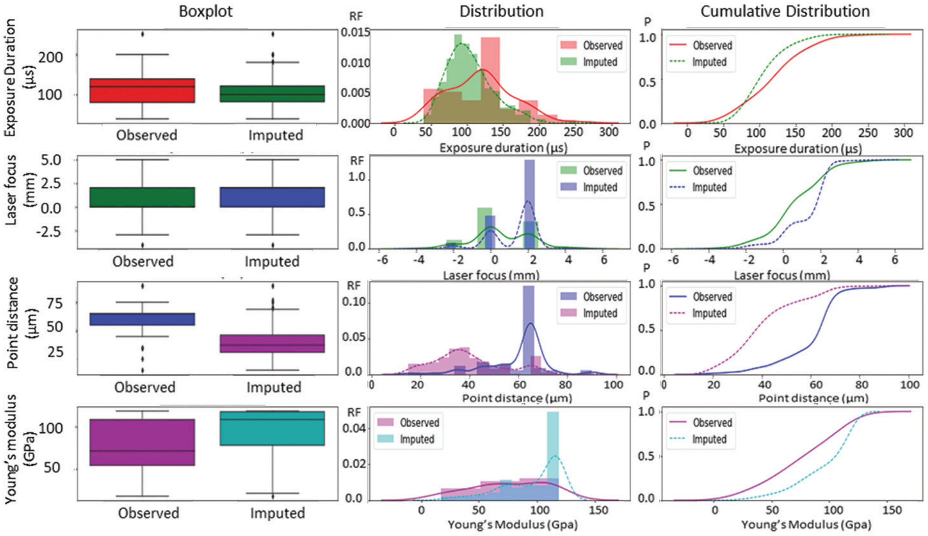

Figure 7. Graphs comparing the distributions of the observed and imputed values of exposure duration, laser focus, point distance, and Young's modulus for graph imputation neural network-imputed dataset, where RF is relative frequency and P is probability.

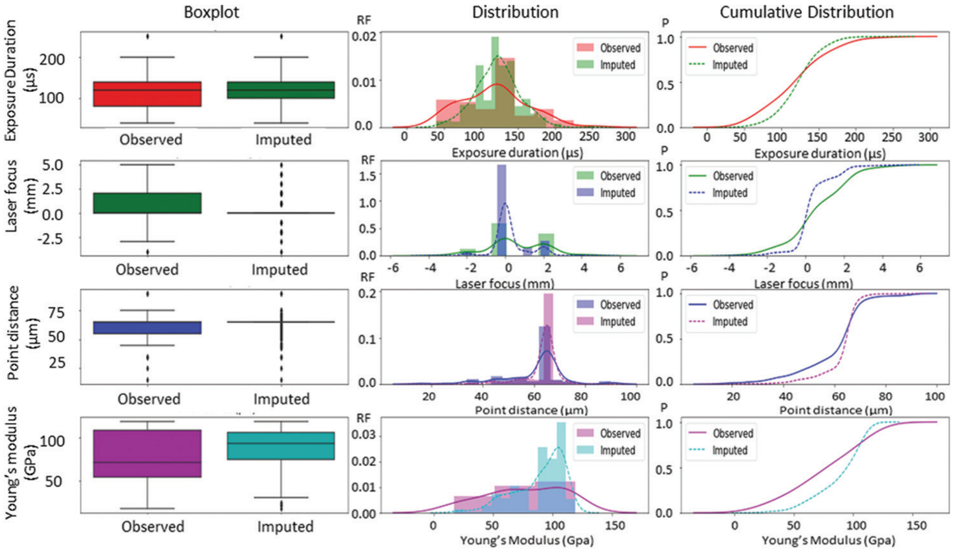

Figure 8. Graphs comparing the distributions of the observed and imputed values of exposure duration, laser focus, point distance, and Young's modulus for the k-nearest neighbor-imputed dataset, where RF is relative frequency and P is probability.

For the imputed values of Young's modulus, there appears to be a peak at around 120 GPa for all three imputed datasets. On further investigation of the imputed datasets, it was found that most of the imputed values close to 120 GPa correspond to sets of observed data that have similar values for the other parameters. Hence, it is not unreasonable for the range of values for the imputed Young's modulus values to be around 120 GPa. There is also limited observed data for Young's modulus (92% missing values), which could have contributed to the limited range of values imputed. To improve the distribution, more varied data with a larger range of Young's modulus values have to be obtained to allow the imputation algorithms to be more robust.

The complete visualization plots for all incomplete variables for all three imputed datasets can be found in the Supplementary File.

Occasionally, imputing more than 50% of the values may be required depending on the specific dataset and research question. In this case, it is necessary to impute a large proportion of missing data to maintain a sufficient sample size and to include important variables in the analysis. However, imputing a high proportion of missing data can also increase the risk of bias and lead to inaccurate results. Therefore, it is important to carefully evaluate the validity of imputed data through various methods such as statistical summaries and comparison with observed data.

Statistical summaries can be used to validate imputed values, and Table 2 shows the compiled observed and imputed datasets. In the kNN-imputed dataset, the minimum and maximum values for all imputed variables remained unchanged from the original values. The mean and standard deviation of observed and imputed energy density values were similar (89.20 vs. 89.07 J/mm^3, and 68.05 vs. 65.14 J/mm^3, respectively). However, variables such as laser spot showed disparities in mean (125.56 vs. 106.03 μm) and standard deviation (133.86 vs. 97.57 μm), possibly due to differences in the proportion of missing data for each variable, with energy density having 364 observed values out of a total of 401, compared to only 194 observed values for laser spot.

Similarly, for the MICE-imputed and GINN-imputed datasets, the minimum and maximum values for all imputed variables did not change. There were also disparities in mean and standard deviations for variables laser focus and laser spot, possibly due to a large proportion of missing data, as discussed above. For the MICE-imputed dataset, the standard deviations of ultimate tensile strength and yield strength do differ (147.47 vs. 218.33 GPa, and 189.93 vs. 269.83 GPa, respectively) but given the proportion of missing data for these two variables, the imputed values may be reasonable. Thus, individual values of the imputed dataset have to be checked to ascertain if the imputations are sensible.

Table 1. Percentage of missing values for each variable

Variables	Missingness (%)
Laser power (W)	0.00
Laser type (0 for cw, 1 for pw)	0.00
Layer thickness (μm)	0.25
Hatch spacing (μm)	5.93
Energy density (J/mm^3)	9.14
Scan speed (mm/s)	14.81
Density (%)	43.46
Laser spot (μm)	51.60
Porosity (%)	69.14
Laser focus (mm)	73.09
EL (%)	79.51
Ultimate tensile strength (MPa)	79.51
Exposure duration (μs)	80.49
Point distance (μm)	81.98
Yield strength (MPa)	82.22
Macrohardness (HV)	88.15
Microhardness (HV)	90.12
Young's modulus (GPa)	92.35

Other than using the graphical and statistical methods to evaluate the imputed datasets, imputed values are also manually checked for any illogical values for the material properties: density and porosity values should add up to 100%, and the microhardness should be higher than the macrohardness[40]. Imputed values for process parameters should also fall within the processing window.

3.2. Comparison of imputation models

Comparing the distribution graphs, all three imputed datasets have relatively close distributions to the original dataset for the process parameters, as well as density and porosity variables. The discriminating features are the remaining variables, namely, elongation, microhardness, microhardness, ultimate tensile strength, yield strength, and Young's modulus. The model performs better for the processing parameters as they are deterministic and depend on fewer external factors. In addition, more datapoints are available for the processing parameters as they are reported in most of the studies. The material properties have a higher deviation because they have fewer datapoints as not every study focused on every aspect of material properties. There are also other factors such as different scan strategies, microstructures, and mechanical test conditions that are not captured in the dataset, leading to poorer imputation accuracy. As seen from the cumulative distribution plots (Figure 9) and distribution plots (Figure 10) of the three imputed datasets, GINN imputation results in the closest distribution to the original dataset.

The distribution of the kNN-imputed dataset has an acceptable deviation from the original distribution. However, an examination of the imputed dataset found that many imputed values for material properties are identical, even with different process parameters. The kNN algorithm did not manage to adequately capture the relationship between process parameters and material properties. Even so, it did successfully model the relationship between density and porosity, with all imputed values for these two variables adding up to 100%. There were also only a few instances where microhardness was lower than macrohardness.

Mean square error of the distributions is calculated and tabulated in Table 3. It was found that kNN performed

Table 2. Statistical summaries of observed and imputed datasets for kNN, MICE, and GINN for variables with missing values

Features	Observed					kNN imputation					MICE imputation					GINN imputation				
	N	Mean	SD	Min	Max	N	Mean	SD	Min	Max	N	Mean	SD	Min	Max	N	Mean	SD	Min	Max
Energy density (J/mm^3)	364	89.20	68.05	11	373	401	89.07	65.14	11	373	401	92.93	67.56	11	373	401	85.32	67.23	11	373
Exposure duration (µs)	78	117.73	43.88	40	251	401	122.09	29.34	40	251	401	102.90	50.74	40	251	401	104.18	31.88	40	251
Hatch spacing (µm)	377	106.42	56.43	35	460	401	114.32	73.92	35	460	401	115.82	74.70	35	460	401	114.57	72.23	35	460
Laser focus (mm)	107	0.57	1.56	−4	5	401	0.28	0.96	−4	5	401	1.86	1.70	−4	5	401	1.30	1.22	-4	5
Laser spot (µm)	194	125.56	133.86	34	730	401	106.03	97.57	34	730	401	108.81	96.52	34	730	401	109.81	100.86	34	730
Layer thickness (µm)	400	45.30	34.89	20	200	401	45.27	34.85	20	200	401	45.32	34.85	20	200	401	45.25	34.86	20	200
Point distance (µm)	72	60.01	12.51	15	90	401	62.89	7.22	15	90	401	41.30	15.82	15	90	401	39.72	14.60	15	90
Scan speed (mm/s)	342	613.23	531.09	25	7000	401	638.93	514.52	25	7000	401	618.34	520.05	25	7000	401	580.02	501.83	25	7000
Density (%)	350	96.67	6.92	35	100	401	96.94	6.51	35	100	401	96.67	6.46	35	100	401	96.99	6.53	35	100
Elongation (%)	82	6.31	3.05	0	14.5	401	6.54	1.84	0	14.5	401	5.84	2.53	0	14.5	401	6.76	2.43	0	14.5
Microhardness (HV)	40	385.05	46.64	225	479	401	393.97	27.84	225	479	401	372.65	36.34	225	479	401	389.81	38.65	225	479
Macrohardness (HV)	47	366.31	26.84	262	403.5	401	372.27	12.76	262	403.5	401	356.86	28.90	262	403.5	401	358.81	34.32	262	403.5
Ultimate tensile strength (MPa)	82	1175.21	147.47	420	1407	401	1168.89	107.53	420	1407	401	1073.71	218.33	420	1407	401	1167.01	140.24	420	1407
Yield strength (MPa)	71	1049.56	189.93	0	1333	401	1040.13	125.32	0	1333	401	916.49	269.83	0	1333	401	1078.48	154.94	0	1333
Young's modulus (GPa)	31	75.64	32.28	17.12	119	401	89.08	20.84	17.12	119	401	95.03	22.62	17.12	119	401	96.59	25.66	17.12	119
Porosity (%)	350	3.33	6.92	0	65	401	3.06	6.51	0	65	401	3.34	6.46	0	65	401	3.02	6.53	0	65

N is the number of datapoints; maximum number of datapoints is 401 in this study; number of available datapoints for observed dataset is always smaller than 401 and may not be the same.
kNN: k-nearest neighbor, GINN: Graph imputation neural network, MICE: Multivariate imputation by chained equations

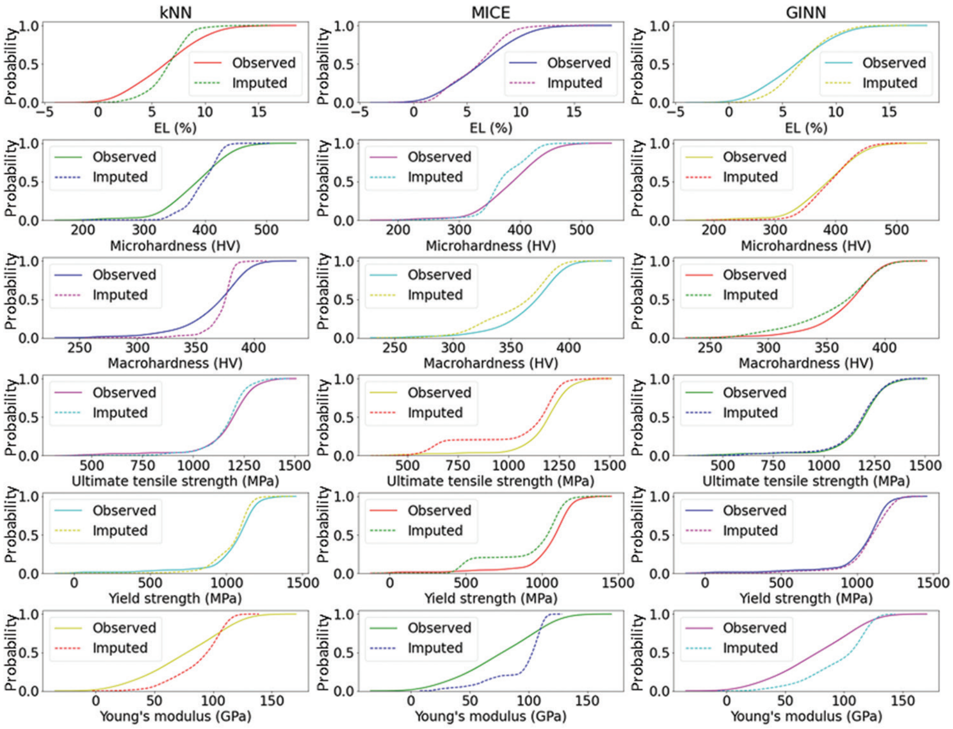

Figure 9. Cumulative distribution plots for k-nearest neighbor-imputed (left), multivariate imputation by chained equations-imputed (middle), and graph imputation neural network-imputed (right) datasets for selected incomplete variables.

the best for six variables, including exposure duration, hatch spacing, laser focus, layer thickness, point distance, and Young's modulus. GINN gave the best imputation for seven variables, including laser spot, density, elongation, microhardness, macrohardness, ultimate tensile strength, and yield strength. MICE only outperformed kNN and GINN in two variables, that is, scan speed and porosity. It is interesting to note that kNN performed better in imputing variables related to process parameters, whereas GINN performed better in variables related to material properties.

For the MICE-imputed dataset, the imputed values were much more varied, and the imputations showed a stronger relationship between the process parameters and material properties than the kNN-imputed dataset. While MICE performed better than kNN in that aspect, there were more instances where microhardness values were lower than macrohardness values (137 for MICE versus 73 for kNN). The sum of the imputed density and porosity values also do not add up to 100%, instead ranging from 99.92% to 100.12%.

The GINN algorithm can be said to have performed the best with the closest distribution to the original dataset and the most varied imputed values, although with 109 instances of lower values of microhardness compared to macrohardness, translating to 73% of the data showing the correct relationship. Most of the sums of imputed density and porosity values add up to 100% when rounded to 2 decimal places.

The performances of the models were validated by comparing the values obtained from the models with the actual values calculated from a known relationship. The laser scan speed is known to be related with other parameters by the equation below.

$$V = \frac{P}{Ehl} \tag{V}$$

where V is the laser scan speed, P is the laser power, E is the volumetric energy density, h is the hatch spacing, and l is the layer thickness. There are 48 datarows in the dataset that contains missing data for the laser scan speed while other parameters such as laser power, energy density, hatch spacing and layer thickness are available. These datarows can be used to validate the performance of the imputation models by comparing the imputed laser scan speed with the calculated laser scan speed using the known relationship as shown in Equation V. Figure 11 shows the performance of the models. It is found that the KNN model tends to overpredict the laser scan speed, while the GINN model tends to underestimate the laser scan speed. The MICE model is able to predict the laser scan speed correctly in

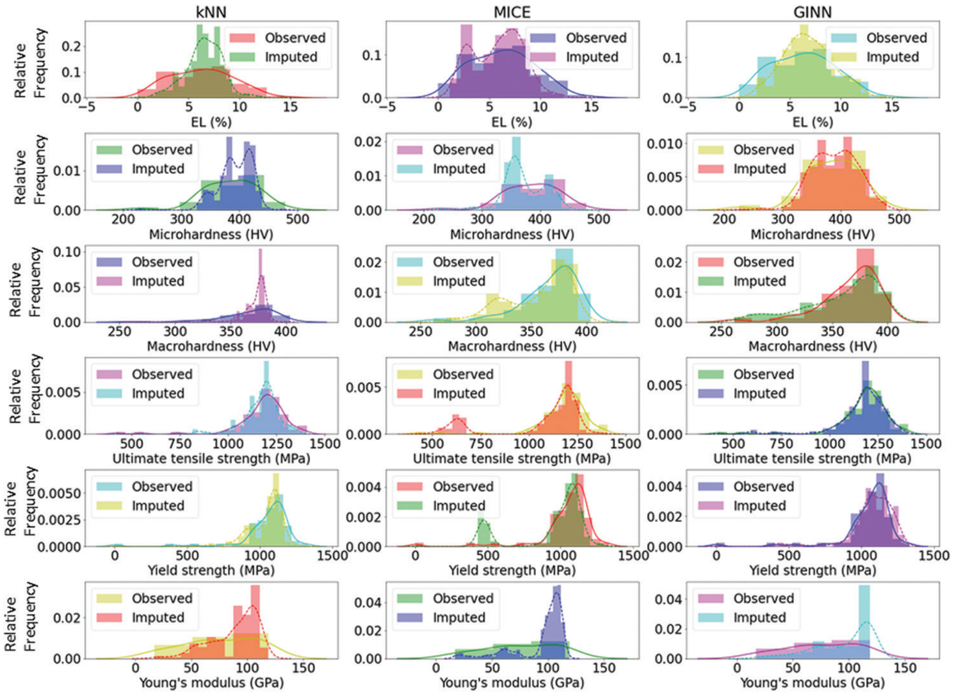

Figure 10. Distribution plots for k-nearest neighbor-imputed (left), multivariate imputation by chained equations-imputed (middle), and graph imputation neural network-imputed (right) datasets for selected incomplete variables.

Table 3. Comparison of the mean square error of the distribution for each variable

Features	kNN	MICE	GINN
Energy density (J/mm³)	3.06E-07	1.71E-07[a]	3.11E-07
Exposure duration (µs)	1.64E-05[a]	4.46E-05	3.23E-05
Hatch spacing (µm)	1.32E-07[a]	7.72E-08	6.77E-08
Laser focus (mm)	2.90E-02[a]	3.03E-02	4.47E-02
Laser spot (µm)	1.19E-06	8.50E-07	2.97E-07[a]
Layer thickness (µm)	1.42E-09[a]	2.88E-09	4.26E-09
Point distance (µm)	1.23E-04[a]	8.56E-04	1.03E-03
Scan speed (mm/s)	1.11E-09	3.75E-10[a]	7.04E-10
Density (%)	1.77E-03	2.27E-03	1.82E-03[a]
Elongation (%)	3.87E-03	2.29E-03	1.81E-03[a]
Microhardness (HV)	1.50E-05	1.51E-05	4.81E-06[a]
Macrohardness (HV)	1.69E-04	2.99E-05	2.36E-05[a]
Ultimate tensile strength (MPa)	2.08E-07	4.52E-07	4.86E-08[a]
Yield strength (MPa)	9.12E-07	7.23E-07	2.30E-07[a]
Young's modulus (GPa)	2.24E-04[a]	2.26E-04	2.97E-04
Porosity (%)	6.01E-05	2.99E-05[a]	4.71E-05

[a]Lowest MSE among the three models. kNN: k-nearest neighbor, GINN: Graph imputation neural network, MICE: Multivariate imputation by chained equations

general, but the presence of outliers causes the relative mean square error (RMSE) (1.36) to be higher compared to the KNN (0.29) and GINN (0.16). GINN performs the best in terms of the RMSE.

To further validate the results, a composite parameter (energy density × hatch spacing) was used to evaluate the models. There are 19 datarows in the dataset that contains missing data for the energy density and hatch spacing, while other parameters of the energy density equation such as laser power, laser scan speed and layer thickness are available. Figure 12 shows the performance of the models. It is found that the MICE model tends to overpredict the composite parameter, while the GINN model tends to underestimate the composite parameter. The GINN model has a lowest RMSE (0.33) for the composite parameter, whereas MICE model has a higher RMSE (3.87) for the composite parameter.

To get the best out of the three models, further processing steps were taken. For each missing datapoint, the median of the imputed values obtained from the three models was taken as the final imputed value. This enhances the statistical confidence of the imputed value and reduces the chances of getting the outliers especially when dealing with small dataset. It resulted in a remarkable RMSE of 0.026, which is significantly lower than that of all three individual models (Figure 13). Nonetheless, it is believed that the models can be further improved with increased number of datapoints.

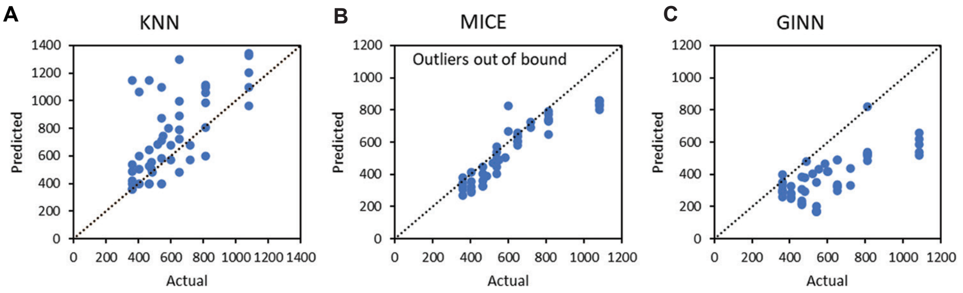

Figure 11. Comparison of the actual and predicted laser scan speed for various models. (A) k-nearest neighbor; (B) multivariate imputation by chained equations; (C) graph imputation neural network. See Supplementary File for the out-of-bound outliers.

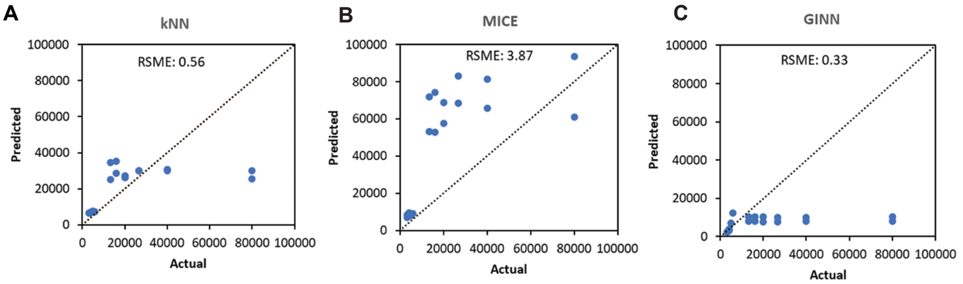

Figure 12. Comparison of the actual and predicted composite parameter (energy density × hatch spacing) for various models. (A) k-nearest neighbor; (B) multivariate imputation by chained equations; (C) graph imputation neural network.

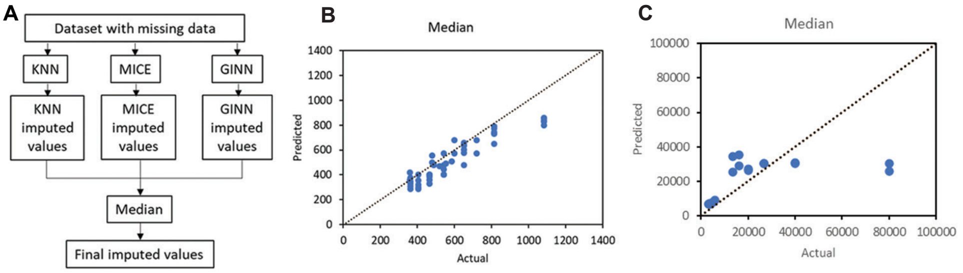

Figure 13. Strategy to improve quality of imputed dataset. (A) Median of the imputed values obtained from the k-nearest neighbor, multivariate imputation by chained equations, and graph imputation neural network. (B) The actual and predicted laser scan speed for the median of the imputed values. (C) The actual and composite parameter (energy density × hatch spacing) for the median of the imputed values.

The accuracy of the imputed results depends on several factors such as the quality of the original data, the imputation method used, and the amount and pattern of missing data. In this context, the imputation method used (GINN, MICE, and kNN) was found to be effective in reducing the overall RMSE and improving the accuracy of the imputed data. The final imputation strategy, which involved taking the median of the imputed values from the three models, further improved the accuracy of the imputed data.

While the results obtained in this study are promising, it is important to note that the suitability of the imputed data for wider implementation or industrial use depends on the specific context and requirements of the application. For example, if the imputed data are to be used for critical decision-making or safety-critical applications, a more rigorous validation process may be necessary to ensure the accuracy and reliability of the imputed data.

Data imputation is a crucial step in data analysis and modeling, especially when dealing with missing data. Imputation methods such as MICE and kNN can help to recover missing data and enable more robust and accurate data analysis. In addition, imputation can also help to reduce bias and increase the representativeness of the data, which can improve the quality of the insights and conclusions derived from the data.

The value of this work lies in its application of multiple imputation methods to a real-world dataset in the context

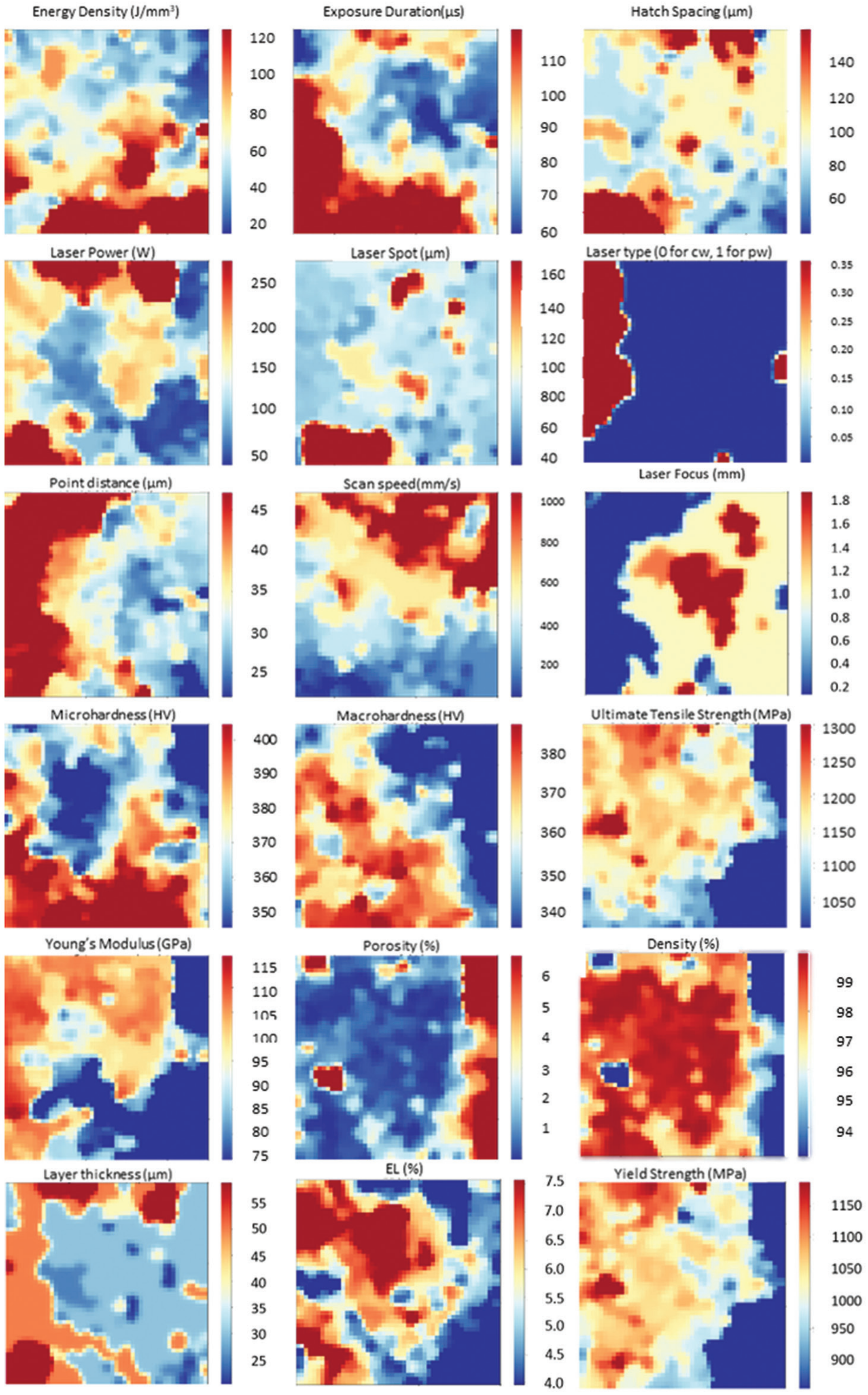

Figure 14. Heatmaps produced by self-organizing map for all 14 variables: 7 process parameters and 7 material properties. Red regions correspond to high values and blue regions correspond to low values.

of SLM. The study provides insights into the effectiveness of different imputation methods and highlights the importance of careful data cleaning and validation in ensuring the accuracy and reliability of the imputed data. The study also demonstrates a practical approach to combining multiple imputation models to enhance the statistical confidence of the imputed data, which can be useful in other domains as well.

4. Visualizing relationships between variables in imputed dataset

Heatmaps for each variable was used to visualize the SOM trained, produced by linking each variable value to a node on the map grid (Figure 14). The relationships between the variables can be determined based on visual analysis, by comparing the locations of the red and blue regions that correspond to high and low values respectively. Based on the heatmaps, the following observations are made from the imputed dataset, some of which are well established relationship:

(i) Porosity is inversely related to Young's modulus and yield strength.
(ii) Scan speed is inversely related to microhardness and macrohardness.
(iii) Exposure duration is directly related to macrohardness.
(iv) Ultimate tensile strength, yield strength, and elongation are directly related.
(v) Energy density and scan speed are inversely related.
(vi) Laser power and Young's modulus are slightly directly related.

These relations provide insight into the process-property relationships in SLM Ti64 and can help users determine the process parameter window to obtain certain desired material properties. For example, to obtain a specimen with higher hardness, a lower scan speed, higher energy density and longer exposure duration should be used. A higher laser power is also likely to result in higher Young's modulus. The inverse relationship between the energy density and scan speed are found to be consistent with the energy density equation.

The inverse relationship between scan speed and microhardness in SLM Ti64 can be explained by several factors. First, high scan speeds can also lead to incomplete melting, resulting in the formation of unmelted or partially melted particles, which can act as a source of defects and lower the microhardness[41]. Second, there could be a change in microstructure of the printed Ti64 from a coarser equiaxed grains to a finer columnar grains as the scan speed increases. When the scanning speed is slow, the laser's slower movement increases both the energy input and stability of the molten pool. The elevated temperature in the molten pool creates adequate energy and nuclei for the epitaxial growth of columnar grains in the building direction. Wang *et al.* observed the coarsening of acicular structures in the samples produced at a speed of 250 mm/s compared to those produced at a speed of 1150 mm/s, and the shape was similar to that of heat-treated samples, as documented by Vilaro *et al.*[11,42]. As the scan speed increased to 1150 mm/s, the quantity of β-phase nanoparticles reduced, and only few white particles were dispersed across the fine acicular α (α′) grain boundaries.

There are several factors that can contribute to the relationship between laser power and Young's modulus in SLM of metals. One possible explanation is related to the changes in microstructure and grain size that can occur as a result of varying laser power levels. High laser power can lead to rapid melting and solidification of the material, resulting in smaller grain sizes and higher dislocation densities, which can contribute to an increase in Young's modulus.

It is noted from the heatmap that there is a slight correlation between laser power and Young's modulus. However, the effect of laser power on the Young's modulus in SLM Ti64 is not straightforward and depends on several factors. At low laser powers, the material experiences less thermal input and solidifies with a finer microstructure, resulting in a higher Young's modulus due to the increased strength of the material. However, as the laser power increases, the material is heated to a higher temperature, resulting in coarser microstructures due to increased grain growth and leading to a decrease in the Young's modulus. Furthermore, excessive laser power can result in porosity and defects in the material, which can significantly reduce the Young's modulus[10]. Therefore, the laser power should be optimized to achieve the desired microstructure and avoid porosity formation to ensure that the built parts have the required Young's modulus for their intended application.

Overall, it is important to consider the complex interplay between multiple process parameters and material characteristics that can affect mechanical properties in SLM. This also highlights the importance of including scan strategies and microstructures in the dataset for better generalization of the process-structure-properties relationship of SLM Ti64.

5. Conclusions

In this study, three model-based imputation techniques, kNN, MICE, and GINN imputations, were used to impute missing values in the Ti6Al4V dataset, which contained various process parameters and material properties obtained from multiple sources available in the literature. The results of the imputations were evaluated using graphical checks and statistical summaries to compare the imputed data with the original distribution before imputation. Among the three techniques, GINN imputation gave the closest distribution to the original dataset and was the most accurate method, achieving the lowest RMSE. A median approach was used by taking the median of the imputed values from the three models. It was found that the median approach further improved the imputation accuracy by achieving RMSE of 0.026.

Data mining of the imputed SLM Ti64 dataset using SOM identified correlations between the process parameters and material properties. These correlations can be utilized to help users identify suitable process parameters for specimens with certain desired properties. While the material properties of monotonic yield strength and elongation at break are important, there are many other properties that could be of interest in the field of additive manufacturing. For example, fatigue strength, fracture toughness, creep resistance, and corrosion resistance are all important material properties that could be explored. In addition, exploring the relationship between process parameters and microstructure, such as grain size, could also provide valuable insights for optimizing the manufacturing process. The presented approach can also be applied to other databases to obtain new knowledge from the database.

However, a major limitation of the imputation methods is that a large proportion of missing data would lead to more inaccurate data imputation, and more manual checking of individual imputed values to ensure validity would be required. Imputation is not always appropriate and may introduce bias or lead to incorrect conclusions if the missing data is non-random or missing not at random. There is no specific quantitative threshold or limit to how much imputation can be performed before the results become meaningless. The validity of imputed data depends on the accuracy of the imputation models, the quality of the original data, and the degree and pattern of missingness.

In summary, imputation using the median approach was found to be the most accurate method for imputing missing data in the Ti6Al4V dataset, and the data mining approach using SOM identified correlations between process parameters and material properties. However, the study also highlights the need for more standardized testing and reporting, and the limitations of data imputation methods when dealing with a large proportion of missing data.

Acknowledgments

None.

Funding

This research is supported by the National Research Foundation, Prime Minister's Office, Singapore under its Medium-Sized Centre funding scheme.

Conflict of interest

The authors declare that they have no known competing financial interests or personal relationships that could have appeared to influence the work reported in this paper.

Author contributions

Conceptualization: Guo Dong Goh
Data curation: Jia Li Janessa Thong, Jia Jun Seah
Formal analysis: Jia Li Janessa Thong, Jia Jun Seah
Funding acquisition: Wai Yee Yeong
Investigation: Sheng Huang, Jia Li Janessa Thong, Jia Jun Seah
Methodology: Xi Huang
Project administration: Wai Yee Yeong
Resources: Wai Yee Yeong
Supervision: Wai Yee Yeong
Validation: Guo Dong Goh
Writing – original draft: Jia Li Janessa Thong
Writing – review & editing: Guo Dong Goh

Data availability

Data are available on request.

References

1. Liu S, Shin YC, 2019, Additive manufacturing of Ti6Al4V alloy: A review. *Mater Des*, 164: 107552.

   https://doi.org/10.1016/j.matdes.2018.107552

2. Elsayed M, Ghazy M, Youssef Y, *et al.*, 2019, Optimization of SLM process parameters for Ti6Al4V medical implants. *Rapid Prototyp J*, 25: 433–447.

   https://doi.org/10.1108/rpj-05-2018-0112

3. Roudnicka M, Bigas J, Vojtech D, 2020, Tuning porosity and mechanical properties of Ti6Al4V alloy additively manufactured by SLM. In: Key Engineering Materials. Vol. 865. Trans Tech Publications, Switzerland, p1–5.

4. Popovich A, Sufiiarov V, Borisov E, *et al.*, 2015, Microstructure and mechanical properties of Ti-6Al-4V manufactured by SLM. In: Key Engineering Materials. Vol. 651. Trans Tech Publications, Switzerland, p677–682.

5. Thijs L, Verhaeghe F, Craeghs T, *et al.*, 2010, A study of the microstructural evolution during selective laser melting of Ti-6Al-4V. *Acta Mater*, 58: 3303–3312.

   https://doi.org/10.1016/j.actamat.2010.02.004

6. Kuo C, Su C, Chiang A, 2017, Parametric optimization of density and dimensions in three-dimensional printing of Ti-6Al-4V powders on titanium plates using selective laser melting. *Int J Precis Eng Manuf*, 18: 1609–1618.

   https://doi.org/10.1007/s12541-017-0190-5

7. Pal S, Lojen G, Kokol V, *et al.*, 2018, Evolution of metallurgical properties of Ti-6Al-4V alloy fabricated in different energy

densities in the Selective Laser Melting technique. *J Manuf Process*, 35: 538–546.

https://doi.org/10.1016/j.jmapro.2018.09.012

8. Gong H, Rafi K, Starr T, *et al.*, 2013, The Effects of Processing Parameters on Defect Regularity in Ti-6Al-4V Parts Fabricated by Selective Laser Melting and Electron Beam Melting. In: Conference 24th Annual International Solid Freeform Fabrication Symposium.
9. Kasperovich G, Haubrich J, Gussone J, *et al.*, 2016, Correlation between porosity and processing parameters in TiAl6V4 produced by selective laser melting. *Mater Des*, 105: 160–170.

   https://doi.org/10.1016/j.matdes.2016.05.070
10. Ali H, Ma L, Ghadbeigi H, *et al.*, 2017, *In-situ* residual stress reduction, martensitic decomposition and mechanical properties enhancement through high temperature powder bed pre-heating of Selective Laser Melted Ti6Al4V. *Mater Sci Eng A*, 695: 211–220.
11. Vilaro T, Colin C, Bartout JD, 2011, As-fabricated and heat-treated microstructures of the Ti-6Al-4V alloy processed by selective laser melting. *Metall Mater Trans A*, 42: 3190–3199.

    https://doi.org/10.1007/s11661-011-0731-y
12. Qiu C, Adkins NJ, Attallah MM, 2013, Microstructure and tensile properties of selectively laser-melted and of HIPed laser-melted Ti-6Al-4V. *Mater Sci Eng A*, 578: 230–239.

    https://doi.org/10.1016/j.msea.2013.04.099
13. Xu Y, Zhang D, Guo Y, *et al.*, 2020, Microstructural tailoring of As-selective Laser melted Ti6Al4V alloy for high mechanical properties. *J Alloys Compd*, 816: 152536.

    https://doi.org/10.1016/j.jallcom.2019.152536
14. Pal S, Gubeljak N, Hudak R, *et al.*, 2019, Tensile properties of selective laser melting products affected by building orientation and energy density. *Mater Sci Eng A*, 743: 637–647.

    https://doi.org/10.1016/j.msea.2018.11.130
15. Sun J, Yang Y, Wang D, 2013, Parametric optimization of selective laser melting for forming Ti6Al4V samples by Taguchi method. *Opt Laser Technol*, 49: 118–124.

    https://doi.org/10.1016/j.optlastec.2012.12.002
16. Bartolomeu F, Faria S, Pinto E, *et al.*, 2016, Predictive models for physical and mechanical properties of Ti6Al4V produced by Selective Laser Melting. *Mater Sci Eng A*, 663: 181–192.

    https://doi.org/10.1016/j.msea.2016.03.113
17. Fotovvati B, Namdari N, Dehghanghadikolaei A, 2018, Fatigue performance of selective laser melted Ti6Al4V components: State of the art. *Mater Res Express*, 6: 012002.

    https://doi.org/10.1088/2053-1591/aae10e
18. Goh GD, Sing SL, Yeong WY, 2020, A review on machine learning in 3D printing: Applications, potential, and challenges. *Artif Intell Rev*, 54: 63–94.

    https://doi.org/10.1007/s10462-020-09876-9
19. Steiner S, Zeng Y, Young TM, *et al.*, 2016, A study of missing data imputation in predictive modeling of a wood-composite manufacturing process. *J Qual Technol*, 48: 284–296.

    https://doi.org/10.1080/00224065.2016.11918167
20. Wang Y, Li K, Gan S, *et al.*, 2019, Missing data imputation with OLS-based autoencoder for intelligent manufacturing. *IEEE Trans Ind Appl*, 55: 7219–7229.

    https://doi.org/10.1109/TIA.2019.2940585
21. Andridge RR, Little RJ, 2010, A review of hot deck imputation for survey non-response. *Int Stat Rev*, 78: 40–64.

    https://doi.org/10.1111/j.1751-5823.2010.00103.x
22. Jadhav A, Pramod D, Ramanathan K, 2019, Comparison of performance of data imputation methods for numeric dataset. *Appl Artif Intell*, 33: 913–933.

    https://doi.org/10.1080/08839514.2019.1637138
23. Altman NS, 1992, An introduction to Kernel and nearest-neighbor nonparametric regression. *Am Stat*, 46: 175–185.

    https://doi.org/10.2307/2685209
24. Imandoust SB, Bolandraftar M, 2013, Application of K-nearest neighbor (KNN) approach for predicting economic events: Theoretical background. *Int J Eng Res Appl*, 3: 605–610.
25. Wilson DR, Martinez TR, 2000, Reduction techniques for instance-based learning algorithms. *Mach Learn*, 38: 257–286.

    https://doi.org/10.1023/A:1007626913721
26. sklearn.impute.KNNImputer-scikit-learn 0.23.2 documentation. Available from: https://scikit-learn.org/stable/modules/generated/sklearn.impute.KNNImputer.html [Last accessed on 2020 Oct 05].
27. sklearn.metrics.pairwise.nan_euclidean_distances-scikit-learn 0.23.2 documentation. Available from: https://scikit-learn.org/stable/modules/generated/sklearn.metrics.pairwise.nan_euclidean_distances.html [Last accessed on 2020 Oct 05].
28. Van Buuren S, Groothuis-Oudshoorn K, 2010, Mice: Multivariate imputation by chained equations in R. *J Stat Softw*, 45: 1–67.

    https://doi.org/10.18637/jss.v045.i03
29. Azur MJ, Stuart EA, Frangakis C, *et al.*, 2011, Multiple imputation by chained equations: What is it and how does it work? *Int J Methods Psychiatr Res*, 20: 40–49.

    https://doi.org/10.1002/mpr.329
30. Rubin DB, 1987, Multiple Imputation for Nonresponse in Surveys (Wiley Series in Probability and Statistics). John

Wiley and Sons Inc., New York.

https://doi.org/10.1002/9780470316696

31. 6.4. Imputation of Missing Values-scikit-learn 0.23.2 Documentation. Available from: https://scikit-learn.org/stable/modules/impute.html#multiple-vs-singleimputation [Last accessed on 2020 Oct 05].

32. Shah AD, Bartlett JW, Carpenter J, *et al.*, 2014, Comparison of random forest and parametric imputation models for imputing missing data using MICE: A CALIBER study. *Am J Epidemiol*, 179: 764–774.

    https://doi.org/10.1093/aje/kwt312

33. Spinelli I, Scardapane S, Uncini A, 2020, Missing data imputation with adversarially-trained graph convolutional networks. *Neural Netw*, 129: 249–260.

    https://doi.org/10.1016/j.neunet.2020.06.005

34. Kohonen T, 1982, Self-organized formation of topologically correct feature maps. *Biol Cybern*, 43: 59–69.

    https://doi.org/10.1007/BF00337288

35. Moosavi V, Packmann S, Vallés I, 2014, SOMPY: A Python Library for Self Organizing Map (SOM). Available from: https://www.github.com/sevamoo/sompy [Last accessed on 2020 Oct 05].

36. Qian J, Nguyen NP, Oya Y, *et al.*, 2019, Introducing self-organized maps (SOM) as a visualization tool for materials research and education. *Results Mater*, 4: 100020.

    https://doi.org/10.1016/j.rinma.2019.100020

37. Nguyen CD, Carlin JB, Lee KJ, 2017, Model checking in multiple imputation: an overview and case study. *Emerging Themes Epidemiol*, 14: 8.

    https://doi.org/10.1186/s12982-017-0062-6

38. Metelkova J, Kinds Y, Kempen K, *et al.*, 2018, On the influence of laser defocusing in Selective Laser melting of 316L. *Addit Manuf*, 23: 161–169.

    https://doi.org/10.1016/j.addma.2018.08.006

39. Slobodzian GE. White Paper-apples to Apples: Which Camera Technologies Work Best for Beam Profiling Applications, Part 2: Baseline Methods and Mode Effects. Available from: https://www.ophiropt.com/laser--measurement/knowledge-center/article/8065 [Last accessed on 2020 Oct 12].

40. Kuruvilla M, Srivatsan TS, Petraroli M, *et al.*, 2008, An investigation of microstructure, hardness, tensile behaviour of a titanium alloy: Role of orientation. *Sadhana*, 33: 235–250.

    https://doi.org/10.1007/s12046-008-0017-2

41. Jiang PF, Zhang CH, Zhang S, *et al.*, 2021, Additive manufacturing of novel ferritic stainless steel by selective laser melting: Role of laser scanning speed on the formability, microstructure and properties. *Opt Laser Technol*, 140: 107055.

    https://doi.org/10.1016/j.optlastec.2021.107055

42. Wang Z, Xiao Z, Tse Y, *et al.*, 2019, Optimization of processing parameters and establishment of a relationship between microstructure and mechanical properties of SLM titanium alloy. *Opt Laser Technol*, 112: 159–167.

    https://doi.org/10.1016/j.optlastec.2018.11.014

ACCSCIENCE PUBLISHING

Materials Science in Additive Manufacturing

ORIGINAL RESEARCH ARTICLE

Energy absorption and recoverability of Moore space-filling thin-walled structures

Changlang Wu, Vuong Nguyen-Van, and Phuong Tran*

School of Engineering, RMIT University, Melbourne, VIC 3000, Australia

Abstract

This paper proposes novel thin-walled structures inspired by Moore space-filling curves. Nine designs, featuring three fractal hierarchies (1st, 2nd, and 3rd orders) with three different relative densities (20%, 30%, and 40%), were used as cross-sectional configurations of the thin-walled structures. Specimens were manufactured using a material extrusion additive manufacturing technique, fused filament fabrication, with a carbon fiber-reinforced composite. Quasi-static compression tests from in-plane direction were conducted to investigate the influences of fractal hierarchy and relative density on the energy absorption capacity. Finite element models were developed to compare with the experiments and to further explore the 4th order structures. A certain level of compliance and snap-in instability were observed in all the structures. These properties show great potential for such thin-walled structures to absorb more energy by enduring large strain. Among them, the 2nd order structures exhibited the best energy absorption capacity. Furthermore, loading and unloading compression tests were performed on the 2nd and 3rd order structures (relative density of 20%) to evaluate their resilience toward displacement and damages. The residual strain and dissipated energy ratio demonstrated that the 2nd order structure outperformed the 3rd order structure owing to its less compliant feature. The integration of Moore curves with thin-walled structures contributes to great compliance and snap-in instability, offering a new approach to designing lightweight energy absorption structures.

Keywords: Fractal; Compliant structures; Snap-in instability; Energy absorption; Additive manufacturing

***Corresponding author:**
Phuong Tran
(jonathan.tran@rmit.edu.au)

Citation: Wu C, Nguyen-Van V, Tran P, 2023, Energy absorption and recoverability of Moore space-filling thin-walled structures. *Mater Sci Add Manuf*, 2(1): 53. https://doi.org/10.36922/msam.53

Received: February 20, 2023

Accepted: March 7, 2023

Published Online: March 24, 2023

Copyright: © 2023 Author(s). This is an Open Access article distributed under the terms of the Creative Commons Attribution License, permitting distribution, and reproduction in any medium, provided the original work is properly cited.

Publisher's Note: AccScience Publishing remains neutral with regard to jurisdictional claims in published maps and institutional affiliations.

1. Introduction

Energy absorption has always been one of the design objectives to provide protection to humans and structures during dynamic or impact events, such as high specific energy absorption (SEA)[1-4], lightweight[5-8], low cost[5,9,10], and easy installation[11,12]. Among various types of structures, thin-walled structures have been widely used as effective energy absorbers in civil engineering, automobile engineering, aerospace engineering, etc., considering its excellent energy absorbing capacity and lightweight features[13]. Over the past decades, designing lightweight thin-walled structures without sacrificing their energy absorption or crashworthiness has become a hot research topic. It has been demonstrated that the energy absorption capacity of thin-walled structures is influenced by various factors, such as structural configuration, material selection, and trigger arrangement. Among them, the cross-section profile is one of the most critical factors[13]. Various shapes have been explored for the outer layer tubes, including triangle[14,15], square[16-18], pentagon[19], hexagon[20], and circle[14,15,21,22] and more recently different cross-section designs for the infill have been proposed and elaborated[23-25].

When it comes to cross-sectional configurations, nature-inspired patterns are often employed due to its multi-functional features and outperformed characteristics[26,27]. One of the fascinating patterns that could be found in nature is the fractal, for instance, the galaxy and seashell. Fractal, as defined in mathematics, is a geometry that resembles itself at various scales[28]. Several studies investigating the crashworthiness of fractal-inspired thin-walled structures (Figure 1) have provided a new approach to designing novel lightweight energy absorbers with improved crashing characteristics[29-32]. In 2018, Zhang *et al.*[23] investigated the crashworthiness of fractal hierarchical hexagon thin-walled structures that were inspired by spider webs. Fractal configurations, geometrical parameters, and fractal orders have proven to play important roles in energy absorption. Besides, Wang *et al.*[24] proposed a thin-walled structure design with cross-sections of Koch snowflakes. Interestingly, the 2nd order Koch snowflake design outperformed a wide range of multi-cell structures with the same mass, thus supporting the argument proposed by Zhang *et al.*[23]. Numerically and analytically, Huang *et al.*[26] introduced a gradient fractal thin-walled structure inspired by bamboos to improve the SEA, comparing to conventional square honeycombs. Again, the 2nd order fractal tube yielded the best energy absorption per unit mass.

To improve the energy absorption capacity of fractal-inspired thin-walled structures, reinforcements have been used as infills. In early 2000, hollow foam-filled tubes were studied analytically and numerically to demonstrate the higher weight-efficiency in energy absorption[33]. Compared to tubes without foam-infill, hollow foam-filled tubes exhibited higher energy absorption capacity with the same mass. Similarly, Dadrasi *et al.*[34] conducted a study to compare the crashworthiness of another fractal-pattern inspired thin-walled columns with and without foam-infill.

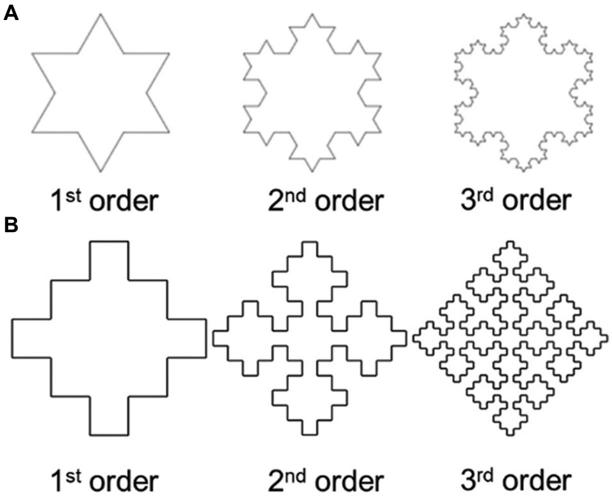

Figure 1. Fractal cross-sections employed in thin-walled structure design: (A) Koch snowflake; (B) Sierpiński curve.

The previous studies have focused on the out-of-plane crashworthiness of structures as vertical thin-walls are known to provide strength and stiffness. Moreover, most of the structures have integrated fractal patterns with a thin-walled tube as the outer layer to improve their mechanical properties. However, this outer layer tube adds extra weight and cost.

Furthermore, fatigue damage also plays an important role in energy absorption[35,36]; therefore, cyclic performance is critical for energy absorption in engineering applications[37]. An energy absorbing device with low recoverability after cyclic loading is likely to have a short lifespan, which could potentially lead to casualties, structural damages, and extra maintenance cost. However, loading and unloading cyclic compression experiments have not been studied on any fractal-inspired thin-walled structures. Moore space-filling curves, as another type of fractal structure, are rarely used as the design motif for thin-walled structures. Space-filling curves are characterized by a unique feature, that is, a finite area would be filled with a curve of infinite length after an infinite number of iterations. Theoretically, Moore space-filling curves could fill a limited design space with infinite length of curves. For a given relative density of thin-walled structures, the cross-section could be filled with infinite space-filling curves by increasing fractal hierarchy. Thus, thin-walled structures with such cross-sectional configurations could offer great potential for excellent mechanical responses in the in-plane direction[38].

From the design point of view, many studies have been carried out over the past few decades on different cross-sectional shapes of thin-walled structures. However, the complex geometries of cross-sectional configurations have yet to be explored due to the limitations of conventional manufacturing technology[39]. The manufacturing process of structures with complex geometries has become easier than ever using advanced additive manufacturing (3D printing) techniques[40-42]. The main purpose of the present work was to study energy absorption for a novel compliant thin-walled structure. These newly designed infill patterns were inspired from Moore space-filling curves with three fractal hierarchies. Three relative densities, that is, 20%, 30%, and 40%, were investigated for each design. All the specimens were manufactured using fused filament fabrication (FFF), which is a low-cost additive manufacturing technology. Quasi-static compression tests and loading-unloading cyclic compression tests were also carried out to observe the mechanical responses and evaluate the permanent deformation of the proposed structures. Numerical models were developed and used for a parametric study to further analyze the mechanical behaviors.

2. Methodology

2.1. Design and fabrication of compliant structures

The novel metamaterials were inspired from a series of space-filling infill patterns, known as Moore curves. As illustrated in Figure 2A, this set of curves consisted of many orders. The 0th order was constructed by connecting the centers of each small square from the bottom left to the bottom right. The 1st order comprised four of the 0th order in a smaller scale with certain rotations. By repeating the same procedure, the 2nd and 3rd order curves were derived (Figure 2A). By connecting the opening with a straight line and smoothing the corner using cubic spline function, the cross-section centerline was constructed. All the curvatures at the same locations were constant for all designs; the only design parameter was wall thickness. The structures were constructed by assigning certain thickness to the wall and extrusion along the out-of-plane direction.

The first three orders of Moore curves were adopted to investigate the influence of fractal hierarchy on energy absorption capacity. In addition, three different relative densities were applied, that is, 20%, 30%, and 40%, to explore the effect of relative density on mechanical responses. All the proposed designs had a depth of 15 mm (in-plane depth) and a side length of 50 mm. In other words, the block size (width × length × height) was 50 × 50 × 15 mm. To achieve three relative densities, the wall thickness was adjusted accordingly, as shown in Table 1.

The samples were fabricated with a composite material, onyx, using an FFF printer, MarkTwo (Markforged Inc., USA). The onyx, provided by Markforged, was composed of nylon (80 vol%) and short carbon fibers (20 vol%). The carbon fibers were 200 μm in length and orientated in the printing direction[43]. An extruder of 0.4 mm in diameter was used for filament deposition. The printing parameters were the same for all specimens: 0.1 mm layer height, single-layer outline, and solid infill with a −45°/45° pattern. For each layer, the extruder travelled along the outlines of the structure first and filled the space in between the outlines. Therefore, the thinnest wall thickness that could be fabricated using Markforged was 0.8 mm (twice of the resolution). Based on this principle, the smallest relative density of 20% was adopted to ensure the printing quality. In addition, the limitation of wall thickness restricted the fractal hierarchy up to the 3rd order. The 3D-printed thin-walled structures with a relative density of 20%, 30%, and 40% are presented in Figure 2B-D, respectively.

The thickness of the fabricated specimens was measured from several regions of the cross-sections to compare to the design values (Table 1). Overall, the 3D-printed structures were slightly thicker than the original designs. One reason could be the high extrusion flow rate, resulting in over-extrusion of filament and a thicker print line. Within each specimen, the wall thickness was not consistent due to machine inaccuracy from FFF printing. As an important printing parameter, the pressure in the extruder influences the filament thickness during the

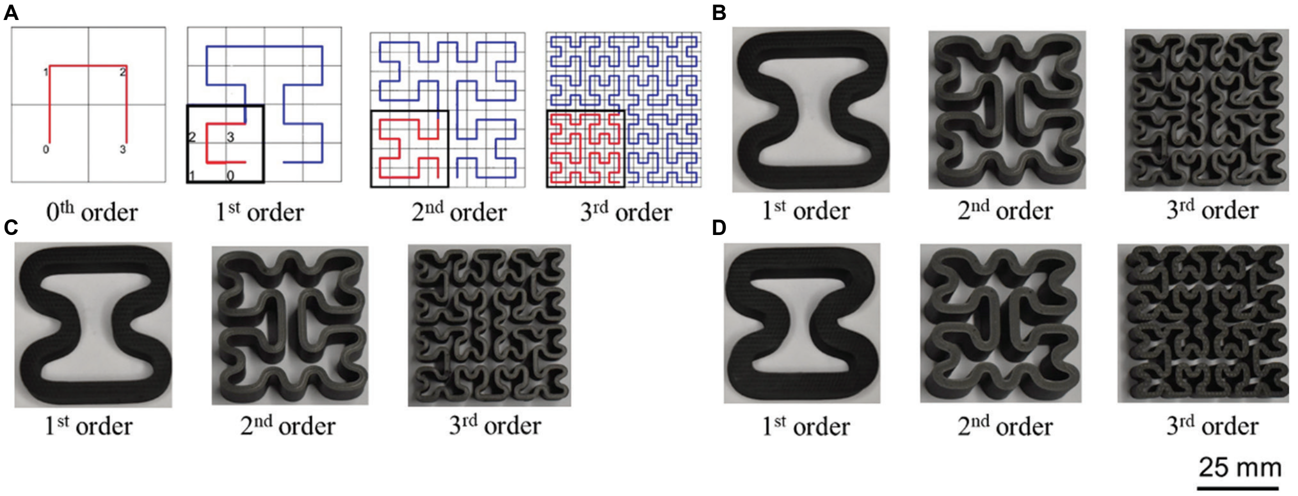

Figure 2. (A) First three hierarchies of theoretical Moore curves. Manufactured Moore curve-inspired thin-walled structures with a relative density of (B) 20%, (C) 30%, and (D) 40%.

Table 1. Wall thickness comparison between designs and as-fabricated specimens

Wall thickness (mm)	1st order		2nd order		3rd order	
	Designed	Fabricated	Designed	Fabricated	Designed	Fabricated
rd=20%	3.110	3.17–3.27	1.610	1.60–1.83	0.840	0.85–0.89
rd=30%	4.665	4.66–4.88	2.415	2.58–2.67	1.260	1.35–1.42
rd=40%	6.220	6.16–6.32	3.220	3.22–3.43	1.680	1.75–1.93

rd: Relative density. Measurements of fabricated specimens were made using a caliper with precision of two decimal places

printing process of each layer. The extruder is expected to generate a filament line with uniform width. However, a thin print line in the beginning may widen as the nozzle pressure increases. This could be more distinct when printing curves, which is a characteristic feature in Moore curve-inspired structures.

2.2. Quasi-static and cyclic compression tests

Uniaxial compression tests were performed using Instron's universal testing machine (5900R Series), with a 30 kN load cell. A loading rate of 2 mm/min was applied to all testings. Unit cells were compressed up to 70% strain (displacement of 35 mm) from two in-plane directions. Three specimens were tested for each design to ensure the reliability of results. Force-displacement data and real-time videos were captured and recorded from the experiment to study the responses of different structures. To further investigate the energy absorption performance of the metamaterials, loading and unloading compression tests were conducted. Herein, cyclic experiments were adopted to obtain the structural response of low cyclic-loading events, such as earthquake[44]; however, fatigue was not considered. Six cycles were applied to each specimen. Force-displacement curves were captured to estimate energy absorption and then converted to effective stress-strain curves to evaluate the residual strain.

SEA, which is defined as the amount of energy absorbed by the material per unit mass, has been widely used as a parameter to indicate the energy absorption capacity of a crushed material[45]. SEA can be calculated by integrating the force-displacement curve (Figure 3A) and then divided by the total mass of materials[43]:

$$SEA = \int_0^d \frac{F(x)}{m} \mathrm{d}x, \tag{I}$$

Where F (x) is the reaction force captured by load cell during experiment, x denotes the compression displacement, and m is the mass of the structure.

To compare the performance of different designs, effective stress-strain curves were derived from force-displacement curves and compared. The following equations were used to calculate the effective axial stress (σ^*_{yx}) and effective axial strain (ε^*_{yx}) in the y-direction (compression direction):

$$\sigma^*_{yx} = \frac{R_y}{A_y}, \tag{II}$$

$$\varepsilon^*_{yx} = \frac{\delta_y}{L_y} \tag{III}$$

Where R_y is the total reaction force from the structure, while A_y is the cross-sectional area of the whole structure that is perpendicular to the y-direction; L_y denotes the height of the structure (length along y-direction), while δ_y is the total displacement experienced by the structures along the y-direction.

For cyclic testings, two parameters were used to evaluate the performance of the structures. First, residual strain was measured after the first and all six loading-unloading cycles to assess the amount of plastic deformation. Second, dissipated energy, which is referred as plastic strain energy, was calculated by subtracting the released energy during the reloading period from the stored energy during the loading period (Figure 3B)[46].

Based on the definition of dissipated energy ($E_{dissipated}$), it was calculated from the force-displacement curve accordingly:

$$E_{stored} = \int_0^{x^n_{max}} F(x)^n_{loading}\, dx \tag{IV}$$

$$E_{released} = \int_0^{x^n_{max}} F(x)^n_{unloading}\, dx, \tag{V}$$

$$E_{dissipated} = E_{stored} - E_{released}, \tag{VI}$$

Where E_{stored} is the sum of energy stored in the structure during all loading cycles, $E_{released}$ is the sum of energy released from the structure during all unloading cycles, and n is the total number of loading and unloading cycles.

To evaluate the resilience of the proposed structures toward permanent deformation and potential damage

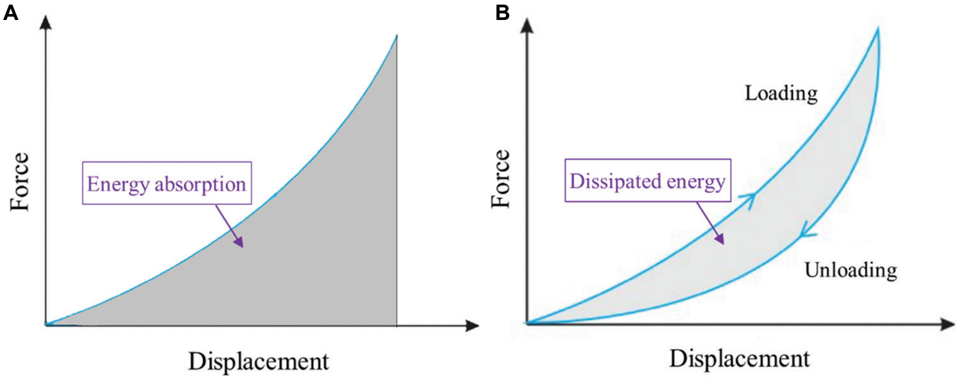

Figure 3. (A) Energy absorbed by the structure represented by the area under force-displacement curve. (B) Energy dissipated by the structure represented by the area between the loading and unloading force-displacement curve.

caused by cyclic loading, we used an energy dissipation ratio (η), which is defined as the ratio between total dissipated energy and total stored energy:

$$\eta = \frac{E_{dissipated}}{E_{stored}} \quad \text{(VII)}$$

2.3. Numerical models and convergence study

A 3D nonlinear quasi-static finite element (FE) model was developed to simulate the response of the structures under compression loading using the commercial software package Abaqus/Explicit 2020 (Dassault Systems SIMULIA Corp., Providence, RI). The material properties used in the model were obtained from the tensile tests on 3D-printed onyx specimens under ASTM D638, rendering a Young's modulus value of 1,800 MPa and a yield stress of 61 MPa. Adopted from the onyx datasheet provided by Markforged, the density and Poisson's ratio were 1.2 g/cm^3 and 0.3, respectively.

To reduce the computational cost and maintain large-scale simulation, the model was simplified by using shell elements considering a constant wall thickness. The linear four-node shell elements (S4R) were used to simulate the fractal structures. Considering that the metallic compression plates of Instron's universal testing machine were much stiffer than the 3D-printed Onyx samples, two rigid plates were modeled for simplification. The shell elements were defined to have a normal contact behavior using hard contact formulation, while a friction coefficient of 0.3[47] was utilized to describe the tangential responses. Two reference points were created, with rigid body constraints applied between them and the rigid plates. By controlling the boundary conditions on the two reference points, the uniaxial compression test conditions were simulated (Figure 4). A displacement of 35 mm was applied at the top reference point, while an all-direction fixed boundary condition was assigned to the bottom reference point.

Besides, the optimal mesh size was decided after carrying out convergence study on the 2nd order fractal structure (relative density of 20%) loaded from both directions. Mesh sizes of 0.5 mm, 0.75 mm, 1.5 mm, and 3 mm were applied for the shell elements. Results of the reaction force versus displacement curves obtained from simulations are shown in Figure 4C and D, corresponding to loading direction 1 (LD1) and loading direction 2 (LD2), respectively. It could be inferred that the mesh size of 0.75 mm is the optimal considering the model accuracy and computational cost.

Furthermore, a parametric study on 4th order fractal-inspired thin-walled structures was conducted using FE simulations. Limited by Markforged printer's resolution, 4th order structures with relative densities of 20%, 30%, and 40% could not be manufactured. Using the FE model, the energy absorption of higher-order fractal-inspired structures was studied.

3. Results and discussion

3.1. Effective stress-strain curves

3.1.1. Quasi-static compression test results

The quasi-static compression test of the 2nd order fractal sample is illustrated in Figure 5D. The responses of the metamaterials under quasi-static compressive load from in-plane direction 1 are shown in Figure 5A-C, corresponding to three different relative densities (20%, 30%, and 40%, respectively). Curves were constructed using the mean effective stress value from three testing results. Overall, all the structures underwent large strains with very low stress. Excellent compliance was observed up to around 50% strain. As suggested in Figure 5A-C, the 3rd order thin-walled structures with a relative density of 20% yielded the most compliant behavior.

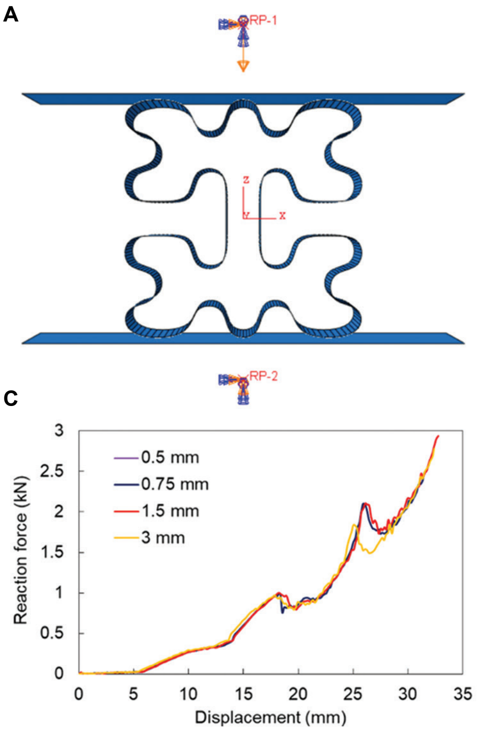

Figure 4. Boundary conditions on reference points to simulate 2nd order fractal structures with shell elements from (A) loading direction 1 (LD1) and (B) loading direction 2 (LD2). Mesh size convergence study on the 2nd order (20% relative density) structure from (C) LD1 and (D) LD2.

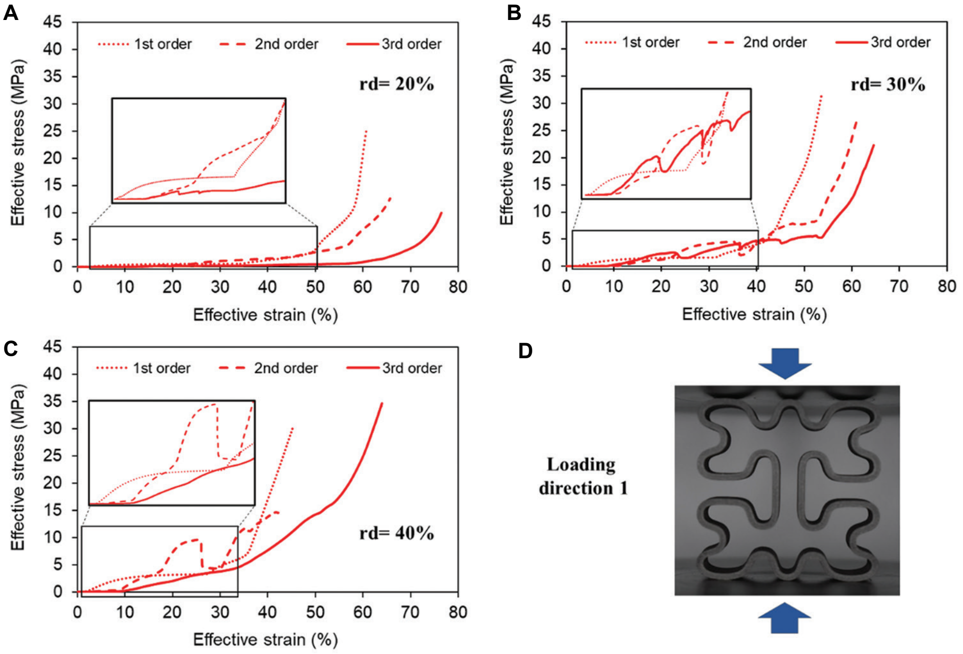

Figure 5. Effective stress-strain curves obtained from quasi-static compression test from loading direction 1 (LD1): (A) Relative density (rd) = 20%, (B) rd = 30%, and (C) rd = 40%. (D) 2*nd* order structure being compressed from LD1. Magnified images in A–C provide clearer views for comparing the beginning responses during compression.

Another characteristic feature of all the effective stress-strain curves was the jagged pattern, which suggested numerous sudden stress drops from the snap within the structures during compression. The snaping was attributed to the nature of space-filling curves and the smooth-corner design. When being compressed, some parts of the structure collided with other parts. Since Moore space-filling curves meander within a limited space, the concave and the adjacent convex tend to snap into each other. Due to snap-in instability, stress within the structure redistributes and decreases. Instead of densification, these fractal structures utilize their compliance to endure more strain before failure.

When applying load from in-plane direction 2, the structures behaved in a different way compared to LD1 (Figure 5). Effective stress-strain curves for three different relative densities are shown in Figure 6. Similar to responses from LD1, structures with 20% relative density experienced larger strain under the same effective stress compared to those with a higher relative density. For the same relative density, the 3rd order structures demonstrated the most compliant behavior. Comparing to the responses from LD1, the stress-strain curves were more jagged. This could be explained by more curvature changes of the cross-section in vertical direction when compressed from LD2. The snap-in behavior was prominent especially for the 1st order structure, followed by the 2nd and 3rd order structures. While the drops in the effective stress-strain curves for the 2nd and 3rd order structures became smaller, the number of total drops increased due to the nature of space-filling curves.

Among all the curves, the response from LD2 for the 3rd order structure with 30% relative density was the most jagged. To understand the reasons behind these stress drops in all the stress-strain curves, the behaviors of the 3rd order structure (30% relative density) observed from the experiment are presented in Figure 7. Structural deformations at strains of 15%, 20%, 25%, 30%, 35%, 40%, and 45% are displayed to provide a clearer picture of the dramatic stress drops at points A, B, and C (highlighted in the stress-strain curve). From the original configuration to a strain of 15%, the thin-walled structure contracted in a perpendicular direction due to the gaps in the space curve. Thereafter, there was contact within the structure itself, as shown in the deformation at a strain of 20%. Collisions within the structure led to one convex part snapping-in to an adjacent concave part, which could be found in the magnified images in Figure 7.

For instance, at a strain of 25%, the two convex parts, as shown in the solid green square in Figure 7, were confronting each other. With increasing load, the top convex slipped all the way into the concave gap on its bottom right (green dashed square in Figure 7 at a strain of 30%). The sudden snap-in was an instability created by the features of Moore curves and the smooth-corner design of the thin-walled structures. Stress was redistributed due to the snap-in behavior within a short time, leading to stress drop A (stress-strain curve in Figure 7). A similar phenomenon

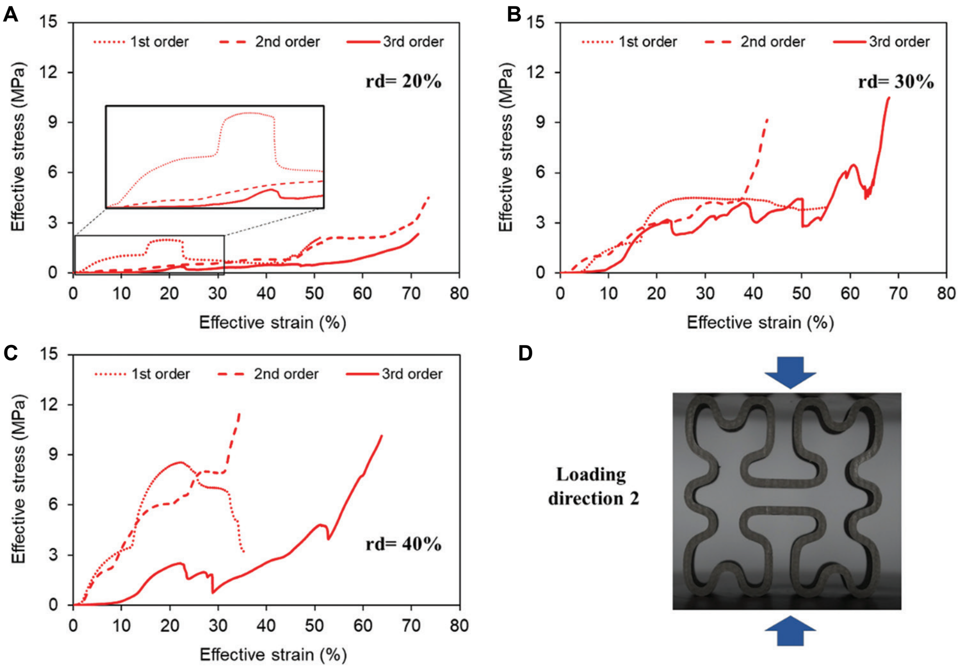

Figure 6. Effective stress-strain curves obtained from quasi-static compression test from loading direction 2 (LD2): (A) Relative density (rd) = 20%, (B) rd = 30%, and (C) rd = 40%. (D) 2nd order structure being compressed from LD2. The magnified image in A provides a clearer view for comparing the beginning responses during compression.

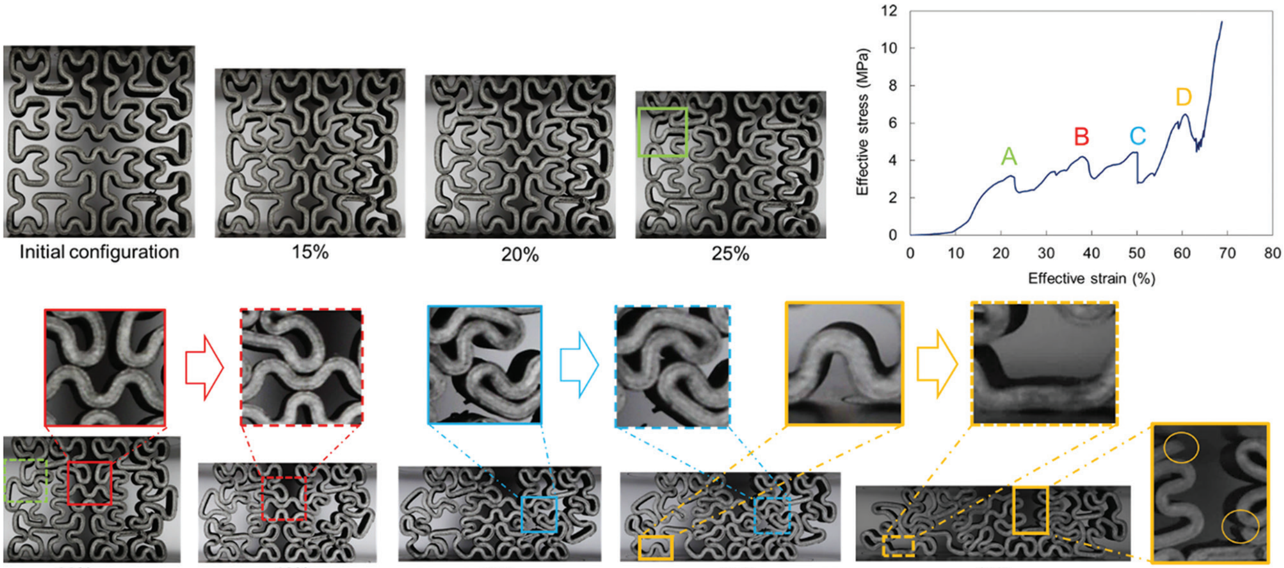

Figure 7. Configurations of 3rd order structure (relative density of 30%) during compression at different strains. Squares colored green, red, and blue show the deformation change of the structure causing stress drops A, B, C, and D, respectively, as highlighted in the stress-strain curve. Magnified images showing the snap-in behaviors, straightening of curved elements, and failure within the structure.

was observed at compression strains of 40% and 50%, corresponding to stress drops B and C, respectively. The basis of the descend after local peak D was the straightening of curved elements and damages within the structure (see yellow magnified images in Figure 7). Compared with the 1st and the 2nd order structures, the 3rd order structure showed a more complex cross-sectional geometry with more concave/convex. Hence, the response of the 3rd order structure demonstrated more drops in stress.

3.1.2. Cyclic loading test results

As observed from the results of the quasi-static compression tests, the 2nd and 3rd order metamaterials with relative density of 20% revealed their characteristic compliance feature. Hence, a cyclic compression test with six loading-unloading cycles was performed to further investigate the energy absorption performance of fractal-inspired thin-walled structures. Figure 8 shows the effective stress-stain curves for both 2nd and 3rd order structures under cyclic loading from direction 1 and 2. Overall, for each design, the response of the first cycle was different from the following five cycles. The structure behaved in a similar way during the last five cycles regardless of the loading direction, demonstrating the reliability and recoverability of the structures to some extent. In other words, most of the plastic deformation during the whole cyclic loading test occurred in the first cycle[48].

Besides, the 2nd order structure appeared to have higher recoverability after cyclic loading than the 3rd order structure through a comparison of their post-mortem deformations (Figure 8). The deformed shapes of the specimens before and after cyclic loading are illustrated in Figure 8. The 2nd order structure maintained its original shape with a certain degree of contraction, while the 3rd order structure experienced significant permanent deformation.

3.2. FE model validation

The FE simulation results were validated by comparing to the experimental outcomes in terms of the effective stress-strain curves of the fractal structures with a relative density of 20% (Figure 9). The behaviors from numerical simulation were close to what was observed from the experiment. However, there were still some discrepancies. Figure 9 presents the effective stress-strain curves from the experiments and simulations. In general, the strain and stress predicted from numerical models were higher than those captured in experiments. In the simulation, there was no obvious sliding between rigid plates and fractal structures. Nevertheless, the top and bottom of the fractal structures that were in contact with the metal compression plates slipped along the tangential direction. Despite applying a frictional penalty of 0.3 to the tangential interaction between surfaces in the FE model, the coefficient of friction between the metal plates and the fractal structures during experiment seemed to be smaller. The sliding attributed to the lower strain and stress in the experiment compared to the simulation.

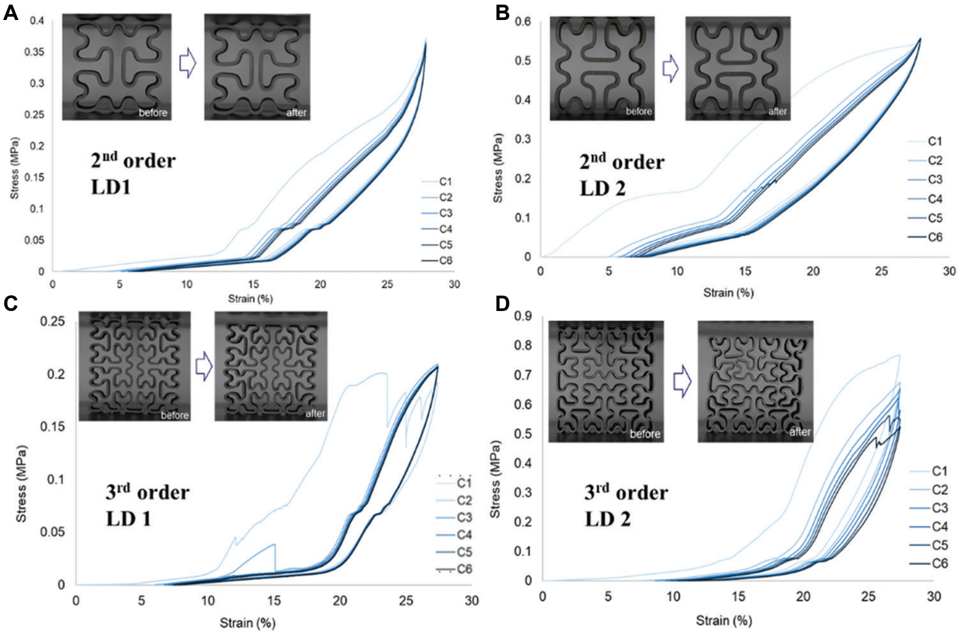

Figure 8. Effective stress- strain curves obtained from cyclic compression tests for structures with a relative density of 20%: (A) 2nd order from loading direction 1 (LD1), (B) 2nd order from loading direction 2 (LD2), (C) 3rd order from LD1, and (D) 3rd order from LD2. The pictures of the specimens are the configurations before and after the cyclic tests.

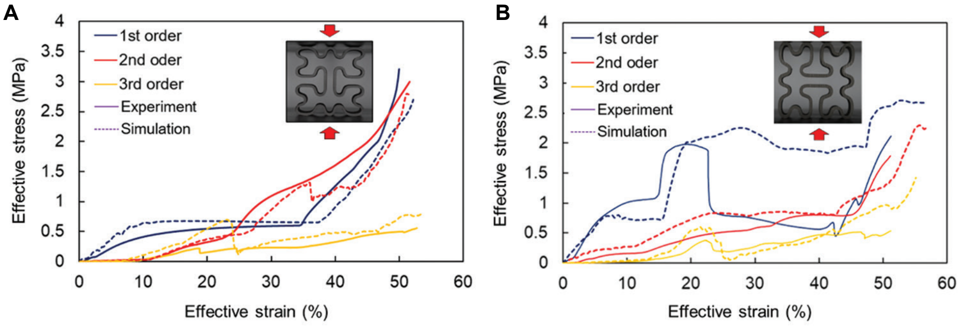

Figure 9. Comparisons of effective stress-strain curves obtained from quasi-static compression experiments and FE simulations for 2nd order fractal structure with a relative density of 20% from (A) loading direction 1 and (B) loading direction 2.

As displayed in Figure 9B, the effective stress (Equation II) within the 1st order structure in the experiment dropped drastically at a strain of 22%. However, there was no obvious reduction in stress, but rather a long phase of plateau from the numerical simulation. In other words, no snap-in was observed in the FE modeling. This is ascribed to the perfectly symmetric parts and ideal boundary conditions in the numerical model. Meanwhile, the experimental condition and 3D-printed specimens differed from what was established in the modeling. It is widely known that defects commonly exist in FFF technology using carbon fiber-reinforced polymer[49]. Any misalignment of compressive loading or imperfections within the fabricated structures could give the structures opportunity to behave in an asymmetric way, leading to the snap-in phenomenon.

When comparing the response from LD1 to LD2, the difference between the experiment and the simulation was slightly smaller. This phenomenon is a result of the design of structures. As shown in Figure 4A and B, the total contact surface between the compression plates and specimens was larger in LD1 (Figure 4A). All the specimens deformed symmetrically in the FE models considering the symmetric design. During the experiment, structures with less contact surface were more prone to deform asymmetrically due to misaligned loading conditions or manufacturing defects.

3.3. Stress distributions

Failure of engineering components is mostly due to stress within the structure. The stress distribution reflects the level of structural design and affects the structural safety performance[50]. It is important to measure and evaluate the stress distribution to ensure that the structure will maintain its integrity under a given load. Stress concentration, which indicates that the localized stress of a segment is significantly higher than the surrounding region, could cause structural failure even if the effective stress is smaller than the material yield strength. For a compliant structure, instability during compression is often accompanied by stress redistribution in a stress concentration region. Thus, it is important to study the stress distribution and observe the stress concentration regions in this study.

To better understand the behavior of structures captured in the experiment, simulations were performed with respect to various designs to observe the stress distribution within the structures. Figure 10 shows the deformation and equivalent stress distribution (von Mises stress) in the 2nd order structure (relative density of 20%) at strains of 25%, 35%, and 45%. In general, the stress was unevenly distributed at the cross-section of the fractal structure. While the concave segments (purple arrow in stress distribution at 25% strain in Figure 10) at the top and bottom were still experiencing very low stress, the four corners (yellow arrow in stress distribution at 25% strain in Figure 10) had already yielded. It is interesting to note that the fractal structures were inclined to act in an auxetic way[51]. With increasing compression load, the structures shrunk in a perpendicular direction rather than expanding. Similar responses were observed for all the fractal-inspired thin-walled structures.

Since the fractal design contains concaves and convexness, the corners with sudden change of curvature tend to induce more stress concentration than other regions. With the increase in strain, all the corners experienced very high stress except for the two corners in the middle due to the snap-ins from the adjacent structures, which attempted to expand the two middle corners and eventually led to curvature reduction. During this process, redistribution and reduction of stress occurred at these two locations. At a strain of 45%, there was accumulation of high stress at the bottom four corners (Figure 10) that were in contact with the compression plates, indicating densification.

3.4. SEA and energy dissipation

Based on the force-displacement curves directly obtained from Instron's machine, the SEAs for all nine designs were compared (Figure 11) with respect to different loading directions. SEA was calculated from 0% to 40% strains (before densification) for all structures. For both loading directions, the increase in fractal hierarchy led to less energy absorption for the relative density of 20%. With the increase in relative density, the energy absorption capacity significantly improved except for the 3rd order structure. In particular, the 2nd order structure appeared to be the most sensitive to relative density regardless of the loading direction. Specifically, the SEA for the 2nd order structure increased to more than double the amount with every 10% rise of relative density. It is interesting to note that for structures with 20% relative density, the 1st order exhibited the best energy absorption capacity among all three hierarchies. However, with increasing relative density, the efficiency of 2nd order structures in absorbing energy seemed to increase. When comparing LD1 with LD2, it could be observed that the energy absorption capacity was higher when subjected to LD2 than when subjected to LD1.

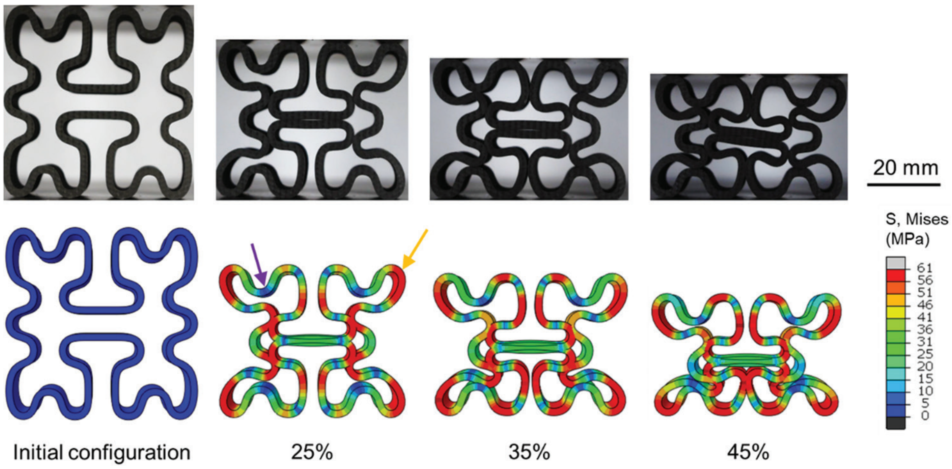

Figure 10. Deformation and stress distribution within the 2*nd* order structure (20% relative density) under compressive load from direction 2. The purple and yellow arrows refer to the typical concave and convex in the structural design. The configurations from the simulation are rendered with actual thickness.

To quantitatively evaluate the performance of fractal thin-walled structures during cyclic compression test, residual strain and dissipated energy (Equation VI) were calculated and compared in a bar chart (Figure 12). Recoverability was evaluated by the residual strain, which measures the permanent deformation of structures after a cyclic test. Dissipated energy, the strain energy dissipated in a material during cyclic loading, was calculated using stored energy during the loading period and the released energy during the unloading period. Both properties were measured after only the first cycle and after all six cycles, considering the difference in behavior during the first cycle and the remaining cycles. Overall, the energy dissipated within the first cycle was the highest among all six cycles. It could be inferred that both 2nd and 3rd order structures dissipated more energy under LD2 (Figure 12), considering the first cycle and all six cycles. Nevertheless, the residual strains in LD2 were higher than those in LD1. The dissipated energy and residual strain indicated that structures under load in direction 2 experienced more permanent deformation.

Table 2 compares the energy dissipation ratios (η) for both structures in two loading directions. The 2nd order structure had relatively smaller energy dissipation ratios than the 3rd order structure, while both structures were more efficient in LD1 (lower value of η). The residual

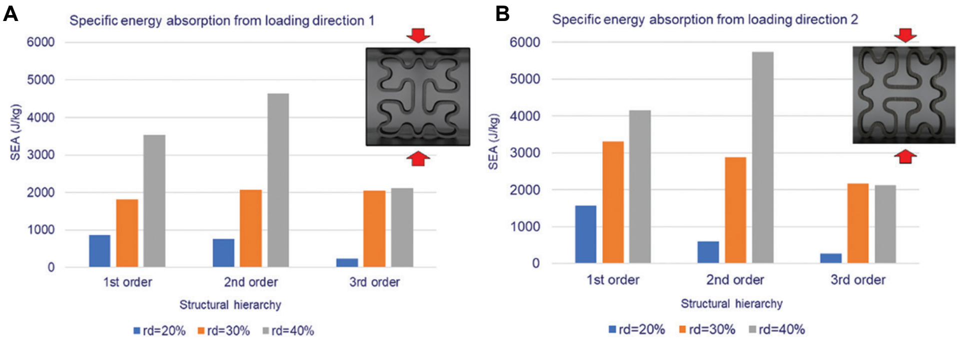

Figure 11. Specific energy absorption comparison among different hierarchies and various relative densities during quasi-static compression test from (A) loading direction 1 and (B) loading direction 2.
rd: Relative density.

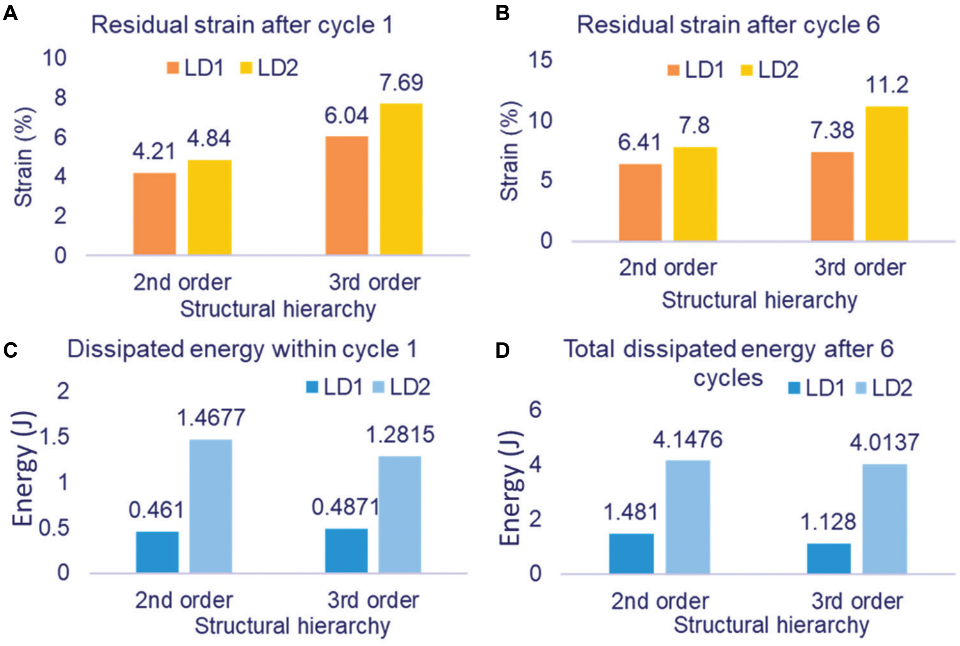

Figure 12. Comparisons for residual strain after (A) the first loading-unloading cycle and (B) all six loading-unloading cycles. Comparisons for dissipated energy after (C) the first loading-unloading cycle and (D) all six loading-unloading cycles.
LD1: Loading direction 1; LD2: Loading direction 2.

Table 2. Energy dissipation ratio for the 2nd and 3rd order structures after cyclic loading

Properties	2nd order structure		3rd order structure	
	Loading direction 1	Loading direction 2	Loading direction 1	Loading direction 2
Dissipated energy (J)	1.48	4.15	1.13	4.01
Stored energy (J)	4.57	11.11	2.64	7.82
Energy dissipation ratio	0.32	0.37	0.42	0.51

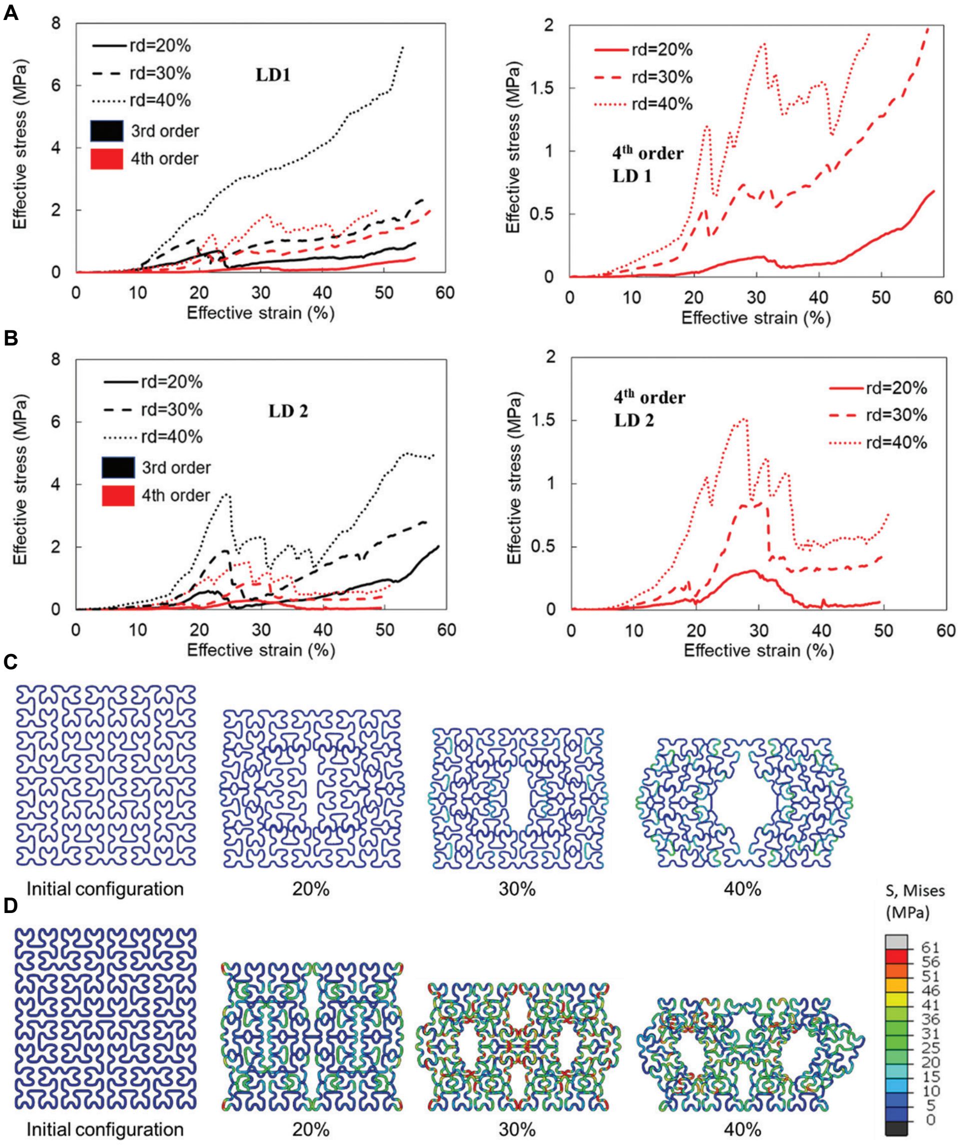

Figure 13. Comparison of effective stress-strain curves between the 3*rd* and 4*th* order structures (left panels), and magnified curves of the 4*th* order structures (right panels) obtained from FE models during quasi-static compression from (A) loading direction 1 (LD1) and (B) loading direction 2 (LD2). (C) Deformation of the 4th order structure with relative density (rd) of 20% under LD1. (D) Deformation of the 4*th* order structure with relative density of 40% under LD2. Shell elements are rendered with actual thickness.

strain and energy dissipation ratio demonstrated resilience in the 2nd order fractal-inspired thin-walled structure under cyclic loading from in-plane direction 1. This phenomenon was attributed to the less compliant behavior of the 2nd order structure when compared to the 3rd order structure.

Table 3. Specific energy absorption for the 4th order structures subjected to quasi-static compressive loadings

SEA (J/kg)	4th order structure	
	Loading direction 1	Loading direction 2
rd=20%	67.05	64.77
rd=30%	321.94	211.88
rd=40%	491.68	339.08

rd: relative density

3.5. Parametric study

A parametric study using FE simulation was conducted on 4th order structures with different relative densities to further explore the influences of fractal hierarchy and relative density on structural responses. To compare the responses of the 4th order structures with the 1st, 2nd, and 3rd order structures, the effective stress-strain curves of the 3rd order structures were used as references (Figure 13A and B). As revealed in Figure 13A and B (left panels), the 4th order structures yielded more compliant behaviors than the 3rd order structures at any given relative density in both LD1 and LD2. The increase by one fractal order led to quadruple complexity and meandering features in the cross-sectional configuration. The large number of curved segments gave rise to more snap-in instability and structural compliance, which were also manifested in more serrated stress-strain curves of the 4th order structures.

Figure 13A and B (right panels) shows clearer effective stress-strain curves of the 4th order structures, while Figure 13C and D displays the structural deformations of the 4th order structures under compression from LD1 (rd = 20%) and LD2 (rd = 30%), respectively. With the increase in relative density, the 4th order structure experienced higher stress in both in-plane directions due to its thicker wall-thickness. The drastic stress drops were created by the multiple simultaneous snap-ins (see 20% strain in Figure 13C and D). A plateau phase (Figure 13B [right panel]) in the effective stress-strain curves at a strain of 40% after the stress jump could be observed for all 4th order structures in LD2. This could be explained by the structural deformation in Figure 13D. After the 30% strain, both sides of the structure expanded outward in a transverse direction. The snap-ins along the side edges eventually unlocked and slid further outward, resulting in a long plateau phase. However, this was not observed in LD1 as only flat surface contacts, without snap-ins, occurred along the longitudinal edges (Figure 13C).

Table 3 summarizes the corresponding SEA for the 4th order structures under different loading directions. Consistent with the results obtained from the first three orders, SEA has a positive relationship with relative density for 4th order structures. However, the SEA in LD1 was more sensitive to increment in relative density compared to LD2. By comparing the values in Table 3 and Figure 11, it could be extrapolated that SEA decreases with the increase in fractal hierarchy after the 2nd order. The compliance feature and snap-in instability are more pronounced in higher orders, and the strength of the structures is sacrificed. Therefore, the energy absorption capacities are reduced for high order structures (higher than the 2nd order).

4. Conclusions

This paper presents a series of thin-walled structures inspired by Moore space-filling curves. Nine designs, featuring three hierarchies with three relative densities, that is, 20%, 30%, and 40%, were proposed and investigated. The FFF 3D printing technology was used to manufacture the samples with carbon fiber-reinforced nylon. Both quasi-static and loading-unloading compression tests were conducted to obtain and analyze the mechanical responses and energy absorption capacity of the proposed structures. Simulations were also performed to further elaborate the mechanical behaviors that were not observed from the experiment, that is, stress distribution. Herein, several conclusions were drawn.

(i) The space-filling feature of Moore curves offered great compliance to the thin-walled structures. All the fractal structures exhibited high level of flexibility, which could provide great potential for energy absorbing device with large strain endurance before failure. Fractal hierarchy was positively related to compliance, while relative density was the opposite.
(ii) The meandering pattern of Moore space-filling curves and the smooth geometry design enabled the snap-in of thin-walled structures. A certain degree of such instability reduced the stress within the structures, enhancing the energy absorption capacity. The 2nd order structures outperformed the 1st, 3rd, and 4th order structures in absorbing energy.
(iii) During quasi-static compression test, the SEA was relatively higher when subjected to LD2 than when subjected to LD1 due to the cross-sectional configuration and snap-in behavior.
(iv) In cyclic loading tests, the 2nd order structure exhibited better resilience. Smaller energy dissipation ratio and less residual strain indicated the promising ability of the 2nd order structure to resist deformation and damage from external loadings.

Overall, the proposed designs inspired by Moore space-filling curves in the present study open a new avenue for further research into the field of lightweight structures for energy absorption. The combination of thin-walled structures with space-filling curve cross-sections can provide great compliance and snap-in instability. This fractal geometry is a promising candidate in the design of lightweight energy absorption structures.

Acknowledgments

The authors acknowledge the facilities and technical assistance from the Advanced Manufacturing Precinct and Microscopy and Microanalysis Facility and at RMIT University.

Funding

This research received no external funding.

Conflict of interest

The authors declare that they have no conflict of interest.

Author contributions

Conceptualization: Phuong Tran
Data curation: Changlang Wu
Formal analysis: Changlang Wu
Methodology: Phuong Tran
Supervision: Phuong Tran
Writing – original draft: Changlang Wu
Writing – review & editing: Vuong Nguyen-Van, Phuong Tran

All authors have read and agreed to the published version of the manuscript.

Ethics approval and consent to participate

Not applicable.

Consent for publication

Not applicable.

Availability of data

The authors confirm that the data supporting the findings of this study are available within the article.

References

1. Ma Y, Sugahara T, Yang Y, *et al*., 2015, A study on the energy absorption properties of carbon/aramid fiber filament winding composite tube. *Compos Struct*, 123: 301–311.
2. Nguyen-Van V, Liu J, Peng C, *et al*., 2022, Dynamic responses of bioinspired plastic-reinforced cementitious beams. *Cement Concrete Compos*, 133: 104682.
3. Nguyen-Van V, Wickramasinghe S, Ghazlan A, *et al*., 2020, Uniaxial and biaxial bioinspired interlocking composite panels subjected to dynamic loadings. *Thin Walled Struct*, 157: 107023.
4. Nguyen-Van V, Peng C, Hazell PJ, *et al*., 2023, Performance of meta concrete panels subjected to explosive load: Numerical investigations. In: *Structural Concrete*. United States: Wiley.
5. Sun G, Chen D, Zhu G, *et al*., 2022, Lightweight hybrid materials and structures for energy absorption: A state-of-the-art review and outlook. *Thin Walled Struct*, 172: 108760.
6. Mohsenizadeh M, Gasbarri F, Munther M, *et al*., 2018, Additively-manufactured lightweight Metamaterials for energy absorption. *Mater Des*, 139: 521–530.
7. Nguyen-Van V, Tran J, Peng C, *et al*., 2020, Bioinspired cellular cementitious structures for prefabricated construction: Hybrid design & performance evaluations. *Autom Constr*, 119: p. 103324.
8. Dang BL, Nguyen-Van V, Tran P, *et al*., 2022, Mechanical and hydrodynamic characteristics of emerged porous Gyroid breakwaters based on triply periodic minimal surfaces. *Ocean Eng*, 254: 111392.
9. Meredith J, Ebsworth R, Coles SR, *et al*., 2012, Natural fibre composite energy absorption structures. *Compos Sci Technol*, 72: 211–217.
10. Yang H, Lei H, Lu G, *et al*., 2020, Energy absorption and failure pattern of hybrid composite tubes under quasi-static axial compression. *Compos B Eng*, 198: 108217.
11. Tarlochan F, AlKhatib S, 2017, Energy Absorption Capabilities of Complex Thin Walled Structures. In: IOP Conference Series: Materials Science and Engineering. United Kingdom: IOP Publishing.
12. Nguyen-Van V, Choudhry NK, Panda B, *et al*., 2022, Performance of concrete beam reinforced with 3D printed Bioinspired primitive scaffold subjected to three-point bending. *Autom Constr*, 134: 104060.
13. Fu J, Liu Q, Kangmin L, *et al*., 2019, Design of bionic-bamboo thin-walled structures for energy absorption. *Thin Walled Struct*, 135: 400–413.
14. Nia AA, Hamedani JH, 2010, Hamedani, Comparative analysis of energy absorption and deformations of thin walled tubes with various section geometries. *Thin Walled Struct*, 48: 946–954.
15. Nia AA, Parsapour M, 2014, Comparative analysis of energy absorption capacity of simple and multi-cell thin-walled tubes with triangular, square, hexagonal and octagonal sections. *Thin Walled Struct*, 74: 155–165.
16. Wang S, Xia H, Liu YJ, 2022, Energy absorption characteristics of polygonal bio-inspired honeycomb column thin-walled structure under quasi-static uniaxial compression loading. *Biomimetics* (*Basel*), 7: 201.
17. Zhang XW, Su H, Yu TX, 2009, Energy absorption of an axially crushed square tube with a buckling initiator. *Int J Impact Eng*, 36: 402–417.
18. Xing BF, Dayong H, Sun YX, *et al*., 2015, Effects of hinges and deployment angle on the energy absorption characteristics

of a single cell in a deployable energy absorber. *Thin Walled Struct*, 94: 107–119.

19. Ali M, Ohioma E, Kraft F, *et al.*, 2015, Theoretical, numerical, and experimental study of dynamic axial crushing of thin walled pentagon and cross-shape tubes. *Thin Walled Struct*, 94: 253–272.
20. Liu YJ, 2008, Crashworthiness design of multi-corner thin-walled columns. *Thin Walled Struct*, 46: 1329–1337.
21. Wang J, Liu Y, Wang K, *et al.*, 2022, Progressive collapse behaviors and mechanisms of 3D printed thin-walled composite structures under multi-conditional loading. *Thin Walled Struct*, 171: 108810.
22. Vinayagar K, Kumar AS, 2017, Crashworthiness analysis of double section bi-tubular thin-walled structures. *Thin Walled Struct*, 112: 184–193.
23. Zhang Y, Wang J, Wang C, *et al.*, 2018, Crashworthiness of bionic fractal hierarchical structures. *Mater Des*, 158: 147–159.
24. Wang J, Zhang Y, He N, *et al.*, 2018, Crashworthiness behavior of Koch fractal structures. *Mater Des*, 144: 229–244.
25. Gao Q, Liao W, 2021, Energy absorption of thin walled tube filled with gradient auxetic structures-theory and simulation. *Int J Mech Sci*, 201: 106475.
26. Huang J, Zheng Z, Deng X, *et al.*, 2022, Crashworthiness analysis of gradient fractal thin-walled structure. *Thin Walled Struct*, 181: 110102.
27. Hao P, Du J, 2018, Energy absorption characteristics of bio-inspired honeycomb column thin-walled structure under impact loading. *J Mech Behav Biomed Mater*, 79: 301–308.
28. Nguyen-Van V, Wu C, Vogel F, *et al.*, 2021, Mechanical performance of fractal-like cementitious lightweight cellular structures: Numerical investigations. *Compos Struct*, 269: 114050.
29. Li Z, Shen L, Wei K, *et al.*, 2021, Compressive behaviors of fractal-like honeycombs with different array configurations under low velocity impact loading. *Materials* (*Basel*), 163: 107759.

    https://doi.org/10.3390/ma14175040
30. San Ha N, Pham TM, Chen W, *et al.*, 2021, Crashworthiness analysis of bio-inspired fractal tree-like multi-cell circular tubes under axial crushing. *Thin Walled Struct*, 169: 108315.

    https://doi.org/10.1016/j.tws.2021.108315
31. He Q, Wang Y, Gu H, *et al.*, 2022, The dynamic behavior of fractal-like tubes with Sierpinski hierarchy under axial loading. *Eng Comput*, 38: 1285–1298.
32. Li K, Feng Y, Gao Y, *et al.*, 2020, Crashworthiness optimization design of aluminum alloy thin-walled triangle column based on bioinspired strategy. *Materials*, 13: 666.
33. Chen W, Wierzbicki T, 2001, Relative merits of single-cell, multi-cell and foam-filled thin-walled structures in energy absorption. *Thin Walled Struct*, 39: 287–306.
34. Dadrasi A, Beynaghi M, Fooladpanjeh S, 2019, Crashworthiness of thin-walled square steel columns reinforced based on fractal geometries. *Trans Indian Inst Met*, 72: 215–225.
35. Fan ZG, Lu LX, Wang J, 2015, Effect of fatigue damage on energy absorption properties of honeycomb paperboard. *Shock Vib*, 2015: 1–7.
36. Van Vuong N, Quan MH, 2019, Fatigue analysis of jacket support structure for offshore wind turbines. *J Sci Technol Civil Eng*, 13: 46–59.
37. Zou Q, Zhou X, Wang R, *et al.*, 2022, Load-carrying and energy-absorbing performance of honeycombs with different cross sections under cyclic loading. *Mat Today Commun*, 33: 104582.
38. Wu C, Do TT, Tran PJ, 2021, Mechanical properties of polyjet 3d-printed composites inspired by space-filling peano curves. *Polymers* (*Basel*), 13: 3516.

    https://doi.org/10.3390/polym13203516
39. Wickramasinghe S, Do T, Tran P, 2022, Flexural behavior of 3D printed bio-inspired interlocking suture structures. *MSAM*, 1: 9.
40. Nguyen-Van V, Panda B, Zhang K, *et al.*, 2021, Digital design computing and modelling for 3-D concrete printing. *Autom Constr*, 123: 103529.
41. Liu J, Nguyen-Van V, Panda B, *et al.*, 2022, Additive manufacturing of sustainable construction materials and form-finding structures: A review on recent progresses. *3D Print Addit Manuf*, 2022. 9: 12–34.
42. Nguyen-Van V, Li S, Liu J, *et al.*, 2022, Modelling of 3D concrete printing process: A perspective on material and structural simulations. *Addit Manuf*, 2022: 103333.
43. Peng C, Tran P, Mouritz A, 2022, Compression and buckling analysis of 3D printed carbon fibre-reinforced polymer cellular composite structures. *Compos Struct*, 300: 116167.
44. Zhang Y, Wei Y, Bai J, *et al.*, 2022, A novel seawater and sea sand concrete-filled FRP-carbon steel composite tube column: Cyclic axial compression behaviour and modelling. *Compos Struct*, 252: 113531.
45. Alhyari O, Newaz G, 2021, Energy absorption in carbon fiber composites with holes under quasi-static loading. *C J Carbon Res*, 7: 16.
46. Zhang Y, Lu Z, Yang Z, *et al.*, Resilient carbon fiber network materials under cyclic compression. *Carbon*, 155: 344–352.
47. Peng C, Tran P, Nguyen-Xuan H, *et al.*, 2020, Mechanical performance and fatigue life prediction of lattice structures: Parametric computational approach. *Compos Struct*, 235: 111821.
48. Bunsell AR, 2018, Handbook of Properties of Textile and Technical Fibres. United Kingdom: Woodhead Publishing.

49. Wickramasinghe S, Do T, Tran P, 2020, FDM-based 3D printing of polymer and associated composite: A review on mechanical properties, defects and treatments. *Polymers*, 12: 1529.

50. Zhao B, Chen W, Hu J, *et al*., 2015, An innovative methodology for measurement of stress distribution of inflatable membrane structures. *Meas Sci Technol*, 27: 025002.

51. Alderson A, Alderson K, 2007, Auxetic Materials. Proceedings of the Institution of Mechanical Engineers Part G, *J Aerospace Eng*, 221: 565–575.

Materials Science in Additive Manufacturing

Special Issue Alerts

Invitation for Special Issue Proposals

Organizing and editing for a Special Issue helps Guest Editors gain editorial experience and improve academic profile, in addition to being a part of organizing scientific communication of contemporary topics.

If you are published researcher and have an idea for a Special Issue, please write in via email to our Managing Editor (msam.office@accscience.sg). Please provide your CV, professional profile page and a topic of interest in your email. Our colleague will guide you in the process of writing a Special Issue proposal.

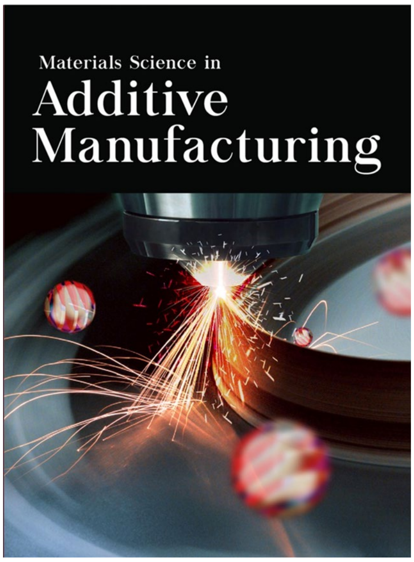

Frequently Asked Questions

1. **Are Special Issue submissions processed in the same way how Regular Issue papers are being pre-screened and reviewed?**
   Yes, all full-length article submissions to a Special Issue will go through the same editorial and peer-review process. The distinct difference here is that the Guest Editors will replace the usual editors and get involved in the making professional decisions on papers after peer review. Note that the specific roles of a Guest Editor could vary across Special Issues.

2. **How many Guest Editors are required to organize a Special Issue?**
   There is no fixed number; however, we suggest no more than 4 Guest Editors per Special Issue. More importantly, all Guest Editors should have excellent publication track records and demonstrated expertise in the topic(s) being proposed.

3. **Is the Special Issue governed by important deadlines?**
   Yes.

Benefits of Being A Guest Editor

- A chance to get involved in the conception and development of a specialty, contemporary topic that is of interest to the readers
- A chance to expand your professional network to the scholars and researchers who are similarly involved in the research of specialty topic
- A chance to hone your editorial skills
- A chance to gain first-hand experience of editing a thematic issue publication, which is a very valuable experience for those who aspire to edit their own journal in future
- A chance to improve your academic profile and help establish your academic influence within your discipline

ACCSCIENCE
PUBLISHING

OUR JOURNALS

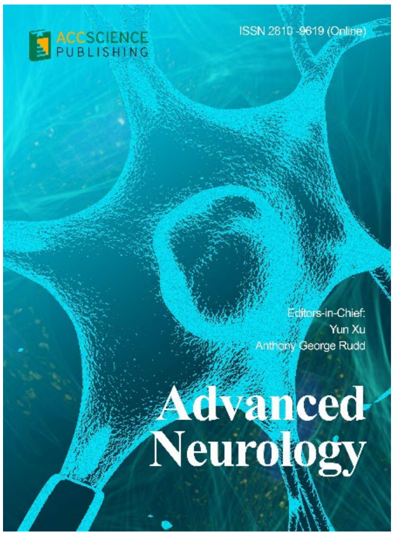

Advanced Neurology is a peer-reviewed and open-access journal that aims to publish and disseminate novel research in the breadth of neurology and neuroscience. The journal aims to advance our understanding in the nervous system and provide a platform to neuroscientists and physicians to showcase their findings in original fundamental and clinical research as well as to present new ideas that highlight the changes in the neurological clinical practice.

Advanced Neurology covers subject areas, including but not limited to the following:

- Neurological disorders
- Neurodegenerative disease
- Cerebrovascular disease
- Epilepsy and movement disorders
- Neuroimmune disease
- Neurological infections
- Muscle disease
- Molecular and cellular neuroscience
- Systems neuroscience
- Cognitive neuroscience
- Computational modeling of nervous system

Gene & Protein in Disease publishes rigorously peer-reviewed and high quality original articles and authoritative reviews that focus on the latest development in multidisciplinary areas in biology and biomedicine, with an emphasis on gene and protein research. The journal has worldwide authorship, and a broad scope in basic and translational biomedical research of genetics, biochemistry, biophysics, oncology, immunology, cell biology, molecular biology, developmental biology, microbiology, neuroscience, stem cell, protein science, structural biology, regenerative medicine and translational medicine.

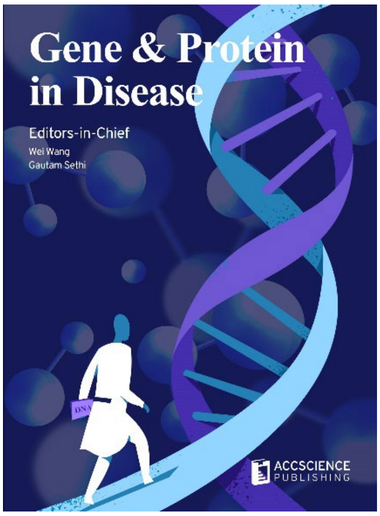

Start a new journal

Write to us via email if you are interested to start a new journal with AccScience Publishing. Please attach your CV, professional profile page and a brief pitch proposal in your email. We shall inform you of our decision whether we are interested to collaborate in starting a new journal.

Contact: info@accscience.com

ACCSCIENCE
PUBLISHING

Access Science Without Barriers

Contact

www.accscience.com
8 Burn Road, #15-03 Trivex, Singapore 369977
Email: editorial@accscience.com
Phone: +65 8182 1586